COO-3060-5
MITNE-131

LMFBR BLANKET PHYSICS PROJECT
PROGRESS REPORT NO. 2

June 30, 1971

Massachusetts Institute of Technology
Department of Nuclear Engineering
Cambridge, Massachusetts 02139

Contract AT(11-1)-3060
U.S. Atomic Energy Commission

MASSACHUSETTS INSTITUTE OF TECHNOLOGY
DEPARTMENT OF NUCLEAR ENGINEERING
Cambridge, Massachusetts 02139

COO-3060-5 MITNE-131
AEC Research and Development Contract
UC-34 Physics

LMFBR BLANKET PHYSICS PROJECT PROGRESS REPORT NO. 2

June 30, 1971

Contract AT(11-1) 3060
U.S. Atomic Energy Commission

Editors:

I. A. Forbes
M. J. Driscoll
N. C. Rasmussen
D. D. Lanning
I. Kaplan

Contributors:

S. T. Brewer
G. J. Brown
P. DeLaquil, III
M. J. Driscoll
I. A. Forbes
C. W. Forsberg
E. P. Gyftopoulos
P. L. Hendrick
C. S. Kang
I. Kaplan
J. L. Klucar
D. D. Lanning
T. C. Leung
E. A. Mason
N. R. Ortiz
N. A. Passman
N. C. Rasmussen
I. C. Rickard
V. C. Rogers
G. E. Sullivan
A. T. Supple
C. P. Tzanos

DISTRIBUTION

COO-3060-5 MITNE-131

AEC Research and Development Contract

AT(11-1) 3060

UC-34 Physics

1-3. U.S. Atomic Energy Commission, Headquarters
Division of Reactor Development and Technology
Reactor Physics Branch

4, 5. U.S. Atomic Energy Commission
Cambridge Office

6. Dr. Paul Greebler, Manager
Nuclear Energy Division
Breeder Reactor Department
General Electric Company
310 DeGuigne Drive
Sunnyvale, California 94086

7. Dr. Harry Morewitz, Manager
LMFBR Physics and Safety Projects
Atomics International
P.O. Box 309
Canoga Park, California 91305

8. Mr. Malcolm Dyos, Manager
Nuclear Development, LMFBR Project
Westinghouse Electric Corporation
Advanced Reactors Division
Waltz Mill Site
P.O. Box 158
Madison, Pennsylvania 15663

9. Dr. Robert Avery, Director
Reactor Physics Division
Argonne National Laboratory
9700 South Cass Avenue
Argonne, Illinois 60439

10. Dr. Charles A. Preskitt, Jr., Manager
Atomic and Nuclear Department
Gulf Radiation Technology
P.O. Box 608
San Diego, California 92112

ABSTRACT

This is the second annual report of an experimental program for the investigation of the neutronics of benchmark mock-ups of LMFBR blankets.

During the period covered by the report, July 1, 1970 through June 30, 1971, work was devoted primarily to measurements on Blanket Mock-Up No. 2, a simulation of a typical large LMFBR radial blanket and its steel reflector.

Activation traverses and neutron spectra were measured in the blanket; calculations of activities and spectra were made for comparison with the measured data. The heterogeneous self-shielding effect for U^{238} capture was found to be the most important factor affecting the comparison.

Optimization and economic studies were made which indicate that the use of a high-albedo reflector material such as BeO or graphite may improve blanket neutronics and economics.

TABLE OF CONTENTS

LIST OF FIGURES

LIST OF TABLES

1. INTRODUCTION

1.1 Foreword

This is the second annual report of the LMFBR Blanket Physics Project. This report covers work done since the last progress report, Reference 1, during the time period from July 1, 1970 through June 30, 1971.

The MIT Blanket Research Project is part of the AEC's LMFBR development program, having as its primary objective the experimental investigation of clean, but realistic, benchmark mock-ups of the blanket-reflector region of typical large LMFBR designs.

The key experimental tool used in this work is the Blanket Test Facility at the MIT Research Reactor (2), which contains a fission-converter plate tailored to deliver a spectrum typical of that leaking from a large LMFBR core, and which can be used to drive blanket mock-ups. This facility permits investigations of blanket neutronics without tying up a critical facility, at an equivalent core power of approximately 500 watts, and requiring only about one-tenth the blanket inventory of a full cylindrical critical core plus blanket.

During the first year of the project, the work was concerned mainly with check-out of the newly constructed facility and with development and evaluation of experimental procedures to be used for the acquisition of data. Thus the present report is the first to contain substantial information on an actual simulated blanket. The blanket in question, designated Blanket Mock-Up No. 2, is a three-subassembly-row assembly with a steel reflector. Uranium metal fuel rods, carbon steel cladding and Na_2CrO_4 in the "coolant" region are used to simulate a real blanket containing UO_2 fuel, stainless steel cladding and sodium metal coolant.

1.2 Work Areas

During the report period, most of the work involved material activation traverses in the test blanket. Foil activation experiments were

also made to permit unfolding of the local neutron spectra. An extensive program of instrumental neutron spectrometry is also well under way, using He^3, Li^6 and p-recoil detectors. Chapters 2 through 4 describe this part of the program.

Methods development work also includes an assessment of the use of prompt capture gamma analysis for the determination of the blanket neutron balance and neutron spectra (Chapters 5 and 6).

The key question of the extent of heterogeneous self-shielding of U^{238} was also investigated both experimentally and theoretically. The results are reported in Chapters 7 and 8.

Optimization and economic analyses were carried out to assess candidate blanket configurations for subsequent experimental investigation. As noted in Chapters 9 and 10, a high-albedo moderating reflector appears to have sufficiently good prospects to justify its selection for Blanket Mock-Up No. 3.

1.3 Staff

The project staff, including thesis students, during the report period was as follows:

*M. J. Driscoll, Associate Professor of Nuclear Engineering
Project Leader

†E. P. Gyftopoulos, Professor of Nuclear Engineering

*I. Kaplan, Professor of Nuclear Engineering

*D. D. Lanning, Professor of Nuclear Engineering

†E. A. Mason, Professor of Nuclear Engineering

*N. C. Rasmussen, Professor of Nuclear Engineering

I. A. Forbes, DSR Staff (from June to September 1971)

I. C. Rickard, DSR Staff (from June to September 1971)

V. C. Rogers, DSR Staff (June and July 1971)

*A. T. Supple, Jr., Engineering Assistant

---

* Continuing on staff after Summer 1971.

† Salary not paid from contract funds during FY 1971.

G. E. Sullivan, Technician (half-time)

S. T. Brewer, Research Assistant (to May 1971)
Ph. D. Student

*G. J. Brown, Research Assistant (as of June 1971)
S. M. Student

†C. W. Forsberg, AEC Fellow, S. M. Student (to June 1971)

P. L. Hendrick, Research Assistant (June to September 1971)

*C. S. Kang, Research Assistant, Sc. D. Student

*T. C. Leung, Research Assistant, Ph. D. Student

*N. R. Ortiz, Research Assistant, Ph. D. Student

N. A. Passman, Research Assistant (to February 1971)
S. M. Student

C. P. Tzanos, Research Assistant (to September 1971)
Ph. D. Student

1.4 References

(1) LMFBR Blanket Physics Project Progress Report No. 1, MIT-4105-3, MITNE-116, June 30, 1970.

(2) I. A. Forbes et al., "Design, Construction and Evaluation of a Facility for the Simulation of Fast Reactor Blankets," MIT-4105-2, MITNE-110, Feb. 1970.

---

* Continuing on staff after Summer 1971.

† Salary not paid from contract funds during FY 1971.

2. DESCRIPTION OF BLANKET ASSEMBLY NO. 2

J. L. Klucar and T. C. Leung

2.1 Introduction

Descriptions of the Blanket Test Facility and of Blanket Assembly No. 2 are contained in Reference 1. A brief description of Blanket No. 2 is included below for convenience.

B. T. F. Blanket No. 2 is a mock-up of a typical LMFBR blanket composition. Subassembly boxes of low-carbon steel rectangular mechanical steel tubing are loaded with 121 uranium metal fuel rods arranged on a square lattice spacing of 0.511 inch; the 0.25-inch-diameter uranium metal fuel is clad in low-carbon steel tubing. The inter-rod volume in each subassembly is filled with anhydrous sodium chromate (Na_2CrO_4) powder. The subassembly boxes are loaded on an experimental cart to provide a blanket assembly which is 48 inches high, 59.2 inches wide and 17.72 inches thick. The blanket is backed by an 18-inch-thick low-carbon steel reflector.

The as-loaded atom densities for Blanket No. 2 are given in Table 2.2.

2.2 Description of Blanket No. 2

2.2.1 General Description

Figure 2.1 shows a schematic view of Blanket Assembly No. 2. A 58-1/4-inch by 62-7/16-inch piece of 1-inch-thick mild steel plate welded between two 60-inch by 39-inch pieces of 1-inch-thick mild steel plate forms an "H" frame support structure which is mounted on an experimental cart. The front section of the "H" frame contains three rows of the blanket subassemblies, and the rear section is filled with seventeen 58-1/4-inch by 60-inch pieces of 1-inch-thick mild steel plate to act as a neutron reflector. Twenty-five of the subassemblies contain steel-clad uranium metal fuel rods and anhydrous sodium chromate powder. The outer subassemblies (see Fig. 2.1) are filled with the

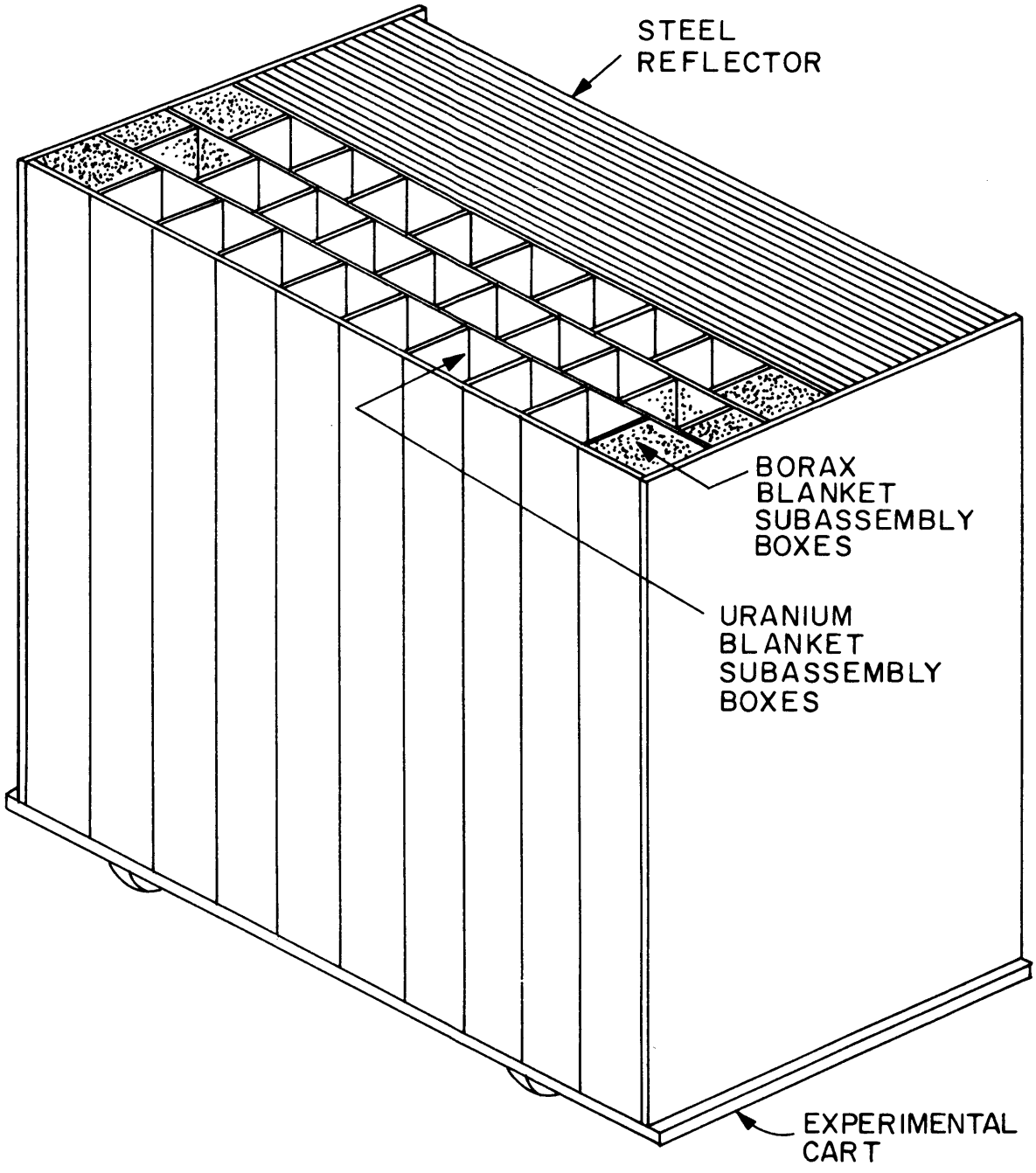

FIG. 2.1 SCHEMATIC VIEW OF BLANKET ASSEMBLY NO. 2

mixture of iron punchings and anhydrous borax ($Na_2B_4O_7$) powder used for Blanket Assembly No. 1.

Twenty-six tubes are provided for foil activation traverses in the axial and transverse directions through the blanket (see Fig. 2.2). The 58-inch-long mild steel tubes have a 7/16-inch O. D. and a 0.028-inch wall thickness. A 2-inch-diameter hole, 4 inches below mid-plane, has been drilled through the reflector to provide a beam hole for fast neutron and prompt gamma spectrum measurements. In addition, a foil holder rod may be inserted in this hole for foil activation traverses through the reflector region.

2.2.2 Description of the Subassemblies

The low-carbon steel subassembly boxes are 5.92 inches square, 60 inches high and have a wall thickness of approximately 3/32 inch. The bottom of each subassembly is sealed with a seam-welded steel plate. Each subassembly contains 121 fuel rods arranged in an eleven by eleven square lattice with a pitch of 0.511 inch. Sixty of the rods have a U^{235} enrichment of 1.016%, and sixty-one have a U^{235} enrichment of 1.143%; the two enrichments are loaded in a checkerboard pattern within the subassembly box. The tips of the higher enrichment rods are painted orange to facilitate identification.

The fuel rods are held in place by upper and lower aluminum grid plates. The lower grid plate rests on the bottom closure plate, and the upper grid plate is supported on four 48-inch-long tubes which have an O. D. of 7/16 inch and a wall thickness of 0.028 inch. These tubes fit over four fuel rods located near the corners of the lattice. The fuel rods are loaded through the upper grid down into the lower grid plate. The upper grid plate has cut-out sections for the traversing tubes and for loading the sodium chromate powder; each tube normally contains a fuel rod unless a foil traverse is to be made.

A total of 3025 fuel rods have been fabricated at M.I.T. by recladding 48-inch-long by 0.250-inch-diameter uranium metal rods in low-carbon steel tubing. The clad tubing is 50 inches long and has a 5/16-inch O. D. and an 0.018-inch wall thickness. Each end of the tube is closed by a press-fitted steel plug, 1/2 in. long and 9/32 in. in diameter.

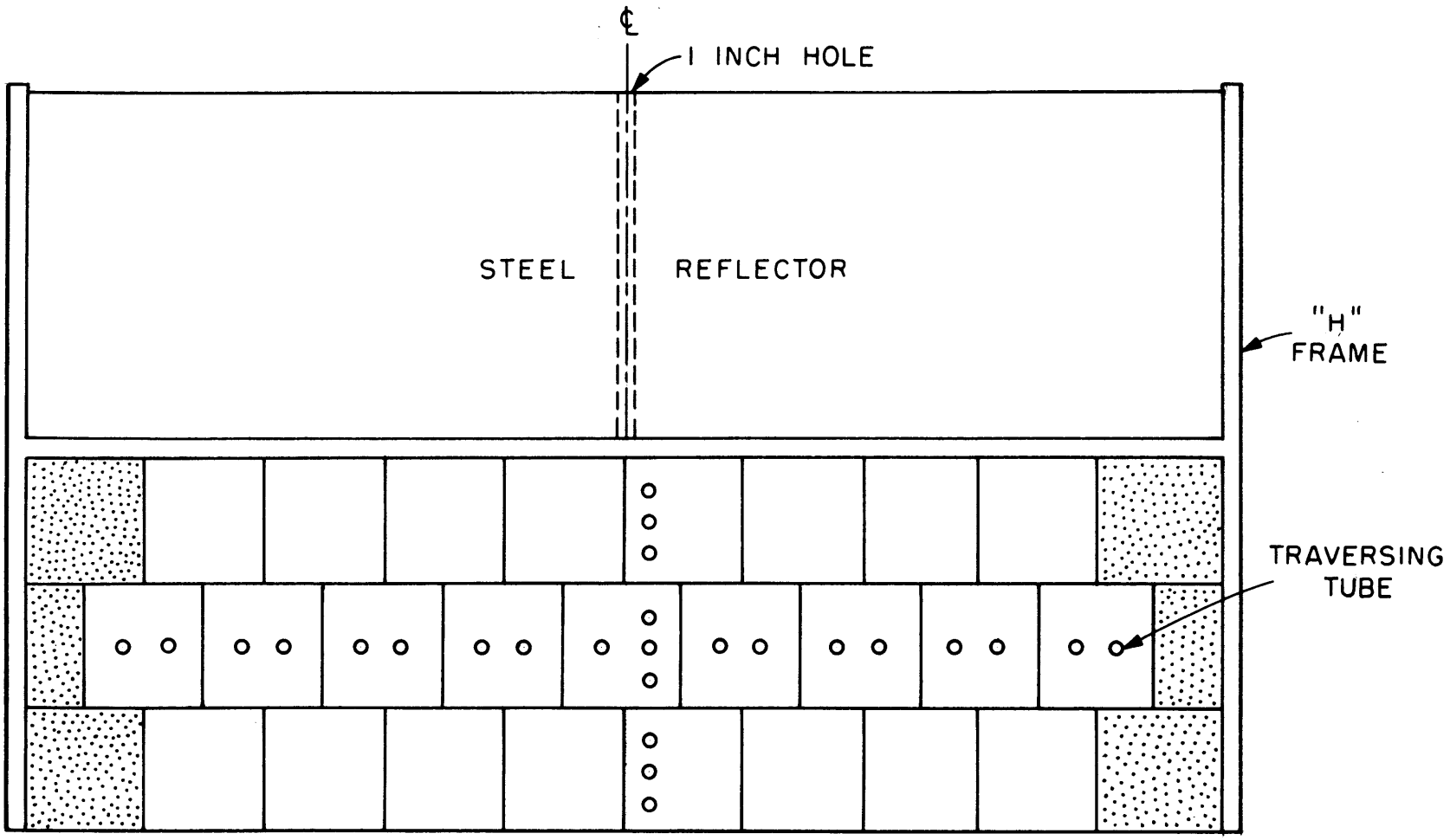

FIG. 2.2 PLAN VIEW OF BLANKET ASSEMBLY SHOWING THE TRAVERSING TUBE POSITIONS

The inter-rod volume of the subassemblies is filled with anhydrous sodium chromate powder (technical grade) which has been dried to reduce its water content to 0.10 w/o. The average loading of sodium chromate in a subassembly is 31.106 kg, with a standard deviation of ± 0.294 kg; the loadings vary from 30.51 kg to 31.80 kg, or ± 2% maximum deviation from the mean.

The top of each subassembly is sealed by a 0.035-inch-thick steel plate which is epoxied in place to ensure that the subassembly is air- and water-tight; the traversing tubes pass through sealed penetrations in this plate.

A breakdown of the subassembly weight is given in Table 2.1.

TABLE 2.1
Subassembly Component Weights

Uranium metal	89.30 kg
Na_2CrO_4	31.11 kg
Cladding	13.00 kg
Subassembly box	26.55 kg
Grid plate support tubes	0.91 kg
Grid plates	0.36 kg
Total	161.23 kg

2.2.3 Atom Densities

The atom densities for Blanket No. 2 were calculated by homogenizing the material components of a subassembly at mid-height – viz., the uranium metal fuel, the anhydrous sodium chromate and the low-carbon steel cladding, support tubes and subassembly walls. The carbon content of the steel is about 0.15 w/o; other impurities, such as manganese and nickel, are negligible. The water content of the sodium chromate is 0.10 w/o.

The homogenized atom densities in Blanket No. 2 are given in Table 2.2 where they are compared with the atom densities in an "equivalent realistic blanket," composed of 37.0 v/o depleted UO_2 (at 90% of theoretical density), 20.7 v/o Type 316 stainless steel (71.2 w/o Fe, 20.0 w/o Cr and 8.8 w/o Ni), 32 v/o sodium and 10.3 v/o void. It is evident that Blanket No. 2 provides a realistic blanket composition in all important respects, with the exception of the small hydrogen content.

TABLE 2.2

Homogenized Atom Densities in B. T. F. Blanket No. 2

Nuclide	Blanket No. 2		Equivalent Realistic Blanket*	
U^{235}	0.000088		0.000016	
U^{238}	0.008108		0.008131	
O	0.016293		0.016293	
Na	0.008128		0.008128	
Cr	0.004064		0.003728	
Fe	0.013750	0.017814	0.012611	0.017814
Ni	0.000000		0.001475	
H	0.000073		0.000000	
C	0.000096		0.000082	

*Composed of 37.0 v/o depleted UO_2 (at 90% of theoretical density), 20.7 v/o Type 316 stainless steel, 32.0 v/o sodium and 10.3 v/o void.

2.3 References

(1) "LMFBR Blanket Physics Project Progress Report No. 1," MIT-4105-3, MITNE-116 (June 1970).

3. NEUTRONICS OF BLANKET MOCK-UP NO. 2

T. C. Leung

Foil activation measurements and traverses are central to the concept of the use of Blanket Mock-Up No. 2 as a benchmark assembly. This phase of the project's work is described in the present chapter and in the forthcoming topical report:

> T. C. Leung, M. J. Driscoll, I. Kaplan and D. D. Lanning, "Neutronics of an LMFBR Blanket Mock-Up," COO-3060-1, MITNE-127.

3.1 Background

The optimization of the blanket region plays a very important role in the development of an economical LMFBR, since as much as one-third to one-half of the fissile material breeding and three-quarters of the fertile material inventory occur in the blanket region. Thus, the proper choice of blanket composition and configuration are essential to high breeding performance, and minimum fuel cycle and power cost of future LMFBRs. Unfortunately, there are substantial difficulties involved in purely theoretical studies of neutron propagation in blanket media. Multigroup calculations for blanket optimization, based mainly on methods and data developed for core studies, are likely to be inadequate. Prediction of reactor physics parameters is considerably more complex and unreliable in the blanket region than in the core, owing mainly to the severe spectral degradation occuring in the blanket. It has consequently become increasingly evident that a systematic experimental study of the blanket region is highly desirable.

The objectives of the present work were to develop standard experimental methods, acquire experimental data and to test theoretical methods on the first of a series of realistic mock-ups of typical LMFBR blanket configurations and compositions. The blanket research was conducted in the M.I.T. Blanket Test Facility (BTF) which allows focusing on the blanket mock-up without tying it to a fast reactor core.

The converter assembly of the BTF, constructed for this purpose, was designed to simulate neutron energy spectra found at the periphery of fast reactor cores in order to drive mock-ups of fast reactor blankets (see Fig. 3.1). In addition, the transverse dimensions of both converter and blanket assembly were designed to match the leakage for a hypothetical LMFBR so that the axial, Z, traverses in the slab-geometry blanket mock-up would correspond to the radial, R, traverses in the actual LMFBR. The details of the design, construction and evaluation of the BTF using Blanket Mock-Up No. 1 are given in Reference 1. The present research is concerned with Blanket Mock-Up No. 2, a simulation of a three-row radial blanket typical of current designs for use in 1000-MWe LMFBRs.

3.2 Blanket Mock-Up No. 2

Blanket Mock-Up No. 2 is shown in Fig. 2.1 of the preceding chapter on its experimental cart, and a complete description of the assembly is given in section 2.2.

As part of the analytic effort in support of the design of Blanket Mock-Up No. 2, preliminary multigroup calculations were made to confirm that all major variables were correctly accounted for. Sensitivity studies pertinent to the design and to the general assessment or results were also made. The five items studied were:

a) S_2, S_4 vs. S_8 transport theory calculations,
b) the effect of hydrogen in the sodium chromate,
c) variation in chromate density,
d) effect of using 1% Pu^{239} vs. U^{235} fuel, and
e) effects of fuel enrichment in Blanket No. 2.

The results showed that

a) S_8 calculations should be adequate for nearly all calculations;
b) $\leq$ 0.1% H_2O contamination was tolerable;
c) the uniformity of chromate density achieved in the sub-assemblies was well within acceptable limits; and
d), e) the use of 1% U^{235} fuel did not place the blanket outside the range of interest for realistic blanket studies.

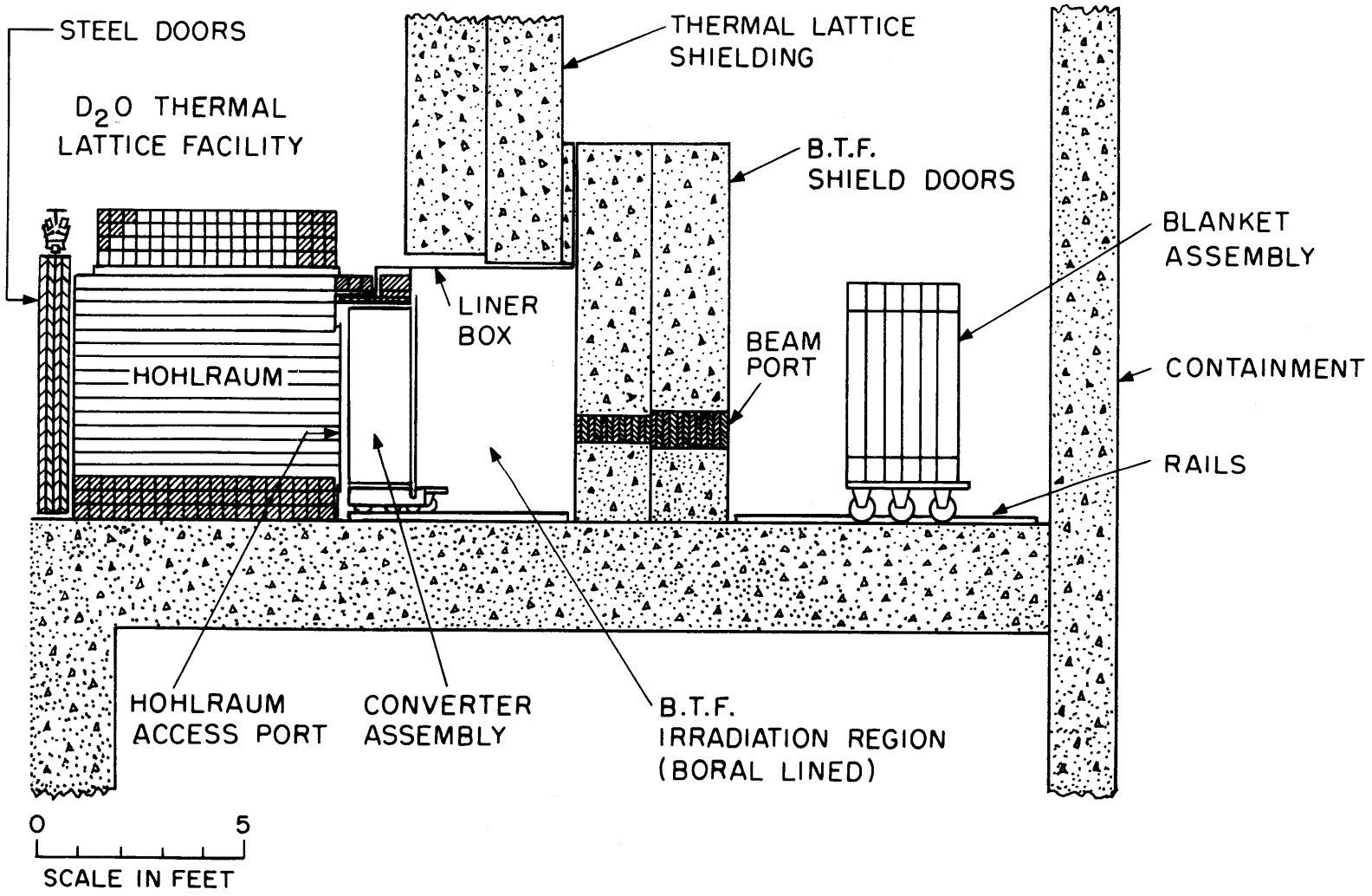

FIG. 3.1 SCHEMATIC CROSS SECTION VIEW OF HOHLRAUM AND BLANKET TEST FACILITY

3.3 Experimental Results

Experimental measurements using foil activation techniques were made in the blanket mock-up in the following major areas:
a) buckling measurements, b) reaction rate measurements, and
c) neutron spectral measurements.

a) Buckling measurements. Vertical and horizontal traverses were made with detector foils such as gold, molybdenum and indium, which are sensitive to different regions of the neutron spectrum. These traverses were used to determine that an energy-independent buckling was achieved in the transverse directions to characterize the transverse neutron leakage. Figure 3.2 shows typical foil activation traverses in the vertical direction. It was observed that fundamental-mode cosine flux shapes were achieved in the vertical and horizontal directions in the blanket mock-up. Thus, transverse leakage may be characterized by a simple buckling term and the problem reduced to an effective one-dimensional problem involving traverses through the blanket.

Figure 3.3 shows the horizontal gold-to-indium, indium-to-molybdenum, and gold-to-molybdenum activation ratios at various depths into the blanket. All these activation ratios indicated that lateral spectral equilibrium was attained in a large central volume of the blanket mock-up. The ratios also showed that backscattering perturbed the blanket spectrum in no more than the outer 30 cm of the blanket assembly.

b) Reaction rate measurements. Reaction rate traverses in the BTF Blanket Mock-Up No. 2 were made in the axial, Z, direction, simulating the radial direction of actual LMFBR blankets. The three types of reaction rates studied were as follows:

i) Capture reaction rates: $Au^{197}(n, \gamma)$, $U^{238}(n, \gamma)$, $Mo^{98}(n, \gamma)$, $Cr^{50}(n, \gamma)$ and $Na^{23}(n, \gamma)$.
ii) Threshold reaction rates: $U^{238}(n, f)$ and $In^{115}(n, n')$.
iii) Fission reaction rates: $U^{235}(n, f)$ and $Pu^{239}(n, f)$.

The reaction rate measurements in the blanket region were made by placing foils (or foil capsules) in recessed spots on the foil holder rods, inserted into the 3/8-inch-I.D. steel holder tubes in the blanket

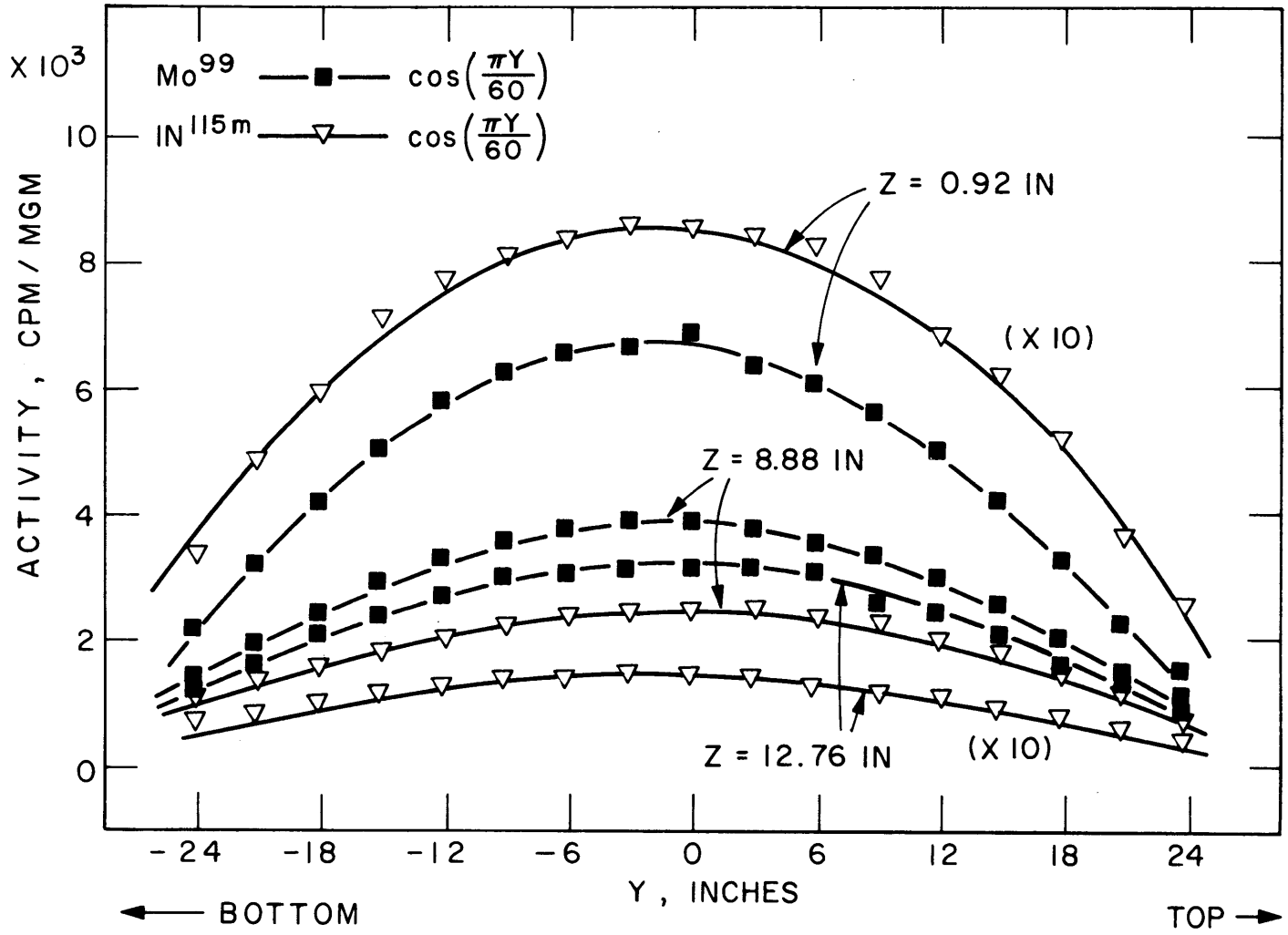

FIG. 3.2 VERTICAL ACTIVATION TRAVERSES IN BLANKET NO.2

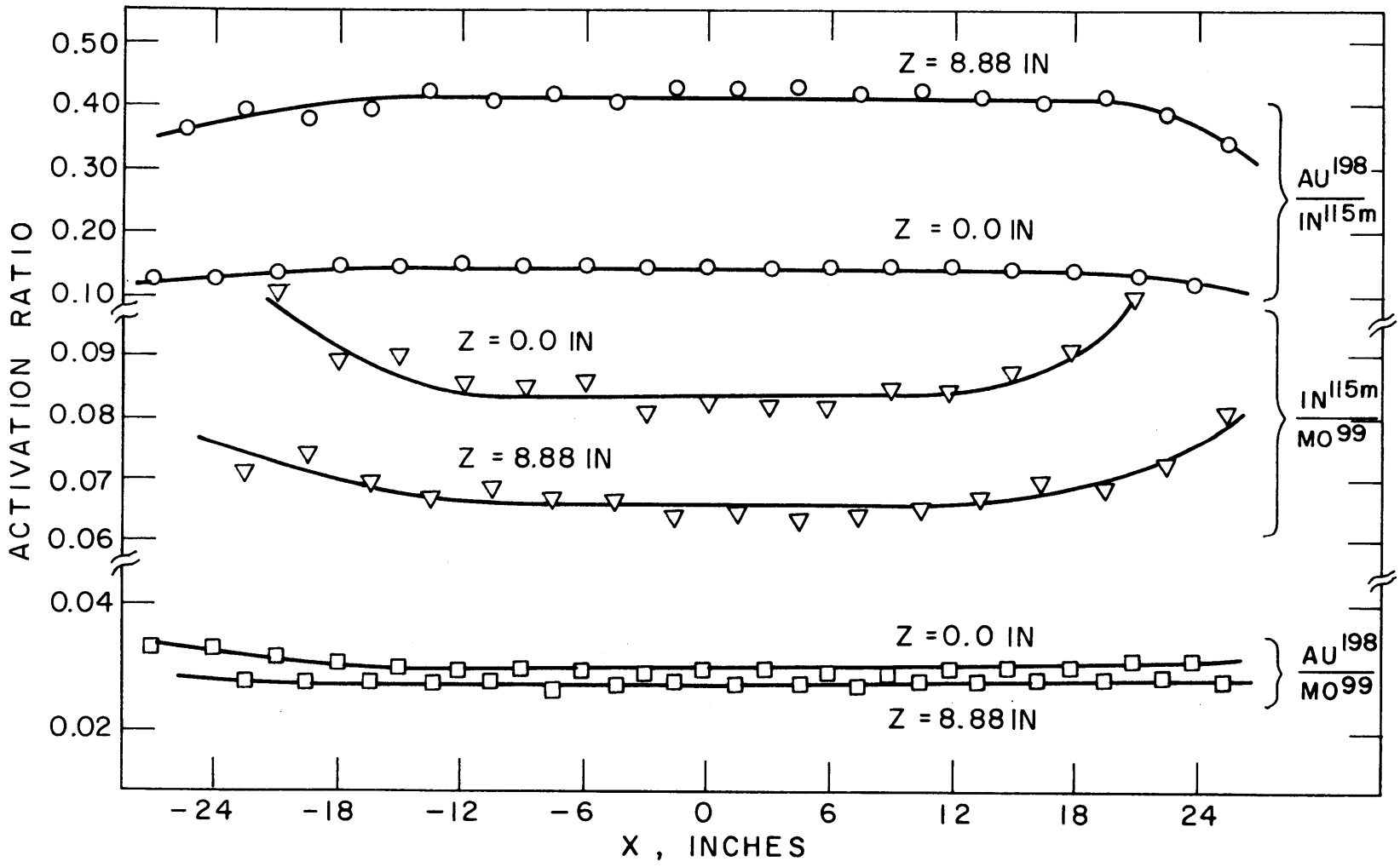

FIG. 3.3 HORIZONTAL ACTIVATION RATIOS IN BLANKET NO. 2

assembly. A single thickness of 3-mil Mylar tape was used to hold each foil in place. In the reflector region, the foils were loaded in a 2-inch-diameter foil holder cylinder, inserted into the 2-1/8-inch-diameter hole drilled horizontally through the 18-inch steel reflector at about mid-height of the blanket. The foils were irradiated from 4 to 24 hours, depending on the properties of the detector foils. A counting system, having a well-type thallium-activated, sodium iodide crystal, was used to measure the gamma activities of the irradiated detector foils. The errors in the measured foil activities were attributed mainly to the uncertainties in the counting statistics, and to a lesser extent to uncertainties in the foil weights. Other sources of error, such as from the effects of gamma attenuation, self-shielding, Mylar tape and foil holder perturbations, were found to be negligibly small. Each normalized axial foil activation traverse was also found to be reproducible to within approximately ± 2%.

Figures 3.4 through 3.8 show the results of all the reaction rate measurements and comparisons with theoretical predictions. The calculations were made with the one-dimensional ANISN transport code (2), in the S_8 option, using the 26-group Russian ABBN cross-section set (3), with shielded U^{238} cross sections. For the sake of comparison, it is found convenient to normalize both the experimental and calculated results to unity at the center of the blanket, i.e., at Z = 22.6 cm.

The agreement between experimental and theoretical reaction rate distributions, i.e., $Au^{197}(n, \gamma)$, $U^{238}(n, \gamma)$, . . . , etc., was good in the blanket region. The poorest agreement occurred in the steel reflector region, especially for the high-energy threshold reaction rates. For the nonthreshold foils, the discrepancy is probably due to the well-known difficulties involved in describing neutron diffusion in iron due to the window in its cross section near 25 keV, while the threshold foil activity mismatch may be attributable to the inadequacy of the 1D computations to describe correctly the 3D transport of the first-flight neutrons which are the primary contribution to threshold foil activation.

The degree of self-shielding of the U^{238} cross sections in the multigroup calculation had a significant effect on the resulting blanket spectra and reaction rate distributions. Broad-group cross sections for U^{238},

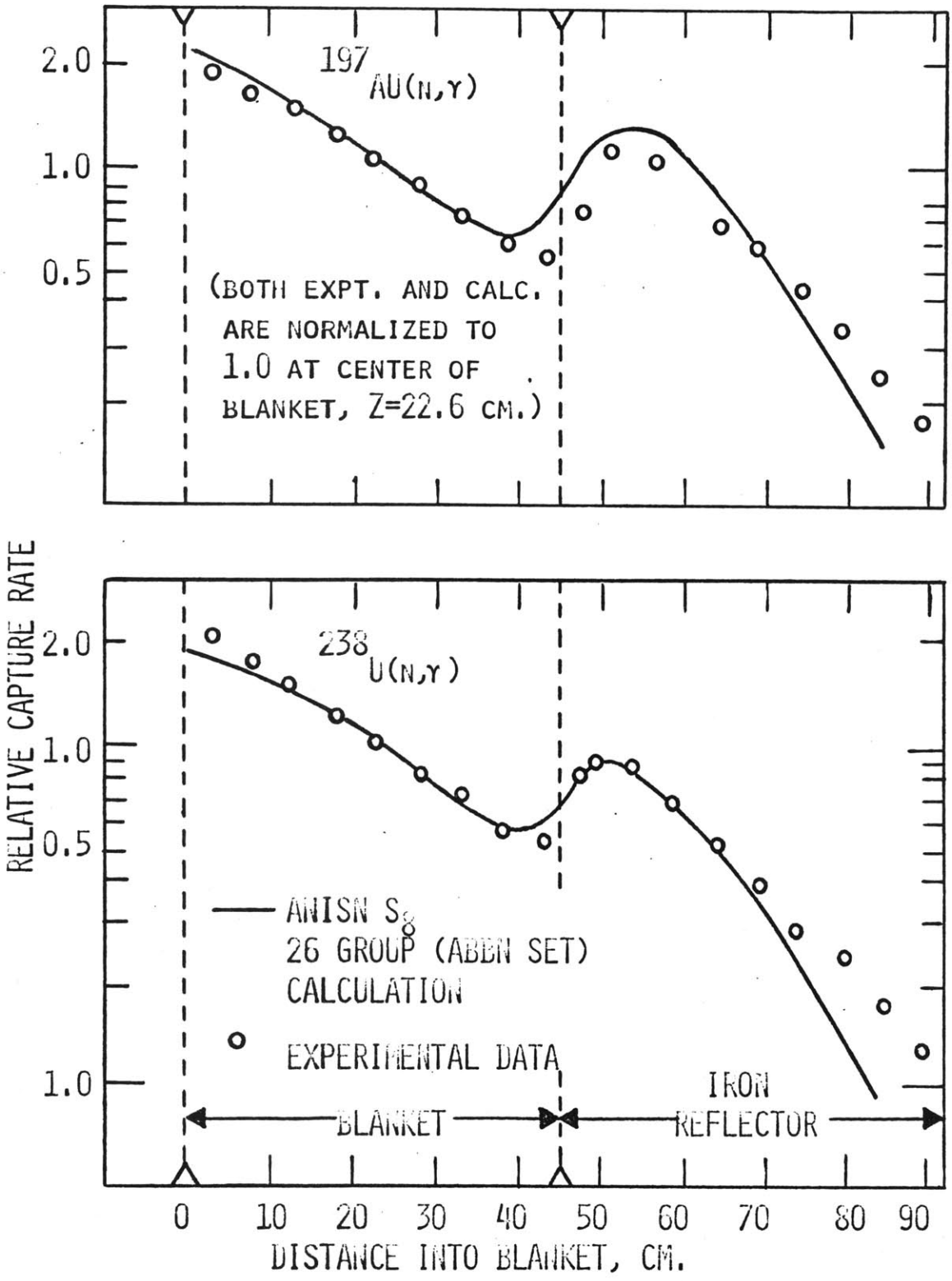

FIG. 3.4 AXIAL CAPTURE RATE DISTRIBUTIONS.

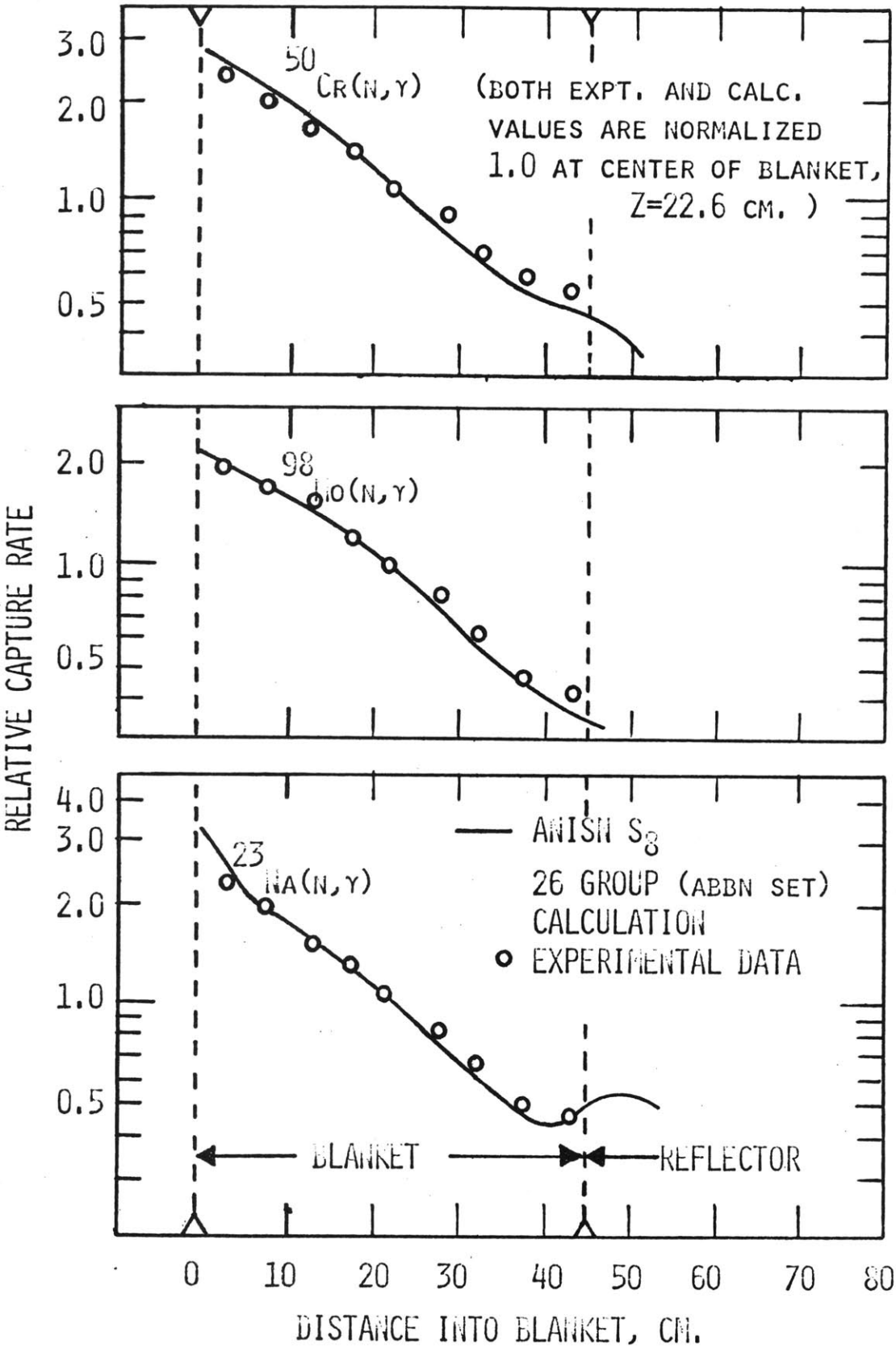

FIG. 3.5 ADDITIONAL AXIAL CAPTURE RATE DISTRIBUTIONS.

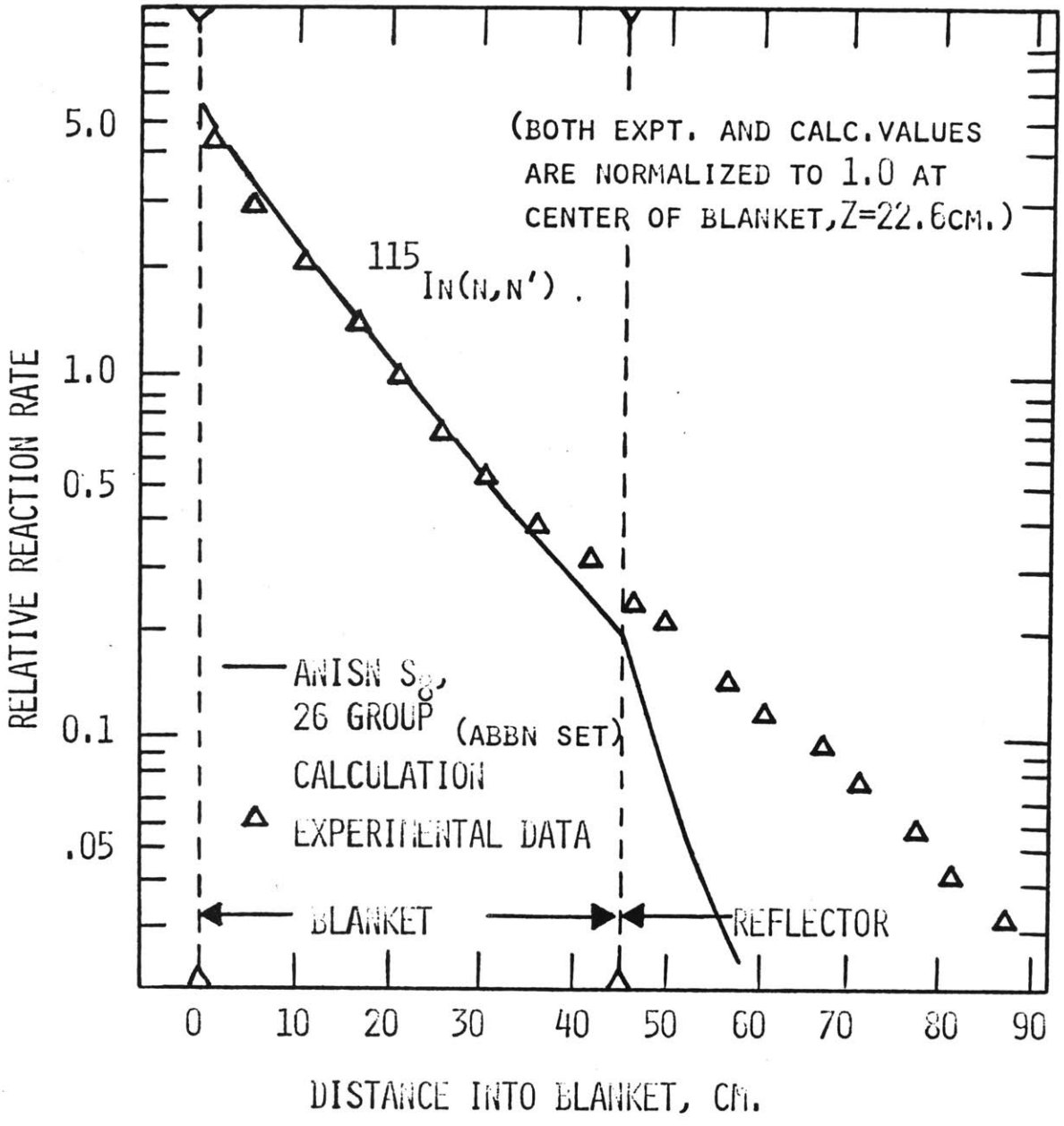

FIG. 3.6 AXIAL THRESHOLD REACTION RATE DISTRIBUTION, $^{115}In(n,n')$.

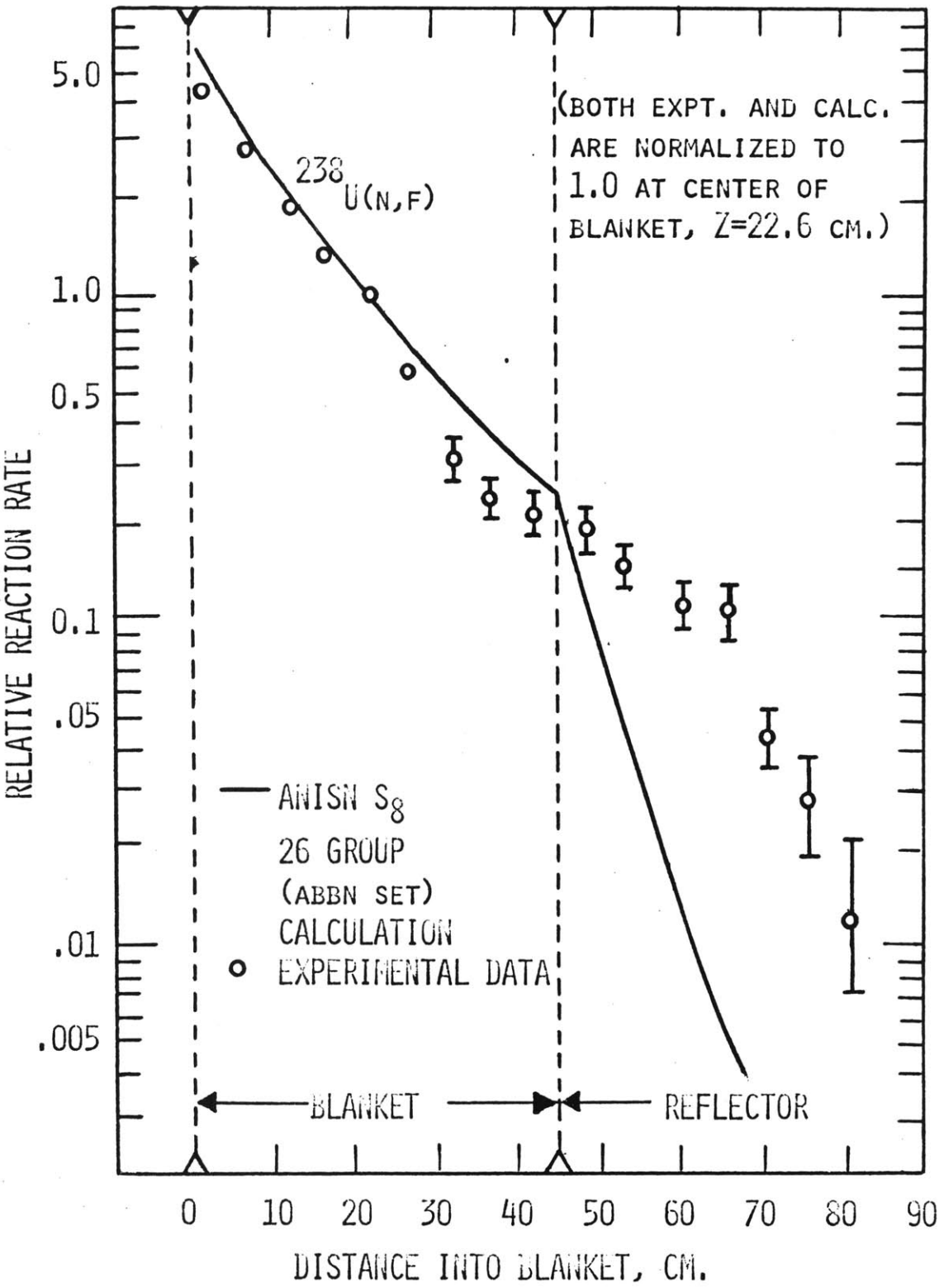

FIG. 3.7 AXIAL THRESHOLD REACTION RATE DISTRIBUTION, $^{238}U(N,F)$.

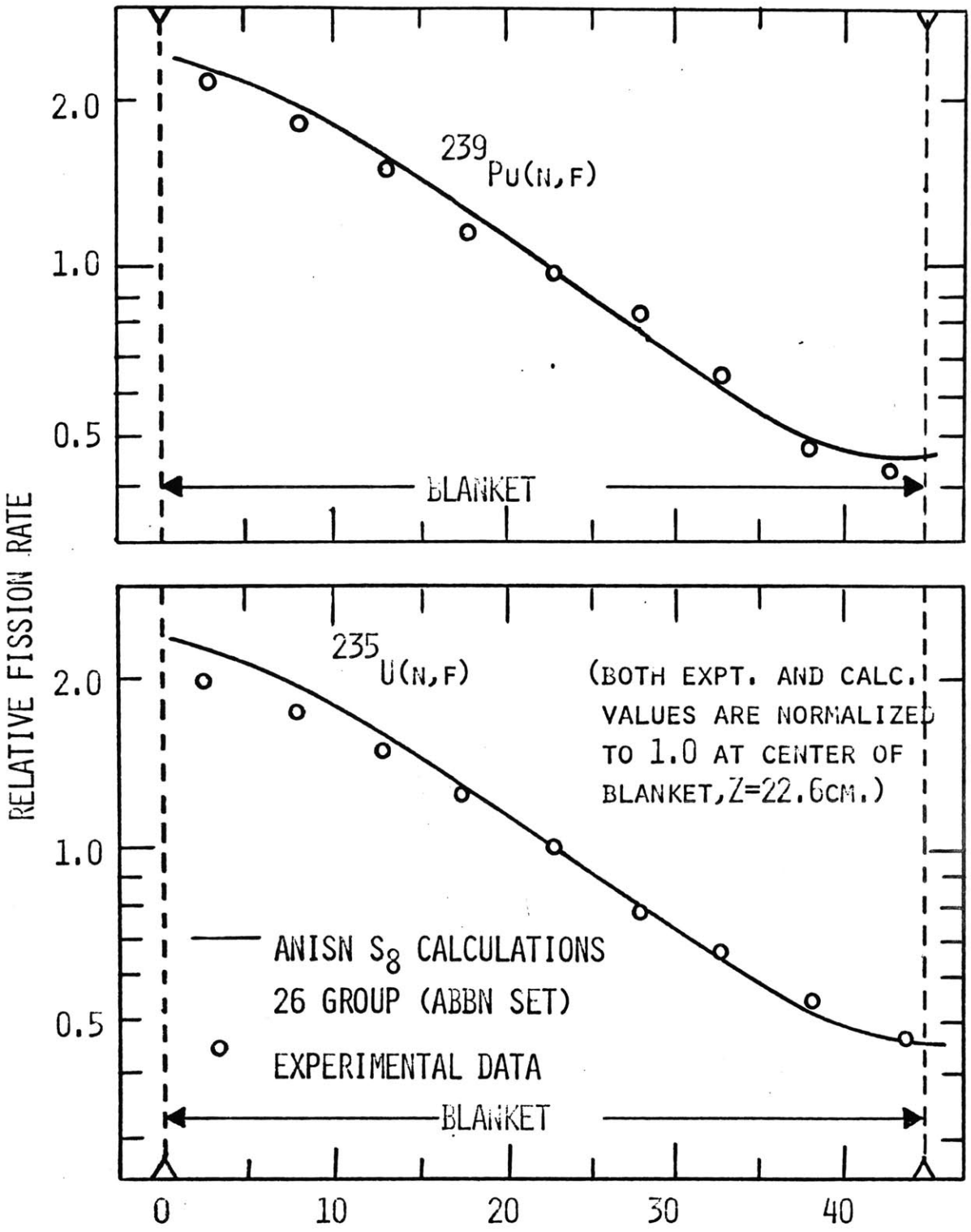

FIG. 3.8 AXIAL FISSION RATE DISTRIBUTIONS.

which accounted for resonance self-shielding, were generated with the IDIOT (4) program using the resonance data from Schmidt (5). These cross sections were then incorporated in the 26-group ABBN set before input to the multigroup ANISN code. Figure 3.9 shows the comparisons of the $Au^{197}(n, \gamma)$ and $U^{238}(n, \gamma)$ reaction rate distributions using both the shielded and unshielded U^{238} cross sections. It was found that the agreement between experimental and theoretical results was considerably better when self-shielded U^{238} cross sections are used. A discussion of the method used to make the U^{238} self-shielding correction is presented in Chapter 8.

The influence of the cross-section weighting spectrum on the reaction rate distribution was also investigated. Different weighting spectra, $\phi(u)$ = constant, $\phi(u) \propto E$ and the calculated mid-blanket spectrum,were used for preparation of the input cross-section set. The calculated results of typical reaction rate distributions using these three weighting schemes are shown in Fig. 3.10. Although no one weighting scheme best fitted the experimental data, the use of different weighting spectra did affect the reaction rate distributions to a certain extent. However, this effect was much less significant than the U^{238} shielding effect.

An overall neutron balance in BTF Blanket Mock-Up No. 2 has been made. Calculations of a one-group neutron balance showed that the net balance between the total production and the total loss of neutrons in the blanket agreed to within 2.5%. Theoretical predictions of the integral sodium and chromium capture reaction rates and U^{235} and U^{238} fission rates checked with experimental results within the experimental uncertainties.

c) Neutron spectral measurements. Blanket Mock-Up No. 2 spectra were unfolded from foil activity measurements using an improved unfolding method based on slowing-down theory. The slowing-down density is a very smoothly varying function of neutron energy, and it can therefore be characterized by few-parameter correlations. Based on selection of a specific functional relation between the flux and the slowing-down density, the LMFBR core, blanket and reflector spectra can be written in the following form (6):

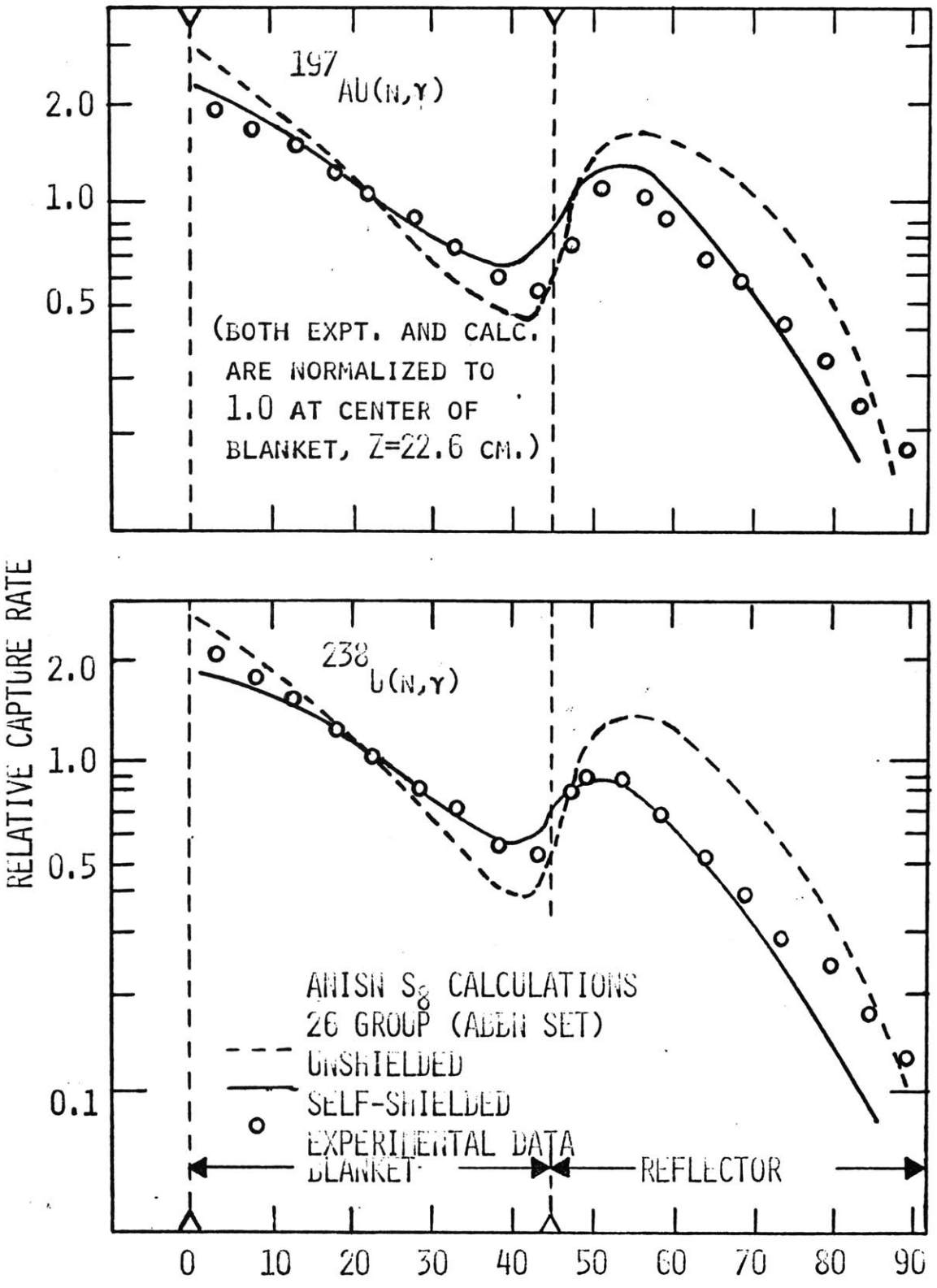

FIG. 3.9 EFFECT OF 238U SELF-SHIELDED CROSS SECTIONS ON REACTION RATE CALCULATIONS.

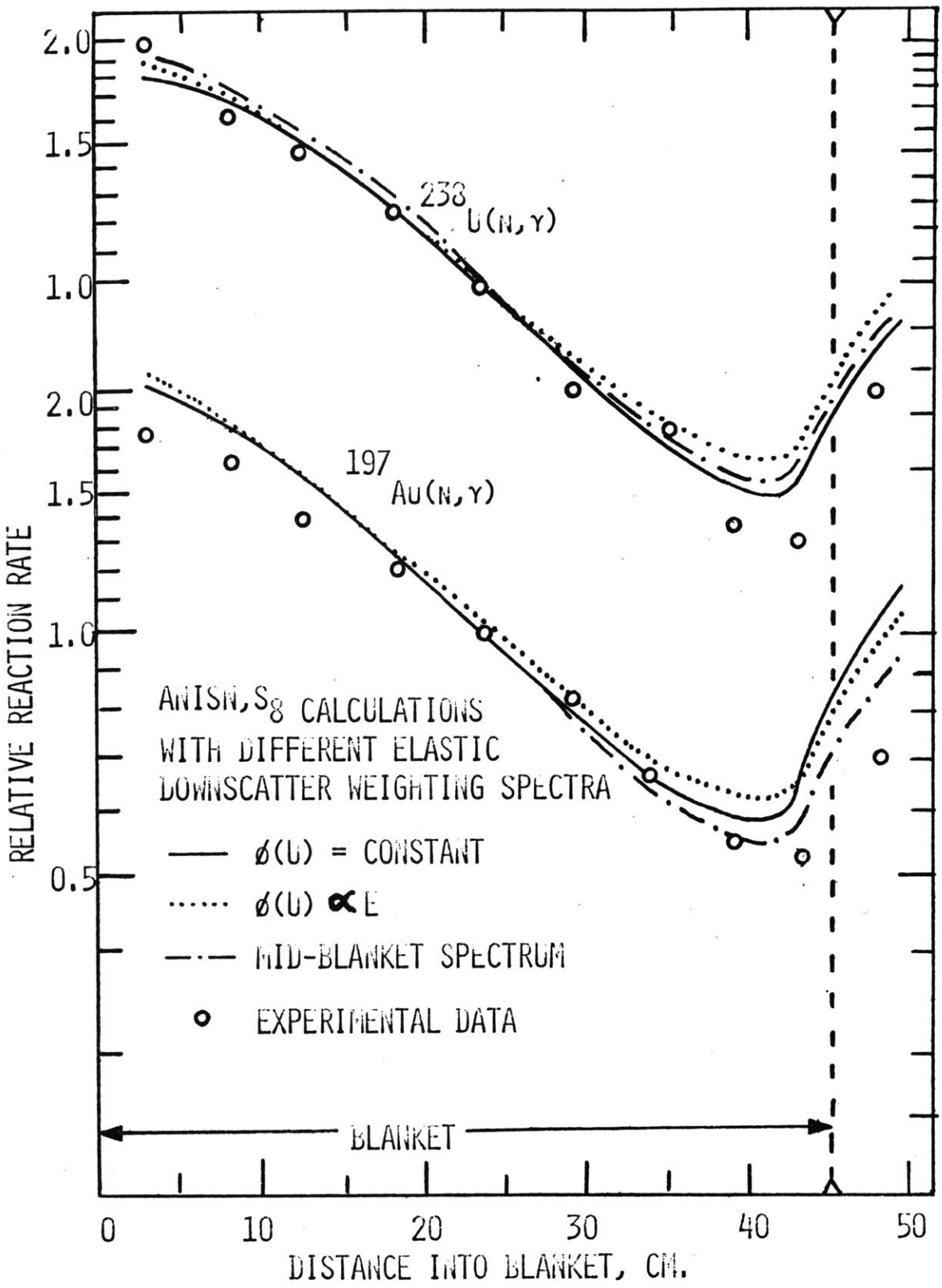

FIG. 3.10 EFFECT OF DIFFERENT WEIGHTING SPECTRA ON REACTION RATE CALCULATIONS.

$$\phi(E) = \frac{C_o}{E\xi(E)\Sigma_{tr}(E)} \exp\left\{-C_1E-C_2E^{-C_3}\right\} \qquad (3.1)$$

where

$\xi(E)\Sigma_{tr}(E)$ = slowing-down power of medium in which spectrum is to be determined, including both inelastic and elastic moderation;

C_o, C_1, C_2, C_3 = constants to be determined by minimization of differences between measured and calculated foil activities.

Iterative adjustment of the constants C_o, C_1, C_2 and C_3 permitted minimizing the difference between the measured and calculated foil activities. The resulting neutron spectrum is obtained by using Eq. 3.1 and the set of C values at which the error is minimum.

This method has been successfully tested and applied in experimental work on Blanket Mock-Up No. 2. Three foil materials were used: indium, gold, and molybdenum, which are representative of the three basic types of detector cross sections – threshold, continuous, and resonance, respectively. Figure 3.11 shows the unfolded blanket mock-up neutron spectrum in comparison with ANISN 26-group calculations. In general, the agreement between the measured and calculated spectra was good. However, the unfolded blanket spectrum was found harder than that of the ANISN calculations using shielded U^{238} cross sections but softer than that calculated by using unshielded U^{238} cross sections.

This unfolding technique was found not strongly dependent on the detector foils used, since similar resulting spectra were obtained using two different foil sets. The spectra unfolded independently, using two different foil sets (In, Au, Mo, and In, Au, Mn), were found to differ by less than 5% in the energy groups comprising the low energy flux tails.

Comparison of spectral indices (foil activity ratios) between BTF and ZPPR blankets also confirmed that M.I.T. Blanket Mock-Up No. 2 is a good simulation of an LMFBR blanket driven by a realistic benchmark critical assembly.

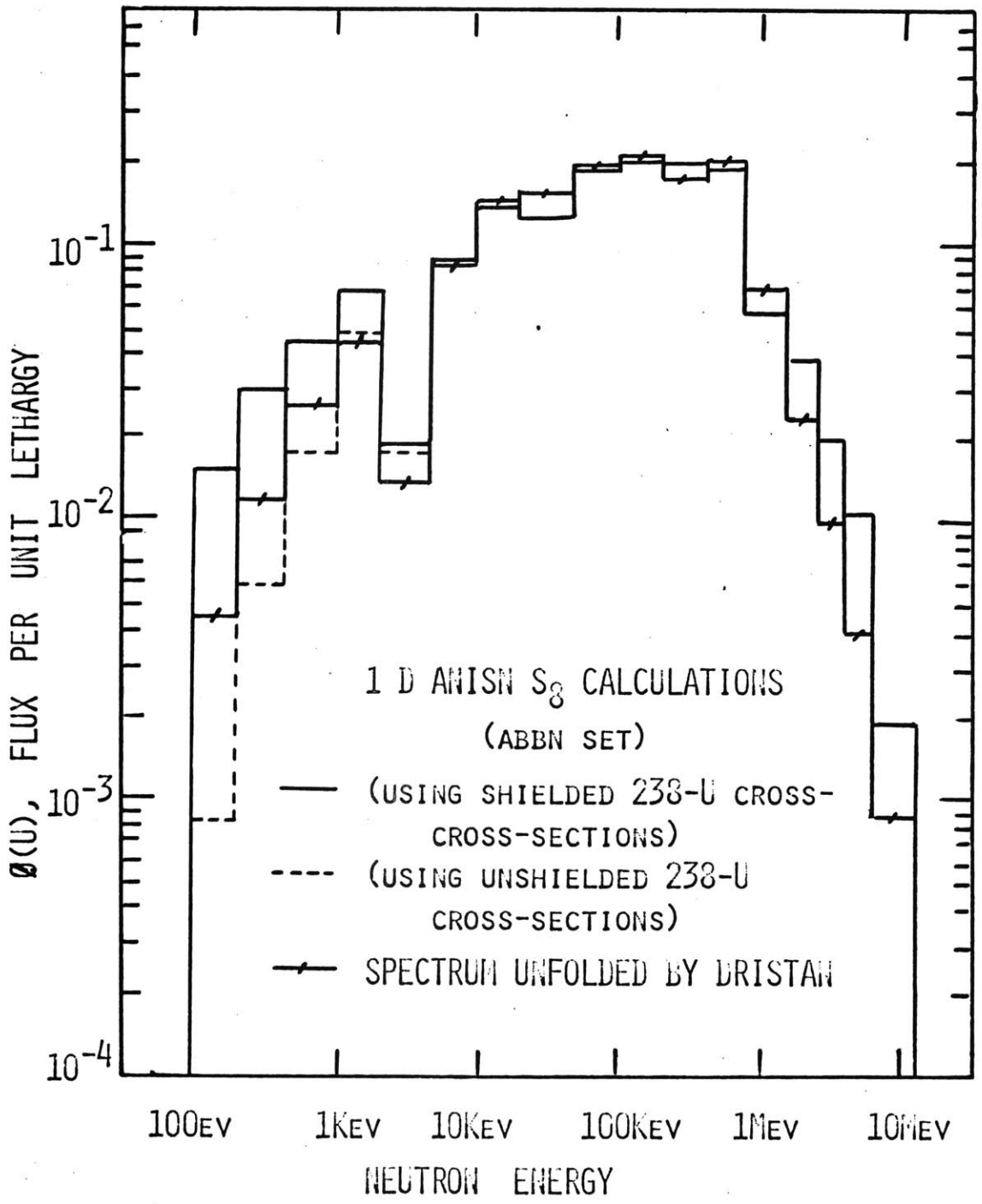

FIG. 3.11 EFFECT ON THE NEUTRON SPECTRA CALCULATIONS IN BLANKET No.2 AT Z = 7.5 cm. USING SHIELDED AND UNSHIELDED 238-U CROSS-SECTIONS.

3.4 Conclusions

Perhaps the most important general observations which can be made as a result of this work are that the BTF concept gives every evidence of being a valid approach for investigation of blanket neutronics without requiring a critical assembly driver, and that, for the most part, state-of-the-art calculation techniques give a fairly good picture of physical reality. The only discrepancy of major potential importance to LMFBR development uncovered in this work is the threshold detector mismatch in the reflector. If first-flight neutrons penetrate deeper than estimated, the potential for accentuated radiation damage to core structure exists. Resolution of this item is thus a high-priority task which should be factored into future project objectives.

3.5 References

(1) Forbes, I. A., "Design, Construction and Evaluation of a Facility for the Simulation of Fast Reactor Blankets," MITNE-110, MIT-4105-2 (Feb. 1970).

(2) Engle, W. W., M. A. Boling and B. W. Colston, "DTF-II, A One-Dimensional, Multigroup Neutron Transport Program," NAA-SR-10951 (March 1966).

(3) Abagyan, L. P., N. O. Bazazyants, I. I. Bondarenko, and M. N. Nicolaev, "Group Constants for Nuclear Reactor Calculations," edited by Bondarenko, published by Consultants Bureau, New York (1964).

(4) Pitterle, T. A. and D. M. Green, "IDIOT – A Fortran IV Code for Calculation of Resonance-Averaged Effective Cross Sections and Their Temperature Derivatives (1969).

(5) Schmidt, J. J., "Neutron Cross Sections for Fast Reactor Materials, Part I. Evaluation," KFK-120, EANDC-30-0 (1966).

4. INSTRUMENTAL METHODS FOR NEUTRON SPECTROMETRY

N. R. Ortiz and I. C. Rickard

The work which is the subject of the present chapter is primarily concerned with the use of Li^6, He^3 and p-recoil spectrometers for the measurement of neutron spectra in Blanket Mock-Up No. 2. Equally important to the acquisition of data are the techniques used to unfold neutron spectra from the measured charged particle spectra. During the past year, work has been carried out in both of these areas: development of the sophisticated electronic expertise required to accumulate charge particle spectra and development and programming of the unfolding codes.

Although considerable progress has been made and a large volume of charged particle spectra have been accumulated, reliable neutron spectra results are not presently available and must await satisfactory debugging of the unfolding programs. Thus, this chapter will be limited to a brief descriptive summary. The complete results will be included in the forthcoming topical report:

> N. R. Ortiz, I. C. Rickard, M. J. Driscoll and N. C. Rasmussen, "Instrumental Methods for Neutron Spectroscopy in the MIT Blanket Test Facility," COO-3060-3, MITNE-129.

In addition, a more complete and more quantitative summary will be included in next year's annual report.

4.1 Spectrometers Employed

Three different spectrometers are being used in the present work: Li^6, He^3 and p-recoil. The first two of these are quite similar in operating principle, consisting of two face-to-face solid state detectors in a coincidence circuit, with either a lithium-containing compound or He^3 gas interposed between the two detectors. Capture of a neutron by a lithium-6 nucleus produces two charged particles (a triton and an alpha particle) as does capture by helium-3 (in which a triton and a

proton are emitted). In both spectrometers one of the two charged particles is detected by one solid state detector, and when the other detector records a coincident detection of the second charged particle, the dual signal is accepted. In the present work, each of the charged particle spectra can be recorded in up to 4096 energy bins; and the electronics are so arranged that the sum or difference of the charged particle signals can also be recorded.

The third spectrometer employed is based upon measurement of the recoil proton spectrum following neutron scattering in a methane- or hydrogen-filled gas proportional counter. The method being used closely follows that developed by Bennett (1) and, in fact, the detector itself is on loan from ANL. Likewise, the spectrum unfolding program is for the most part a translation of an ANL-developed code.

All three spectrometers are commercially available devices, as are all of the electronic components used.

4.2 Spectrum Unfolding

As already noted, interpretation of the p-recoil spectrum is based upon the highly developed approaches perfected by ANL researchers. Considerable in-house effort at M.I.T., on the other hand, has gone into development of unfolding methods for the other two spectrometers.

Data from both the Li^6 and He^3 spectrometers can be accumulated in either the sum or difference modes. In addition, the energetics of the Li^6 reaction are such that the triton spectrum can be isolated and recorded. Thus there are three different modes of operation or types of spectra (sum, difference, individual particle) which can be analyzed.

The mathematical relations connecting the measured sum, difference or particle spectra, C(E), to the incident neutron spectrum, $\phi(E)$, are all of the form:

$$C(E) = \int P(E \mid E') \, \Sigma(E') \, \phi(E') \, dE' \qquad (4.1)$$

where

$\Sigma(E)$ = neutron absorption cross section for production of reaction;

$P(E \mid E')$ = probability distribution function relating intensity of detected spectrum at energy E to reaction rate

involving neutrons at energy E′, determined by detailed analysis of the inelastic collision mechanics governing incident and exiting particle energies and the reaction Q value.

Equation 4.1 can be solved for $\phi(E)$ in a number of ways. In order to have a clear picture of the effect of the unfolding process on the results inferred for $\phi(E)$, two fundamentally different approaches are being applied in the present work. The first method merely involves conversion of the integral equation into a discrete energy-group format and the direct application of iterative matrix inversion techniques. The second method involves differentiation of Eq. 4.1 with respect to energy to form a differential equation, which is then similarly reduced to matrix form and inverted. The differential approach is superficially similar to the method used for unfolding proton recoil spectra.

At present, unfolding code development is at the stage where consistency checks on artificially generated results having known solutions are being carried out preliminary to runs using experimental data.

4.3 Discussion

Another important aspect of the present work which should be noted is the use of a Cf^{252} source to provide a known spectrum from which an experimental detector response function can be determined. This methodology results in cancellation of a number of potential error contributions. The use of the difference-coincidence method also contributes to error cancellation: the present work, to our knowledge, will be the first detailed exposition of the application of this difference-coincidence approach in LMFBR-oriented neutron spectrometry.

Upon completion of this work, we expect to have a unique compilation of benchmark spectrum measurements involving various permutations and combinations of detector types (three), modes of operation (three), and unfolding methods (two). The results can also be compared to ANISN calculations, to foil measurements by Leung (Chapter 3) and to Ge(Li) measurements by Kang (Chapter 5).

Finally, based upon both the present work and comparable experimentation by others, the useful range of the subject spectrometers appears to terminate somewhere in the 1 to 10 keV range. Neutron energy distributions below 10 keV are of considerable interest, however, particularly in terms of U^{238} capture and resonance self-shielding. Thus it does not appear that exclusive use of instrumental spectrometers can suffice in the present application, but foil activation methods must also be employed in this sub-keV-region.

4.4 References

(1) Bennett, E. F., "Fast Neutron Spectroscopy by Proton-Recoil Proportional Counting," NSE, 27, 16-27 (1967).

5. ANALYSIS OF BLANKET NEUTRONICS USING GAMMA SPECTROMETRY

C. S. Kang and N. C. Rasmussen

Direct measurement of the prompt and decay gamma spectra emitted by a blanket using a high resolution Ge(Li) spectrometer makes possible a number of novel and useful techniques for investigation of the behavior of neutrons in the blanket medium. These applications are the subject of the present chapter and the forthcoming topical report:

> C. S. Kang, N. C. Rasmussen and M. J. Driscoll, "Use of Gamma Spectroscopy for Neutronic Analysis of LMFBR Blankets," COO-3060-2, MITNE-130.

5.1 Introduction

It was the purpose of the present investigation to extend and apply gamma-ray spectroscopy using lithium-drifted germanium detectors to the study of fast reactor blankets. The focal point for this research is the Blanket Test Facility (BTF) at the M.I.T. Reactor (MITR), which is driven by the thermal neutron flux from the MITR thermal column. The present work is concerned exclusively with measurements in Blanket No. 2, a mock-up of a typical large LMFBR blanket.

This work can be divided into four fairly independent applications:

1) determination of neutron reaction rates in LMFBR Blanket No. 2,
2) determination of the hydrogen content of LMFBR blanket materials,
3) determination of the neutron leakage spectrum from Blanket No. 2,
4) gamma-ray dosimetry.

The neutron reaction rates in Blanket No. 2 include capture rates, inelastic scattering rates and the fission rate. Both decay and prompt gamma rays are analyzed. The major constituents contributing useful gamma rays were found to be U^{238}, Na, Cr, Fe and O. One not entirely anticipated result worthy of note was the complete disappearance of the U^{238} prompt capture line at 4.059 MeV, which is so prominent in thermal neutron spectra.

Because of the important effect even small amounts of hydrogen have on the neutron energy spectrum, a careful determination of the hydrogen content of the blanket was necessary. Prompt activation analysis was used to determine the hydrogen content of sodium chromate, which is the major potential carrier for moisture in Blanket No. 2.

Three methods are considered to determine the neutron energy spectrum leaking from Blanket No. 2:

1) an energy shift method using low-Z materials,
2) a prompt activation method, and
3) the germanium atomic recoil method.

The third method is developed in detail and applied to measure the neutron energy spectrum from Blanket No. 2.

In most experiments with Ge(Li) detectors for gamma-ray measurements, the dominance of the Compton recoil continuum in the detectors is regarded as an unwanted and troublesome "background." This feature, however, can be exploited for continuous gamma-ray spectroscopy (1).

5.2 Experimental Apparatus

5.2.1 Blanket Test Facility

The Blanket Test Facility (BTF) is described in Chapter 2, section 2.2. BTF Blanket No. 2 is an accurate mock-up of a typical LMFBR blanket composition. Figure 5.1 shows the schematic plan view of the Blanket Test Facility with Blanket No. 2 in place. The 2-inch-diameter hole, 4 inches below mid-plane, has been drilled through the blanket reflector to provide a beam hole for fast neutron and gamma-ray spectrum measurements. This beam hole is aligned with the holes through four masonite and steel laminated plugs in the port 12CH1 penetrating the shield doors, so that the measurements can be done externally. Lead collimators containing various-sized holes have been made up to fit into the holes of the masonite and steel laminated plugs.

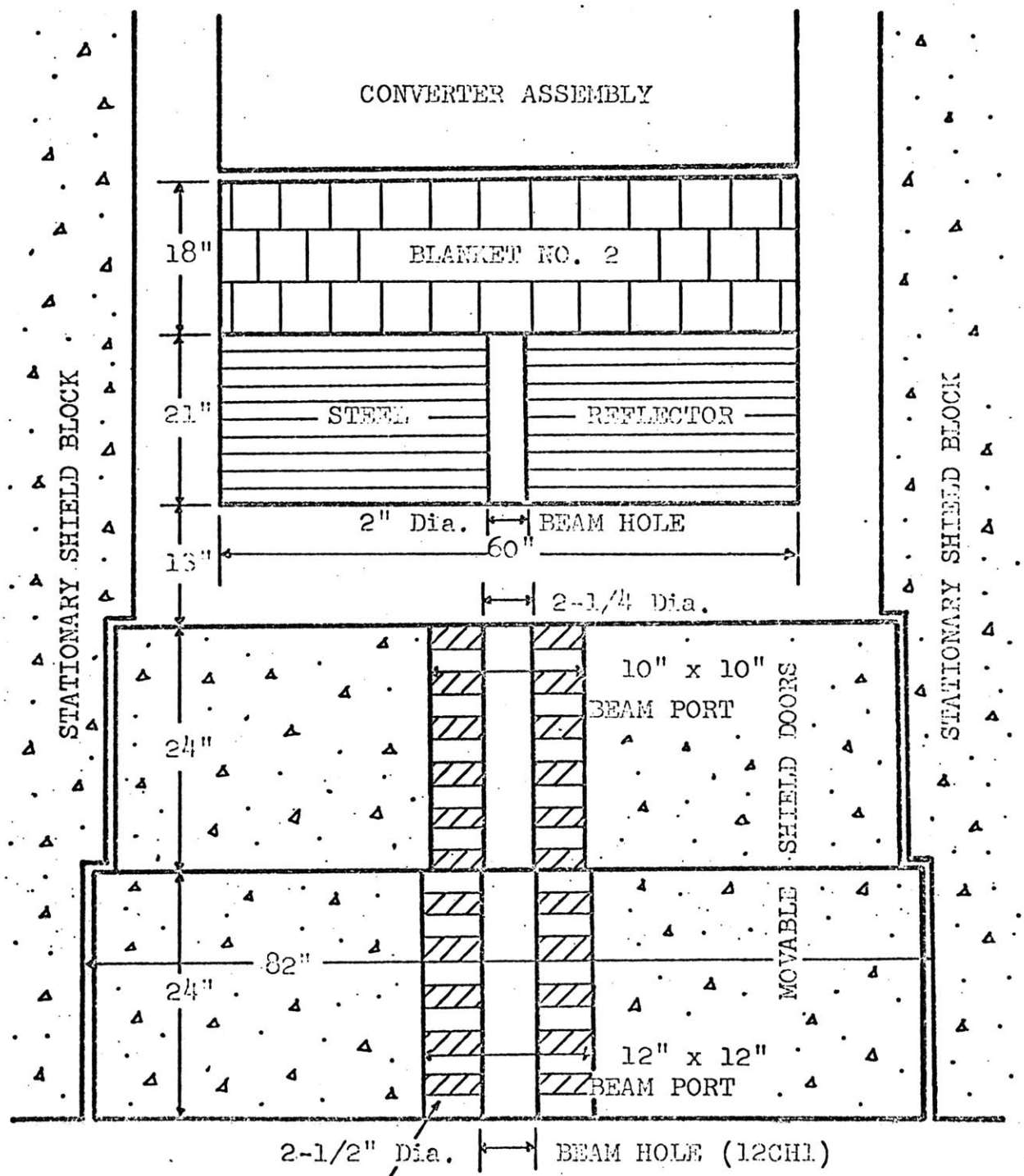

FIG. 5.1 Schematic Plan View of Blanket Test Facility and Blanket No. 2

5.2.2 Detectors and Nonlinearity Correction

The main detector used in this work was a Ge(Li) detector having an active volume of 17 cc and a relatively large dead region. The overall efficiency was fairly high and the energy resolution of the detector varied from a full width at half maximum, FWHM, of 3.5 keV to 7 keV for gamma-ray energies of 511 keV and 7724 keV, respectively. The free mode method of operation was used throughout the work. No gating of the analyzer was done, and no coincidence or timing of the detected pulses was carried out. Figure 5.2 shows a plot of the measured linearity correction factor versus channel number obtained through the subroutine LINEAR of the GAMANL code (4) for the various gain settings of the main amplifier.

Most data were analyzed using the computer code GAMANL (4) and plotted using the CAL-COMP provided by the M.I.T. Information Processing Center.

5.3 Determination of Neutron Reaction Rates in LMFBR Blanket No. 2

The neutron reaction rates of interest may be categorized as capture, scattering and fission rates. The capture rate may be obtained by analyzing the prompt capture gamma rays and short-lived decay gamma rays from the blanket. Inelastic scattering rates, using the characteristic prompt inelastic gamma rays, and the fission rate, using the short-lived fission product decay gamma rays, are also analyzed. Blanket No. 2 is mainly composed of U^{238}, Na, Cr, Fe and O. By analyzing various gamma rays from Blanket No. 2, one can determine the reaction rates of these major blanket constituents. The results can then be compared with the values obtained using foil activation methods.

The disappearance of the U^{238} prompt capture lines made it difficult to deduce the capture rate of U^{238} in the blanket. However, observation of many short-lived decay gamma-ray lines from Np^{239} provided an alternate method for obtaining the capture rate of U^{238}. Prominent Na peaks in both prompt and decay gamma-ray spectra enable one to inter-normalize the prompt and decay gamma-ray data and synthesize the results into a single neutron balance.

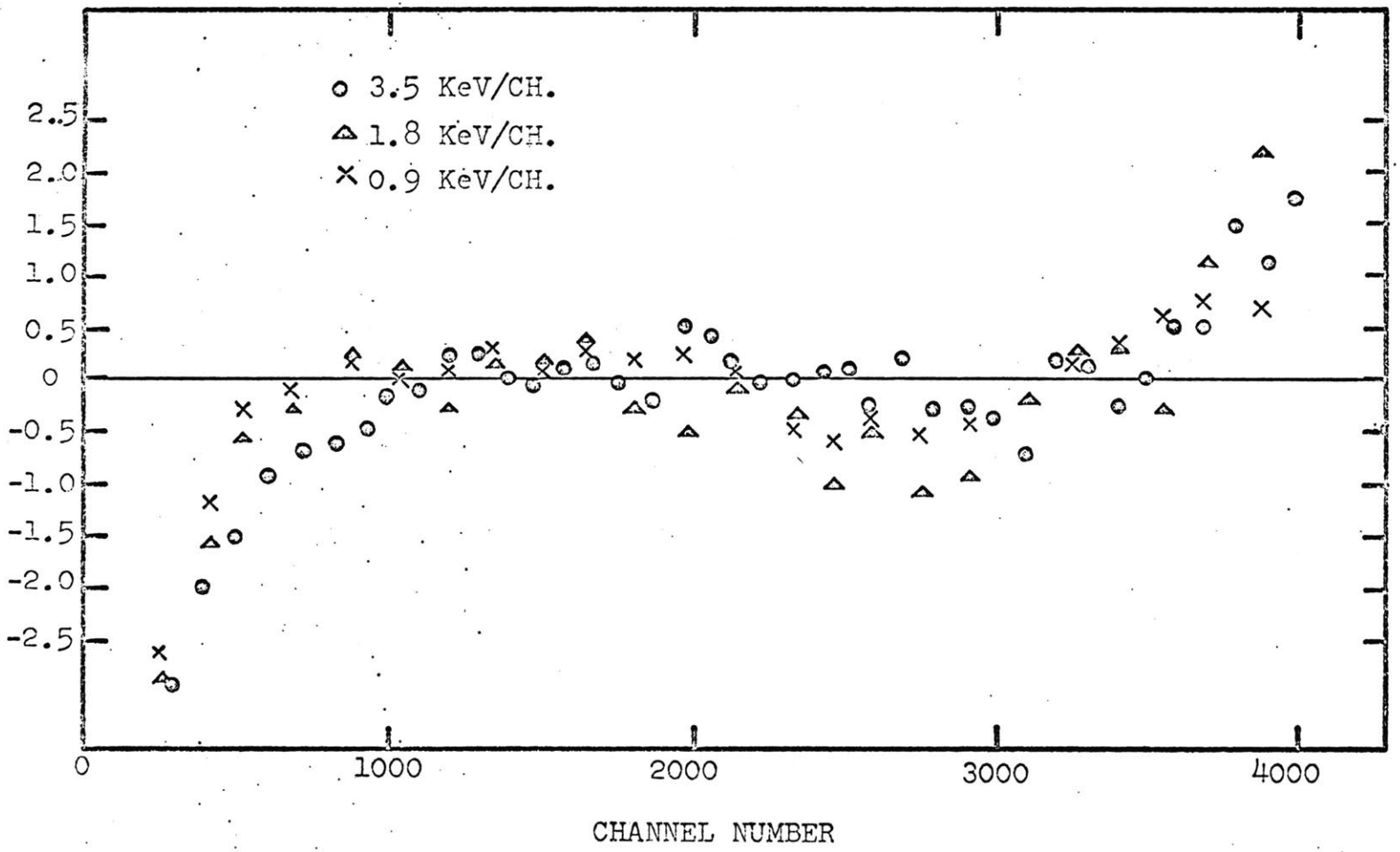

Fig. 5.2 Linearity Correction as a Function of Channel Number for Free Mode Operation

5.3.1 Reaction Rates from Capture Gamma Rays

The reaction rate in an element of interest can be related to the capture gamma-ray intensity in the following way. The number of prompt gamma rays of interest with energy E_γ produced per second at the position x in the blanket is given by the following equation (refer to Fig. 5.3):

$$C_\gamma(x) = \int_E N \frac{I_\gamma(E)}{100} \sigma(E)\, \phi(E, x)\, dE, \tag{5.1}$$

where

$I_\gamma(E)$ is the number of prompt gamma rays with energy E emitted per 100 neutron reactions of energy E,

N is the number of target nuclei of interest per cc of the blanket,

$\sigma(E)$ is the neutron cross section for a certain reaction of the element of interest at the neutron energy E, and

$\phi(E, x)$ is the one-dimensional axial neutron flux having energy E at the position x in the blanket.

Assuming a constant $I_\gamma(E)$ and the separability of variables for the neutron flux, $\phi(E, x) = \phi(E)\psi(x)$, and defining the average reaction rate as follows,

$$R \equiv \int_E N\, \sigma(E)\, \phi(E)\, dE, \tag{5.2}$$

one can express the total area of the gamma-ray peak of interest with energy E_γ observed by the detector during the time interval, T, as follows:

$$A_\gamma = R \cdot \left(\frac{I_\gamma}{100}\right) \cdot S_\gamma \cdot T \cdot C_\gamma \cdot F_\gamma \cdot \Omega, \tag{5.3}$$

where

$$S_\gamma = \int_0^{X_B} \phi(x)\, S_\gamma(x)\, dx, \tag{5.4}$$

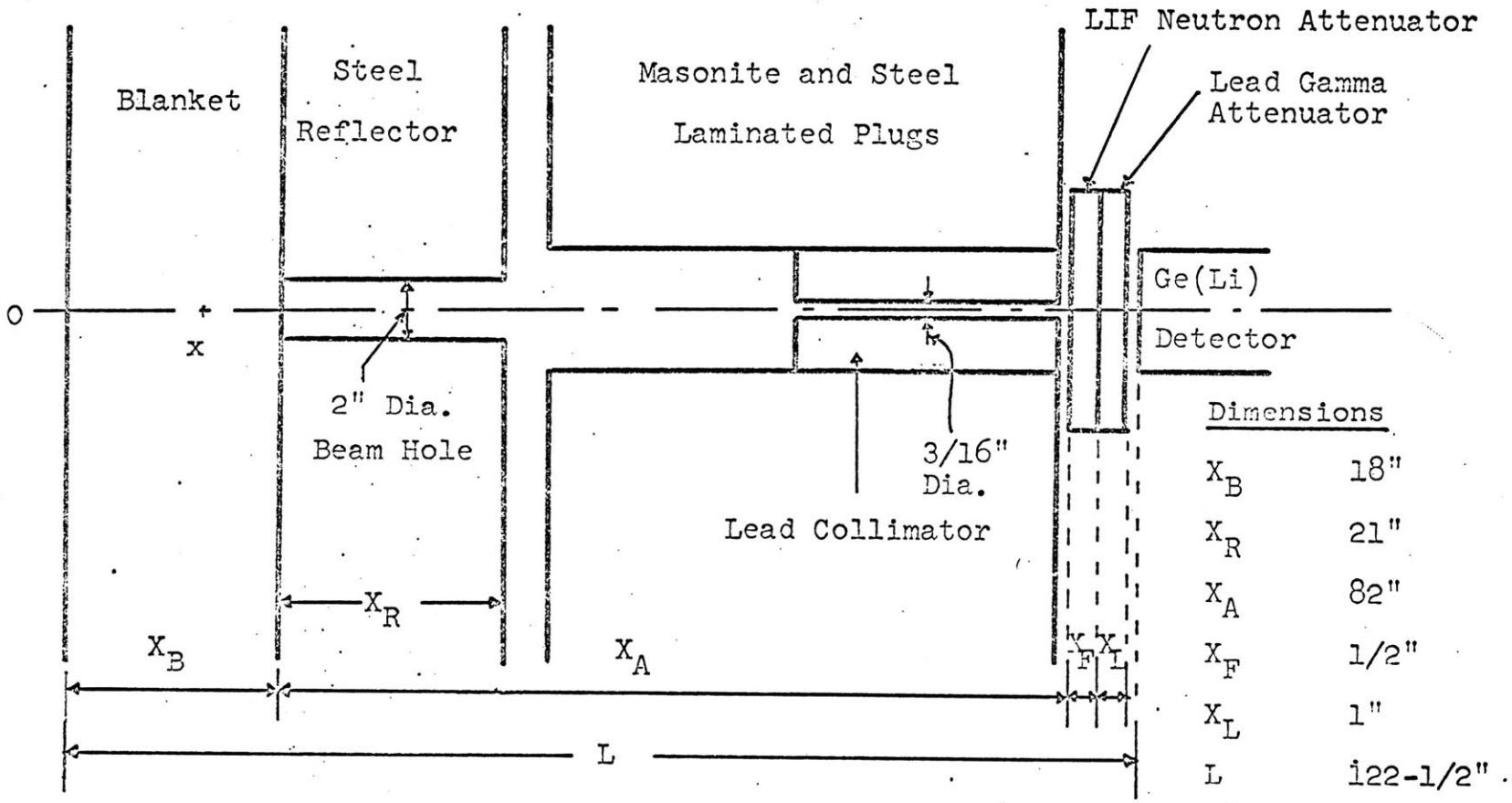

Fig. 5.3 Schematic Overall Plan View of Blanket No. 2 and Detection Setup

C_γ is the intrinsic detection efficiency of the Ge(Li) detector and the associated electronics for gamma-ray energy E_γ,

F_γ is the correction factor for attenuation of gamma rays with energy E_γ by air or any other materials placed in the flight path of the gamma-ray beam from the blanket surface to the detector,

Ω is the geometric solid angle correction factor, and

$S_\gamma(x)$ is the correction function for self-absorption of gamma rays with energy E_γ in the blanket, which is a function of position.

5.3.2 Prompt Capture Gamma-Ray Detection Efficiency

The total detection efficiency of a gamma ray of energy ε_γ is defined by:

$$\varepsilon_\gamma = S_\gamma \cdot F_\gamma \cdot C_\gamma \cdot \Omega. \tag{5.5}$$

When dealing with high-energy, prompt capture gamma rays (hence, when heterogeneous effects are inconsequential), the total efficiency of the setup is readily determined experimentally and one can avoid complicated calculations. Figure 5.4 shows the total efficiency curve for the detection system, which is obtained from the iron prompt capture gamma-ray data from Blanket No. 2, employing the yield intensity for thermal neutrons. Note that the observed total efficiency data lie on the efficiency curve for thermal neutron capture except for a few of the peaks.

5.3.3 Reaction Rates from Decay Gamma-Ray Measurement

The total area under the decay gamma-ray peak of interest observed by the detector at energy E_γ during the time interval between t_s and t_f is given by the following equation:

$$A_\gamma = R \cdot \frac{I_\gamma}{100} \; S_\gamma \cdot T \cdot C_\gamma \cdot F_\gamma \cdot \Omega, \tag{5.6}$$

where

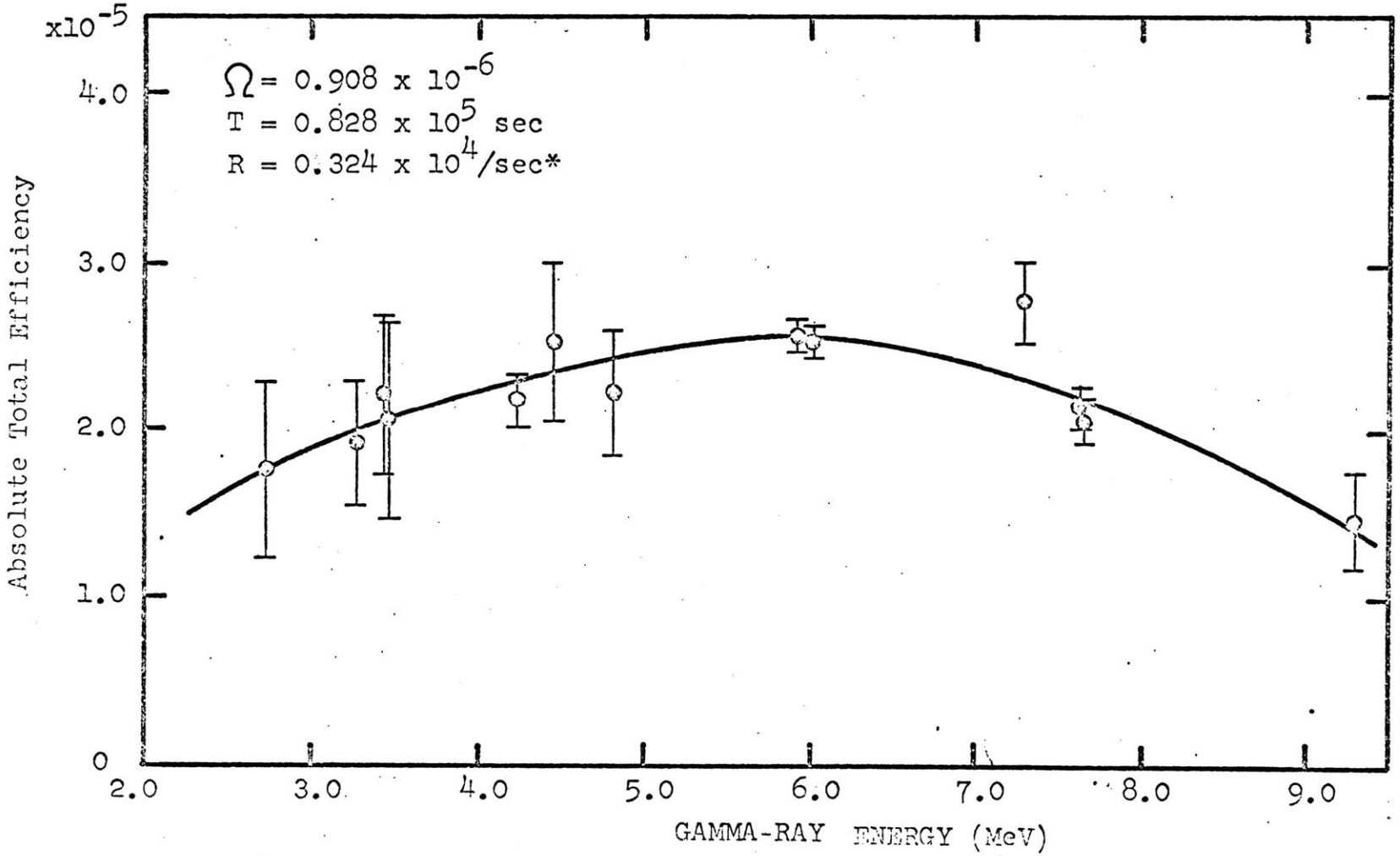

Fig. 5.4 Total Efficiency Curve of Detection System for High Gamma-Energies

(* $R = N \bar{\sigma} \bar{\phi}$: $N = 0.01375$, $\bar{\sigma} = 0.00867$, $\bar{\phi} = 2.72 \times 10^8$)

$$T_{Na} = \int_{t_s}^{t_f} \left(e^{-\lambda_{Na} t} - e^{-\lambda_{Na}(t_1+t)} \right) dt , \tag{5.7}$$

$$T_{Np} = \int_{t_s}^{t_f} \frac{\lambda_{Np}}{\lambda_{Np} - \lambda_U} \left(e^{-\lambda_U t} - e^{-\lambda_U (t+t_1)} \right.$$

$$\left. + \frac{\lambda_U}{\lambda_{Np}} e^{-\lambda_{Np}(t+t_1)} - \frac{\lambda_U}{\lambda_{Np}} e^{-\lambda_{Np} t} \right) dt , \tag{5.8}$$

$$S_\gamma^{Na} = \int_{\Delta V} dv \, \psi(\underline{r}) \, \eta_{Na}(\underline{r}) \, S^{Na}(\underline{r}) , \tag{5.9}$$

$$S_\gamma^{U} = \int_{\Delta V} dv \, \psi(\underline{r}) \, \eta_{U}(\underline{r}) \, S^{U}(\underline{r}) , \tag{5.10}$$

and the remaining terms are the same as previously described. Equation 5.6 is exactly the same as Eq. 5.3 except for the definitions of T and S_γ. In the previous case of the high energy gamma rays, all these factors were combined into a single factor, the so-called total efficiency. But when one deals with low energy gamma rays, the heterogeneity effect does not allow combination of all factors into a single factor, since the self-absorption correction factor will be very different according to where the gamma rays originate. In this situation, Eqs. 5.9 and 5.10 are solved numerically. The self-absorption correction factors for gamma rays from sodium chromate and from uranium fuel rods of Blanket No. 2 are shown in Figs. 5.5 and 5.6. In Fig. 5.6 the calculated factors are compared with values measured using a dummy fuel assembly and an irradiated fuel rod as a gamma source. The intrinsic efficiency data are also obtained by a series of measurements, which are shown in Fig. 5.7.

Two radioactive isotopes, Na^{24} and Np^{239}, are of primary interest in the analysis of the blanket decay gamma-ray spectra. The Na^{24} decay gamma-ray lines at 1368 keV and 2754 keV are used to internormalize the prompt capture gamma rays and the decay gamma rays from Np^{239} in the analysis of the neutron capture reactions.

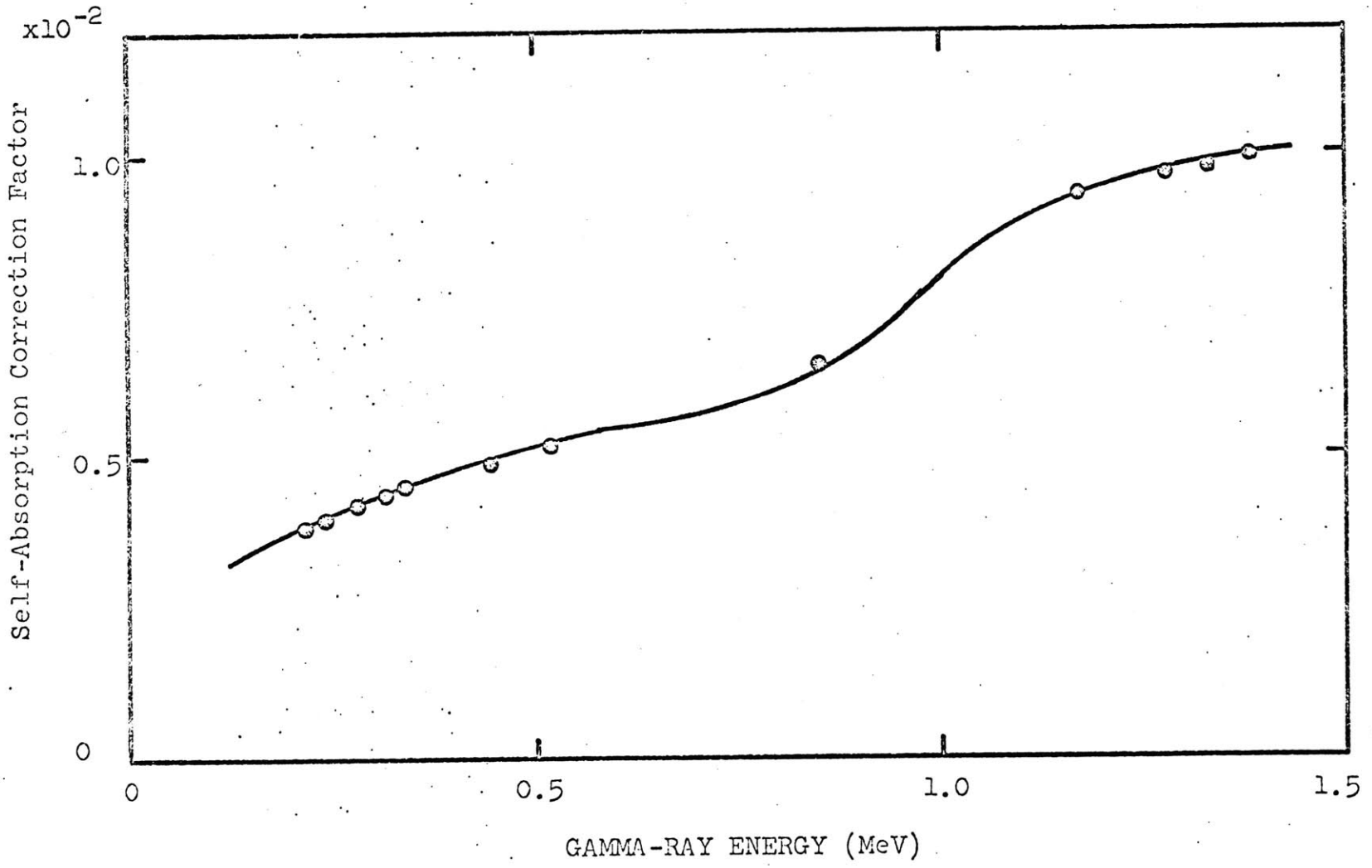

Fig. 5.5 Self-Absorption Correction Factors for Gamma-Rays from Na_2CrO_4 of Blanket No. 2

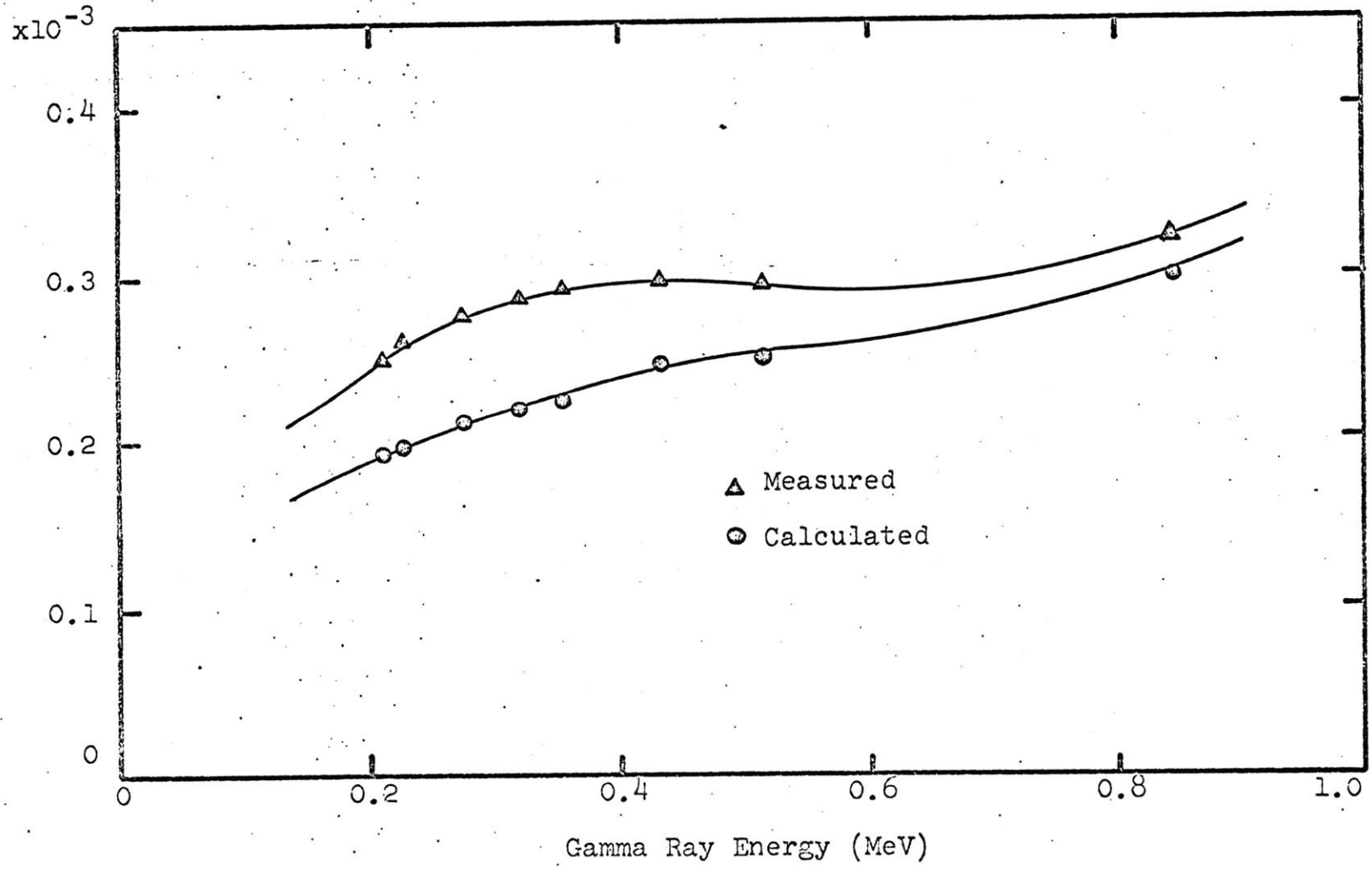

Fig. 5.6 Self-Absorption Correction Factor for Gamma-Rays from U-Fuel Rods of Blanket No. 2

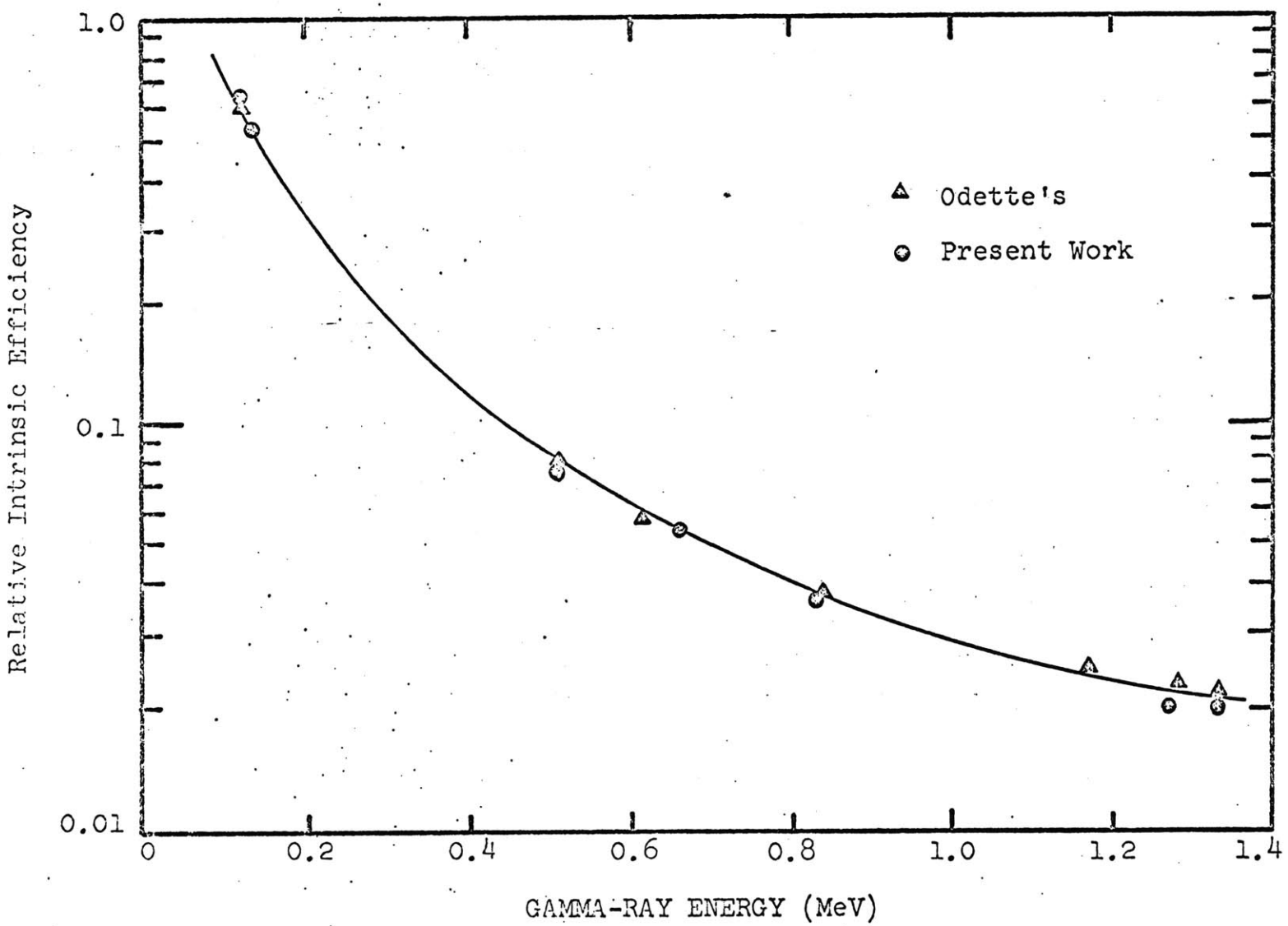

Fig. 5.7 Intrinsic Efficiency of 17 c.c. Ge(Li) Detector

5.3.4 Reaction Rates from Gamma Rays of Inelastic Neutron Scattering

The inelastic scattering process can be analyzed by the measurement of the gamma rays emitted by the excited target nucleus, since every inelastic scattering event is accompanied by the emission of gamma rays, the energies of which correspond to the excited levels of the target nucleus. The energies of the first and the second excited states of the materials of Blanket No. 2 are given in Table 5.1. Since the production cross section of gamma rays, the energy of which corresponds to the first excited state of the target nucleus, is not the same as the inelastic scattering cross section, it is not always true that every inelastic scattering reaction gives one characteristic gamma ray, the energy of which corresponds to the first excited level. However, it is reasonable to assume that the gamma-ray production rate is proportional to the reaction rate itself. Figure 5.8 shows the calculated total efficiency of the system for low energy gamma rays. This efficiency data can be normalized to the measured total efficiency data obtained from iron lines.

TABLE 5.1

Energies of First and Second Excited States*

Nucleus	First Excited State (MeV)	Second Excited State (MeV)
O^{16}	6.05	6.13
Na^{23}	0.438	2.08
Cr^{52}	1.434	2.37
Fe^{56}	0.845	2.085
U^{238}	0.045	0.145

*Nuclear Data Table

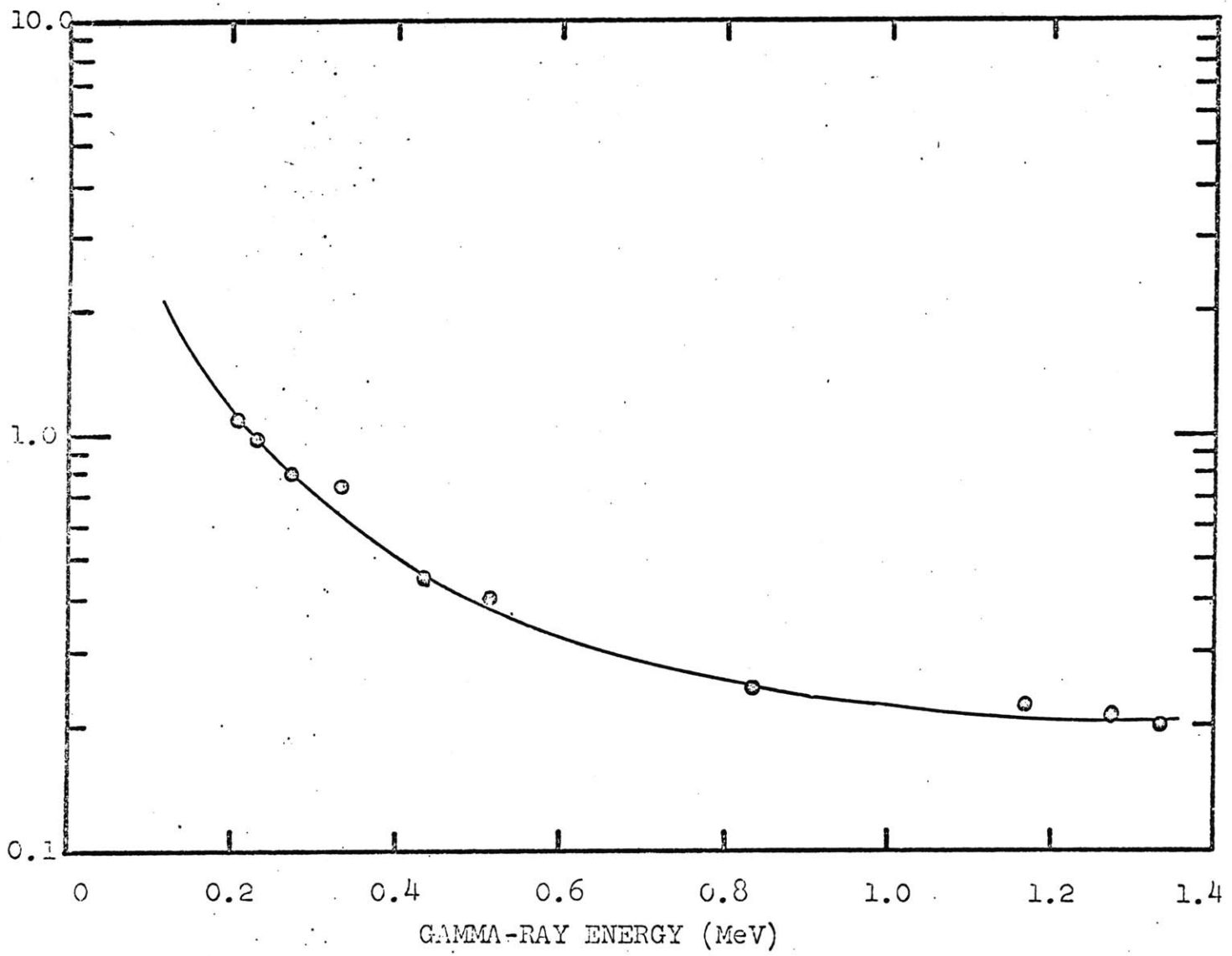

Fig. 5.8 Calculated Total Efficiency for Low Energy Gamma-Rays, Which Originate from Na_2CrO_4

5.3.5 Reaction Rates from Fission Product Gamma Rays

The primary interest here is focused on short-lived fission products in Blanket No. 2 for the purpose of investigating the fission rates in the blanket. The use of long-lived fission products raises the complicated problem of the unknown amount of accumulation of counts due to the increasing inventory of long-lived radionuclides from run to run. The use of exceptionally short-lived fission products, on the other hand, has the problem of poor counting statistics because of the rapid decay. Table 5.2 shows the principal lines used and their corresponding intensity yields. Useful peaks are not chosen solely on the basis of the relative difference in the fission yield of the emitting nuclide or on the basis of the gamma-ray energy. Other parameters must be considered such as the decay constants, the yields of the gamma rays and the half-lives of all the radioactive precursors.

TABLE 5.2

Principal Fission Product Gammas of Interest

Isotope	Energy (keV)	Gamma Yield (Percent)	Area (A_γ)
Sr^{91}	1024.8	30	328.5 ± 19%
Zr^{97}	1146.7	2	144.2 ± 28.1%
Nb^{97m}	743.3	100	1014.7 ± 9.1%
Nb^{97}	658.2	99	1861.6 ± 7.1%
Te^{132}	230.9	100	12485.1 ± 2%
I^{132}	667.1	95	797.8 ± 7.1%
	772.1	82	607.9 ± 17.3%
I^{133}	530.6	100	1112.5 ± 9.8%

5.3.6 Summary

The results are summarized in Table 5.3; they are normalized and compared with theoretical and other experimental values (5) in Table 5.4. The neutron capture rates of iron, chromium, sodium and U^{238}, the inelastic scattering rates of sodium, chromium, iron and oxygen, and the total fission rate in the blanket have been analyzed. All reaction rates are normalized to the self-shielded U^{238} capture rate. The measured iron capture rate is higher than the calculated rate, as might be expected, since iron is a major constituent in the reflector and shielding and background contamination is possible in spite of the good collimation of the gamma-ray beam. The inelastic scattering rates differ from the theoretical results except for those of sodium. This is attributed to the fundamental difference between the inelastic scattering cross section and the gamma-ray production cross section.

It is evident that the subject method is at present subject to large uncertainties, which make it inferior to foil activation techniques in situations where the latter approach is feasible.

5.4 Determination of Hydrogen Content of LMFBR Blanket Materials

Because of the high neutron slowing-down power of hydrogen, moisture which is absorbed or contained in the materials causes moderation of the fast neutrons and an increased population of epithermal neutrons in the blanket. The deleterious effect of hydrogen in the blanket is calculated and discussed in Reference 6. This work investigates the possible application of prompt activation analysis as a method for hydrogen assay.

In most thermal neutron prompt capture analysis carried out at M.I.T., the hydrogen characteristic line at 2.223 MeV is always prominent. The probability of this process ($\hat{\sigma}_c(2200) = 0.332$ b.) is high and the gamma-ray yield is 100%. However, the capture cross section of hydrogen decreases so rapidly with energy that high energy neutrons cannot be effectively used to analyze the hydrogen content in a material.

Two successive measurements, with or without known amounts of hydrogen added, can be used to give precise information on the hydrogen

TABLE 5.3

Reaction Rates in Blanket No. 2

Reaction	Reaction Rate ($\times 10^2$)	Remark (Gamma Rays)
Fe (n, γ)	3.13 - 4.00	More than 20 prompt γ-peaks analyzed
Cr (n, γ)	0.24 - 0.38	835.1-, 7939.3- and 8884.1 keV
Na (n, γ)	0.30 - 0.31	870.6-, 6395.4- and 1368.7 keV
U^{238}(n, γ)	50.7 - 72.7	Np^{239} decay gamma rays at 209.8-, 228.2-, 277.6-, and 334.3- keV
Na (n, n')	2.39 ± 16.7%	438.0 keV
Cr (n, n')	3.33 ± 14.0%	1433.9 keV
Fe (n, n')	16.32 ± 4.5%	845.0 keV
O (n, n')	5.19 ± 16.7%	6127.8 keV
U (n, f)	7.38 - 19.8	Fission product decay gamma rays from Nb^{97m}, Nb^{97}, I^{132} and I^{133}

TABLE 5.4

Neutron Balance in Blanket No. 2

Reaction	ANISN		T. Leung (5)		Present Work**
$U^{238}(n, \gamma)$*	1.0000		1.0000		1.0000
Fe (n, γ)	0.0036		--		0.0346 ± 0.0042
Na (n, γ)	0.0025		0.0022		0.0029 ± 0.0001
Cr (n, γ)	0.0650		0.0740		0.0030 ± 0.0007
$U^{235}(n, \gamma)$	0.0016		--		--
$U^{238}(n, f)$	0.0485	0.1069	0.0520	0.1130	0.1326 ± 0.0612
$U^{235}(n, f)$	0.0584		0.0610		
Na (n, n′)	0.0271		--		0.0232 ± 0.0039
Cr (n, n′)	0.0081		--		0.0324 ± 0.0046
Fe (n, n′)	0.0418		--		0.1590 ± 0.0071
O (n, n′)	0.0001		--		0.0504 ± 0.0084

*All values reported relative to U^{238}.

**Adapted and normalized to T. Leung's data.

content. Samples were irradiated at the thermal neutron beam port 4TH1 of the MITR. Figures 5.9 and 5.10 show the prompt capture gamma-ray spectrum of sodium chromate, which is the only potential carrier of moisture in the blanket, with and without known amounts of hydrogen added. The chromium line at 2.238 MeV is used as a monitor line and Mylar tape is added to give a known amount of hydrogen. The hydrogen content in the undried sodium chromate was found to be 0.77 ± 0.12 w/o. Samples from the dried sodium chromate loaded into the blanket subassemblies were confirmed to be < 0.1 w/o by prompt activation analysis. This measurement was confirmed by a crucible drying method.

This prompt activation method insures the detection of all possible hydrogen in the sodium chromate, such as that in NaOH impurity, a very likely contaminant in sodium chromate. Further assurance of acceptable quality control measures is given by the fact that no H-line was ever detectable in the prompt gamma-ray spectra extracted from Blanket No. 2 during the work described in section 5.3.

5.5 Determination of the Neutron Leakage Spectrum from Blanket No. 2

The evaluation of techniques for the measurement of the leakage neutron spectrum from Blanket No. 2 has focused on three methods:

1) a gamma-ray Doppler energy shift method using low-Z materials,
2) a prompt activation method, and
3) the analysis of Ge internal conversion spectra at 691.4 keV.

The last method is developed for this purpose, and the other two methods will be discussed but briefly.

5.5.1 Atomic Recoil Method

When fast neutrons impinge on a (Ge)Li detector, two spectral lines, at 595 keV and 691.4 keV, undergo broadening in a manner which is not observed when the detector is subjected to a thermal spectrum. These broadened lines at 595 keV and 691.4 keV are produced by the gamma-ray emission of Ge^{74} and the internal conversion of Ge^{72}, respectively, excited by inelastic scattering events

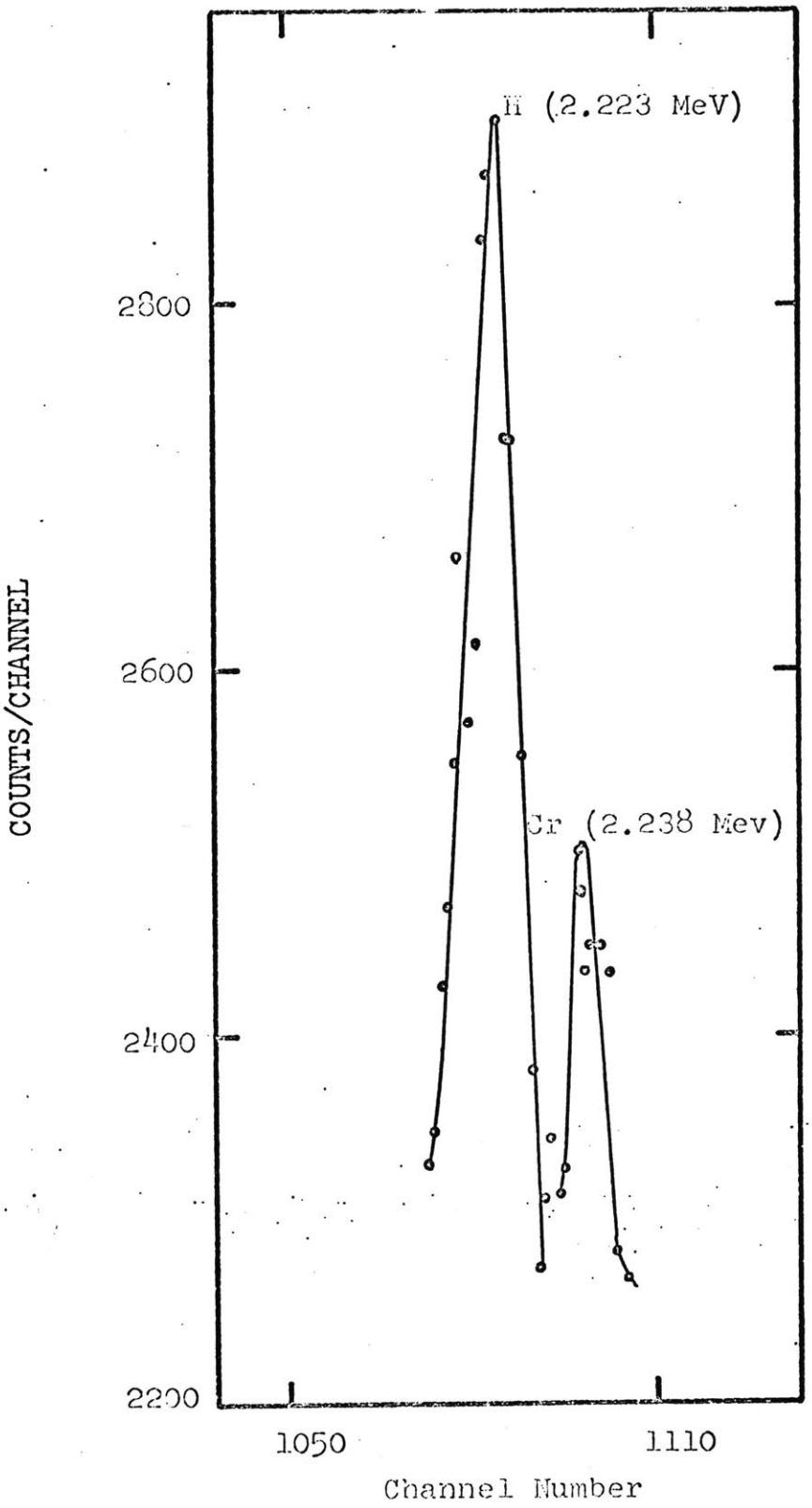

Fig. 5.9 Spectrum of H and Cr of Na_2CrO_4 with Known Amount of Hydrogen Added, Run No. 38

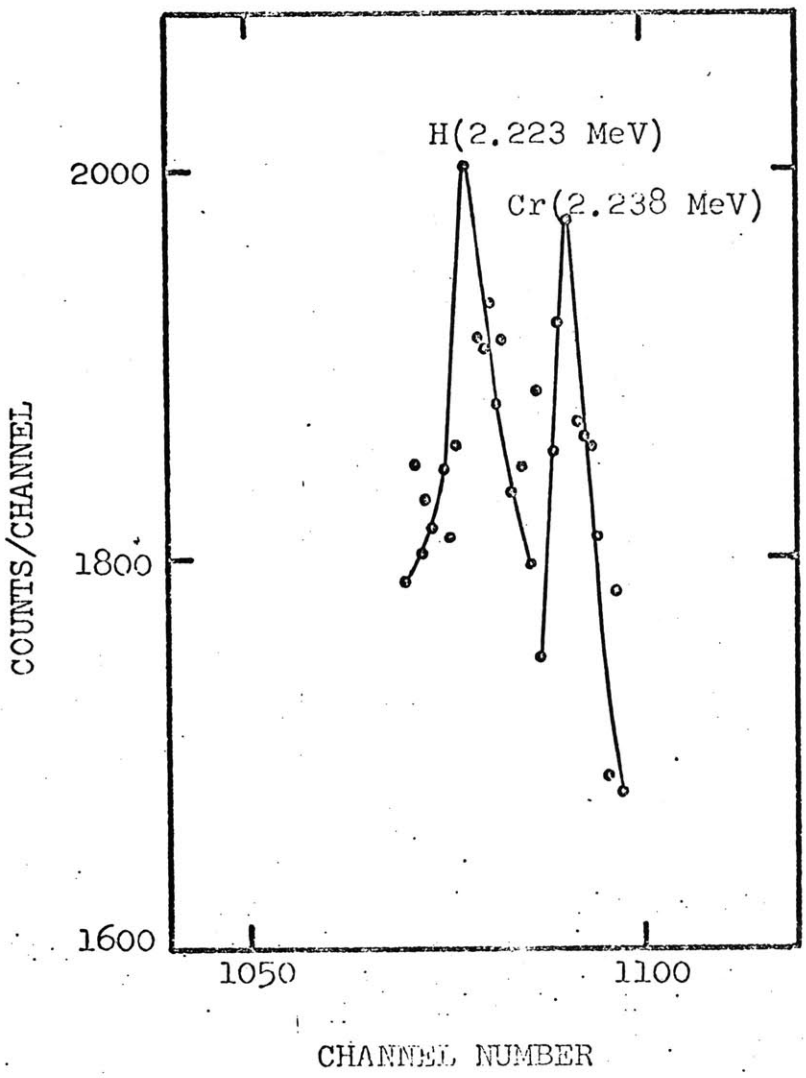

Fig. 5.10 Spectrum of H and Cr of Na_2CrO_4, Run No. 40

with the fast neutrons incident on the Ge(Li) detector. The observed line broadening is the sum of the inelastic scatter gamma-ray energy and the energy of the recoiling Ge atom, since both events occur within the resolving time of the detector. The electronic energy loss of the Ge atoms in germanium is shown in Fig. 5.11. A semi-empirical relationship describing this process is:

$$E'' = a(E')^b \tag{5.11}$$

where

$a = 0.170, \quad b = 1.163,$

E'' is the energy lost to ionization, and

E' is the energy of the recoiling atom.

Now the energy spectrum of the recoil germanium atom is given by:

$$I_R(E') = N \int P(E \rightarrow E')\, \phi(E)\, dE, \tag{5.12}$$

where

N is the total number of Ge^{72} or Ge^{74} nuclei in the detector,

$\phi(E)$ is the neutron energy spectrum, and

$P(E \rightarrow E')$ is the recoiling kernel which can be written as follows:

$$P(E \rightarrow E') = -\frac{2\pi\, \sigma(E, \Theta)}{\sigma(E)} \frac{d\mu}{dE'}, \tag{5.13}$$

where

$d\Omega = 2\pi\, d\mu$

$\sigma(E) = \int_{4\pi} \sigma(E, \Theta)\, d\Omega$, and

$\sigma(E, \Theta)$ is the differential cross section of the germanium nucleus for neutrons having energy E through an angle Θ.

Equation 5.12 can be solved numerically by introducing a matrix representation. The technique used involves correction using the Cf^{252} standard neutron source spectrum and enables one to cover the entire high energy range of the incident neutrons without incurring distortion due to analytical or numerical shortcomings of the unfolding technique.

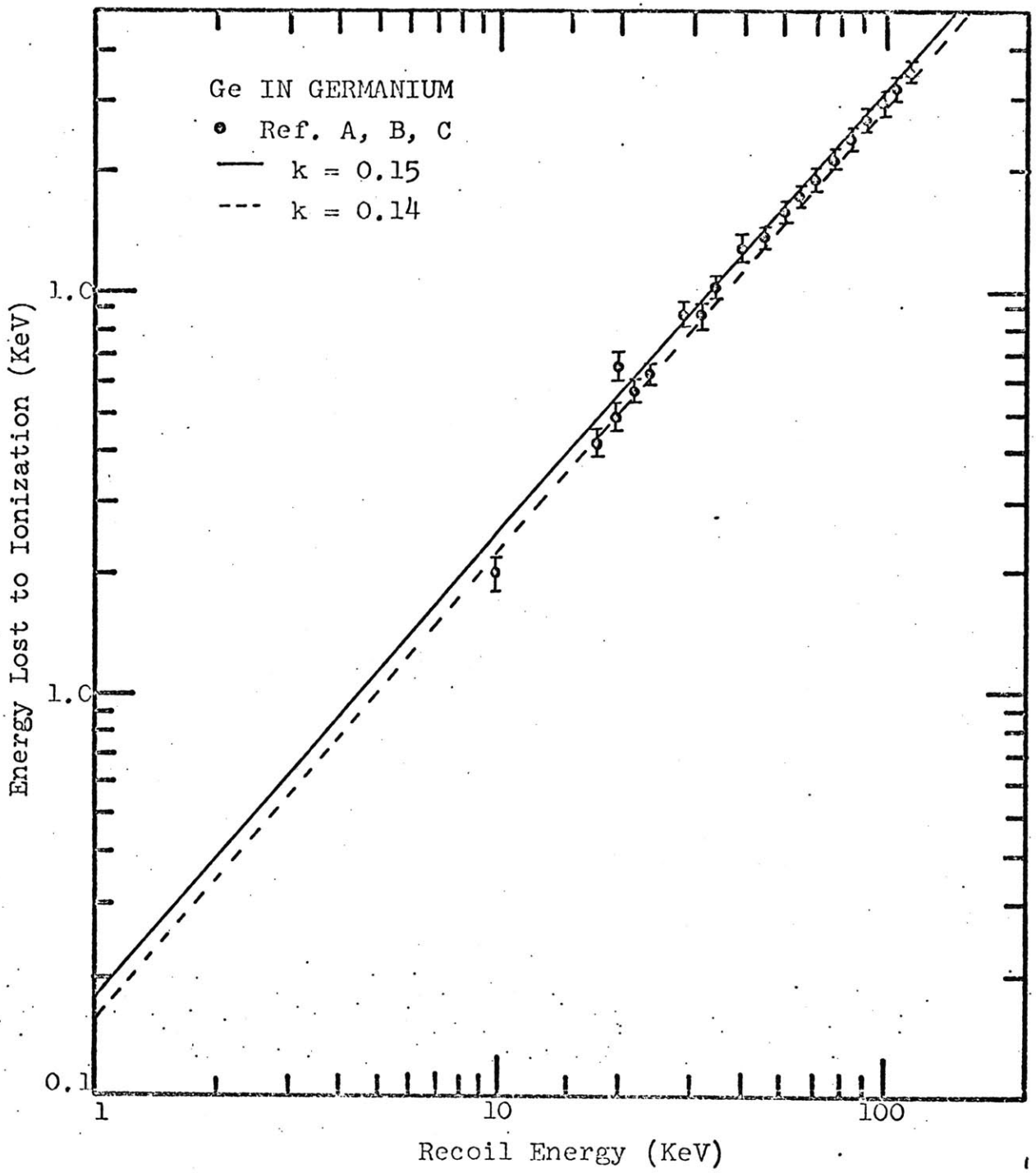

Fig. 5.11 The Energy Lost to Ionization vs. the Recoil Energy of Germanium

Ref. A - Chaseman et al., Phys. Rev. Letters, 20, 1430 (1968)
Ref. B - Chaseman et al., Phys. Rev. Letters, 15, 245 (1965)
Ref. C - Chaseman et al., Phys. Rev. 154, 239 (1967)

Figure 5.12 shows a broadened gamma spectrum at 691.4 keV produced by neutrons leaking from Blanket No. 2. This broadened spectrum from Blanket No. 2 was analyzed with the help of the correction matrix, obtained using the Cf^{252} standard neutron source. The analyzed neutron spectra of Runs No. 107 and No. 106 from Blanket No. 2 are shown in Figs. 5.13 and 5.14.

Since the inelastic scattering event is a threshold reaction, one can only obtain the neutron spectrum above the threshold energy of the reaction. Large depressions at 2.2 MeV and 3 MeV in Figs. 5.13 and 5.14 are also observed in the neutron spectrum in ZPR-3 Assembly 48 deduced by both MC^2 calculation and proton recoil measurement at ANL (7). This is attributable to resonances at these energies. Oxygen, chromium and sodium all have large scattering resonances in this energy range.

5.5.2 Some Other Methods for Extracting Neutron Energy Spectra from Gamma-Ray Spectra

Two additional methods for obtaining neutron energy spectra using gamma-ray spectroscopy were considered: the energy shift method and the prompt activation method.

Consider a neutron of energy En and mass Mn hitting a low-Z target nucleus and being captured by the target, releasing a prompt capture gamma ray. Classical conservation laws for nuclear reactions give the following equation:

$$E = \left(Q + \frac{En}{2}\right) - \frac{1}{4}\,\frac{(Q + En/2)^2}{Mn\,C^2} + \ldots, \qquad (5.14)$$

where the target nucleus is hydrogen and the detector is placed at a 90° angle to the direction of the neutron beam. Hence, the shift of the gamma-ray energy from the thermal capture line at 2.223 MeV depends on the energy of the incident neutrons. This effect may make it possible to deduce the incident neutron energy spectrum.

The second method considered is the prompt activation method. The total gamma-ray intensity of a prompt peak i is given by:

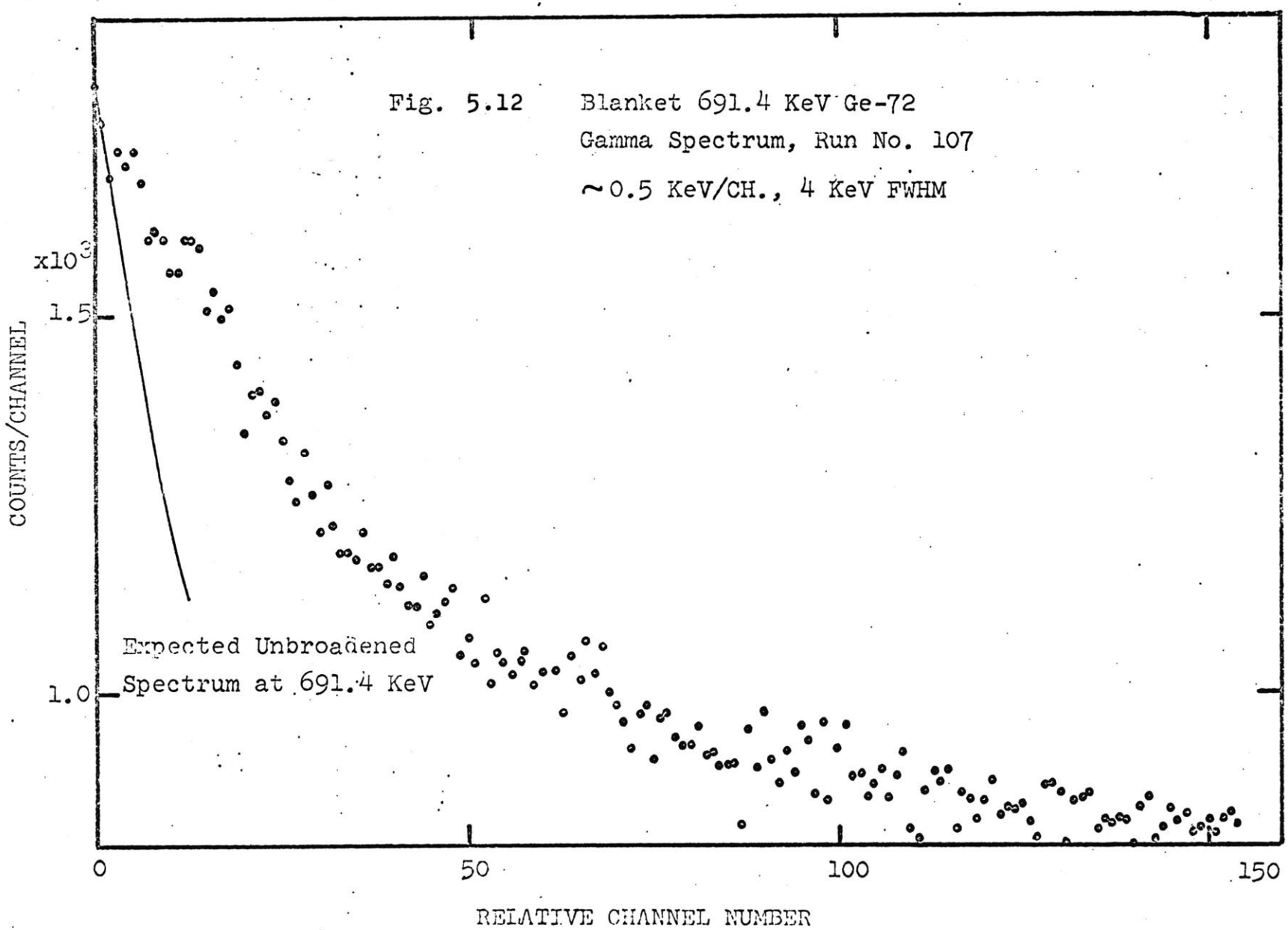
Fig. 5.12 Blanket 691.4 KeV Ge-72
Gamma Spectrum, Run No. 107
~0.5 KeV/CH., 4 KeV FWHM
x10^3
1.5
1.0
COUNTS/CHANNEL
Expected Unbroadened
Spectrum at 691.4 KeV
0
50
100
150
RELATIVE CHANNEL NUMBER

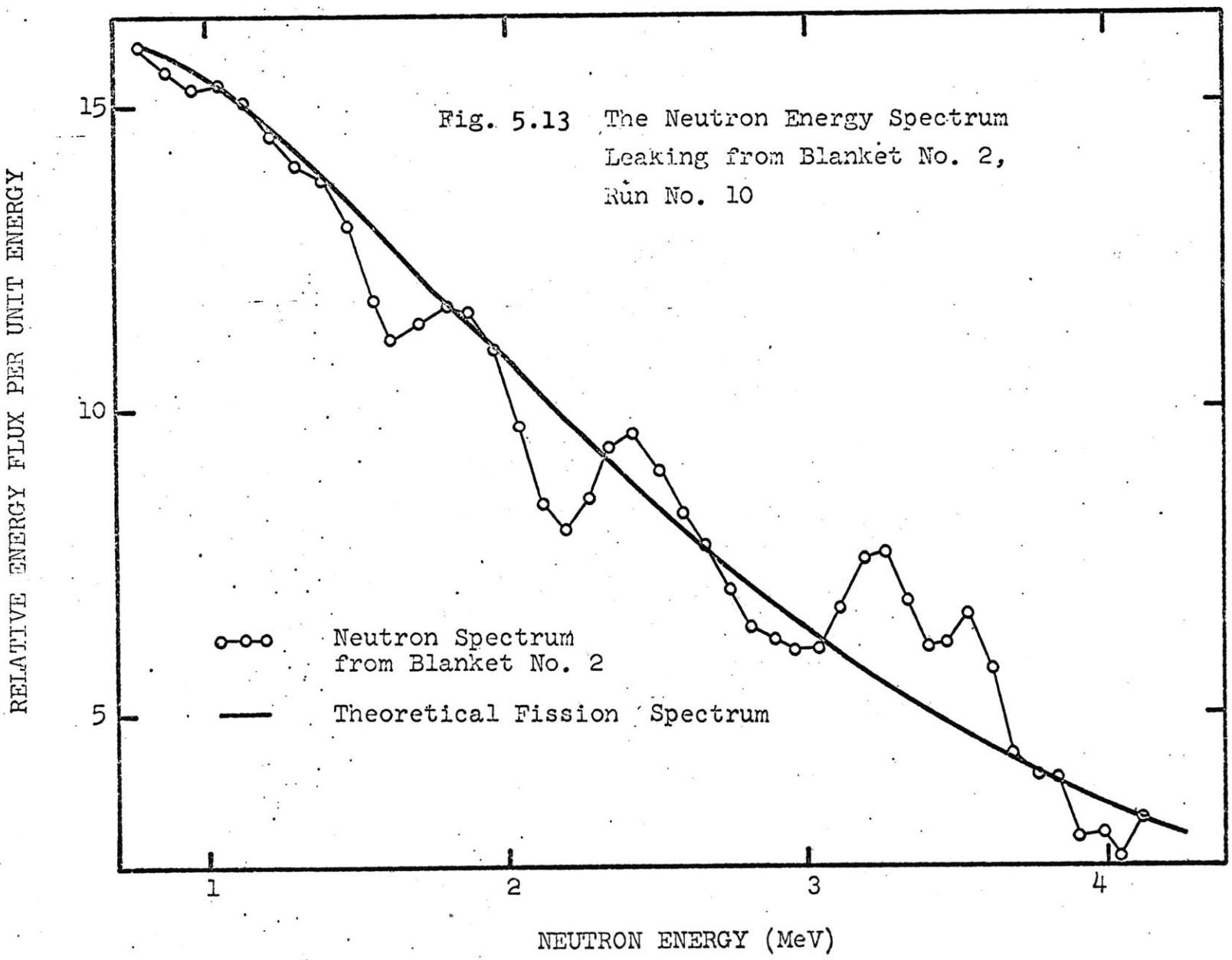

Fig. 5.13 The Neutron Energy Spectrum Leaking from Blanket No. 2, Run No. 10

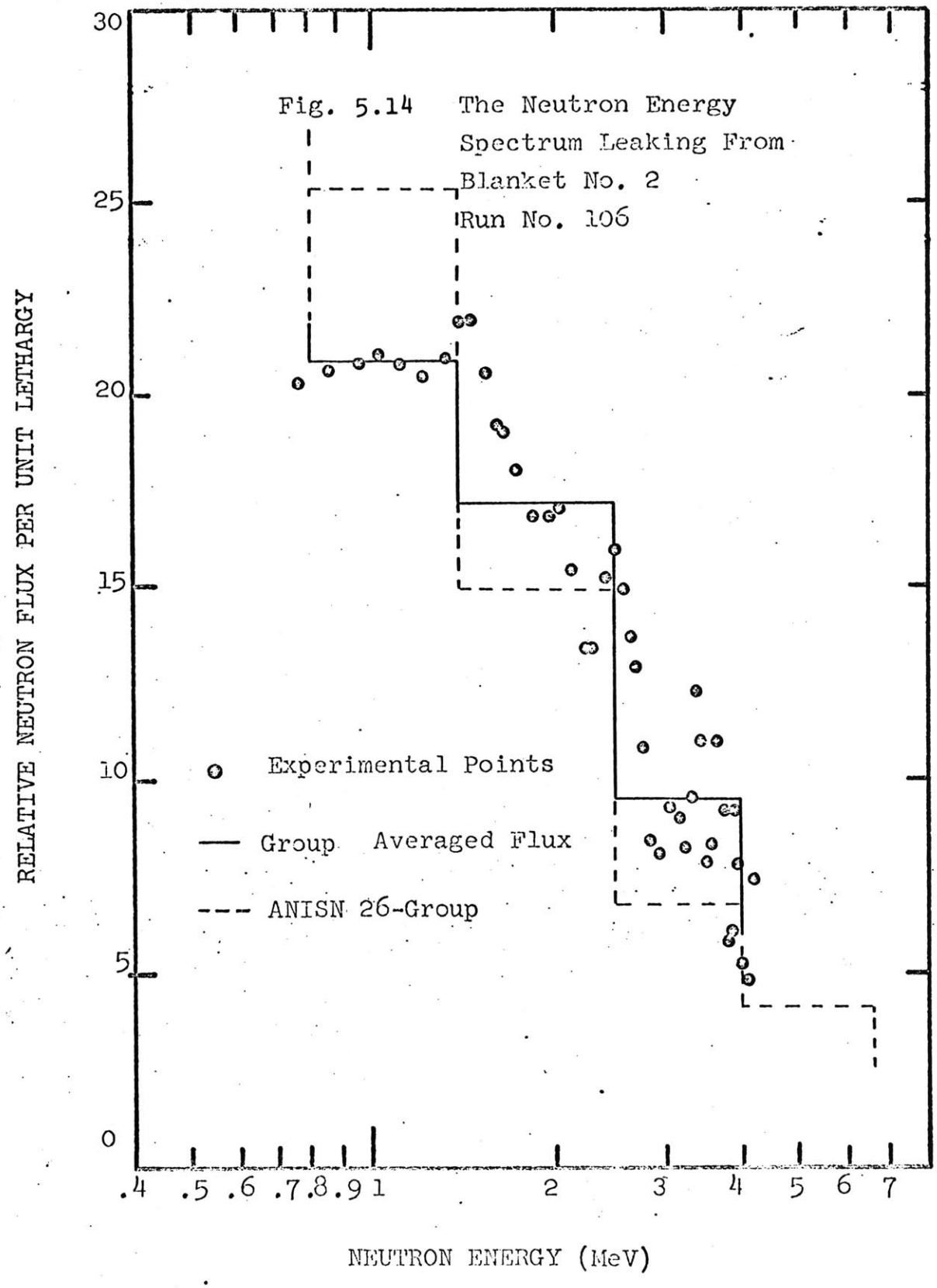

Fig. 5.14 The Neutron Energy Spectrum Leaking From Blanket No. 2 Run No. 106

$$I_i = C_i \int \Sigma_i(E)\ \phi(E)\ dE\ , \tag{5.15}$$

where

C_i is the total efficiency of the detection system for the gamma-ray peak i,

Σ_i is the macroscopic gamma-ray production cross section for the gamma-ray peak i at the neutron energy E, and

$\phi(E)$ is the incident neutron flux.

Equation 5.15 can be solved numerically by introducing a matrix representation. An advantage of the prompt activation method would be that one can use a large number of peaks. Furthermore, if inelastic gammas are analyzed, thermal neutrons no longer interfere with the experiment. Neither of these latter two methods was carried through to the point of practical application.

5.6 Gamma-Ray Dosimetry

The radiation environment of a reactor is not exclusively composed of neutrons. For shielding purposes, it is also important to know the gamma-ray spectrum in the vicinity of the blanket. In most experiments with Ge(Li) detectors for gamma-ray measurements, the dominance of the Compton recoil continuum in the detectors is regarded as a very unwanted and troublesome complication. R. Gold (8), however, showed how this background signal can be exploited to determine the continuous gamma-ray spectrum.

The measured electron recoil spectrum due to Compton scattering of the incoming gamma rays by the Ge(Li) detector is given by:

$$I(E) = \int_{E'_{min}}^{E'_{max}} K(E, E')\ \phi(E')\ dE' \tag{5.16}$$

where

$\phi(E')$ is the total photon flux at energy E', and the function $K(E, E')$ is customarily called the response function of the detection system, which is the well-defined Compton scattering kernel.

This integral equation can be solved with constraints. Using physical constraints imposed by the Compton scattering process, one can deduce an upper triangular matrix as follows:

$$[I] = [K][\phi], \tag{5.17}$$

where

$[I] = \text{col.}\{I_1, I_2, \ldots, I_n\}$,

$[\phi] = \text{col.}\{\phi_1, \phi_2, \ldots, \phi_n\}$, and

$[K]$ is the upper triangular matrix, the elements of which are

$$K_{ij} = \int_{\Delta E'_j} K(E_i, E')\, dE'; \quad j = i, i+1, \ldots N. \tag{5.18}$$

Figure 5.15 shows the continuous gamma-ray spectra leaking from Blanket No. 2, obtained by unfolding the Compton continuum. The photons above 5 MeV originate primarily from prompt neutron capture in the iron, which is the cladding and main structural material in Blanket No. 2, its reflector and the surrounding shielding. Two prominent peaks at 7.632 MeV and 7.646 MeV appear as the most distinct contribution in the high energy spectrum. Above this energy, the gamma flux decreases abruptly. The distribution between 8.5 MeV and 9 MeV is composed of gamma rays from Cr^{54} at 8.881 MeV, plus a possible weak contribution of gamma rays from Fe^{57} at 8.872 MeV. The first bump at ~ 1.2 MeV in Fig. 5.15 is due to the high background gamma ray from Ar^{41} at 1.294 MeV.

5.7 Conclusions and Recommendations

5.7.1 Conclusions

The present work was a study of the application of gamma-ray spectroscopy to investigate fast reactor blankets as part of AEC-sponsored research at M.I.T. This work exclusively focused on analysis of Blanket No. 2, a mock-up of a typical large LMFBR blanket.

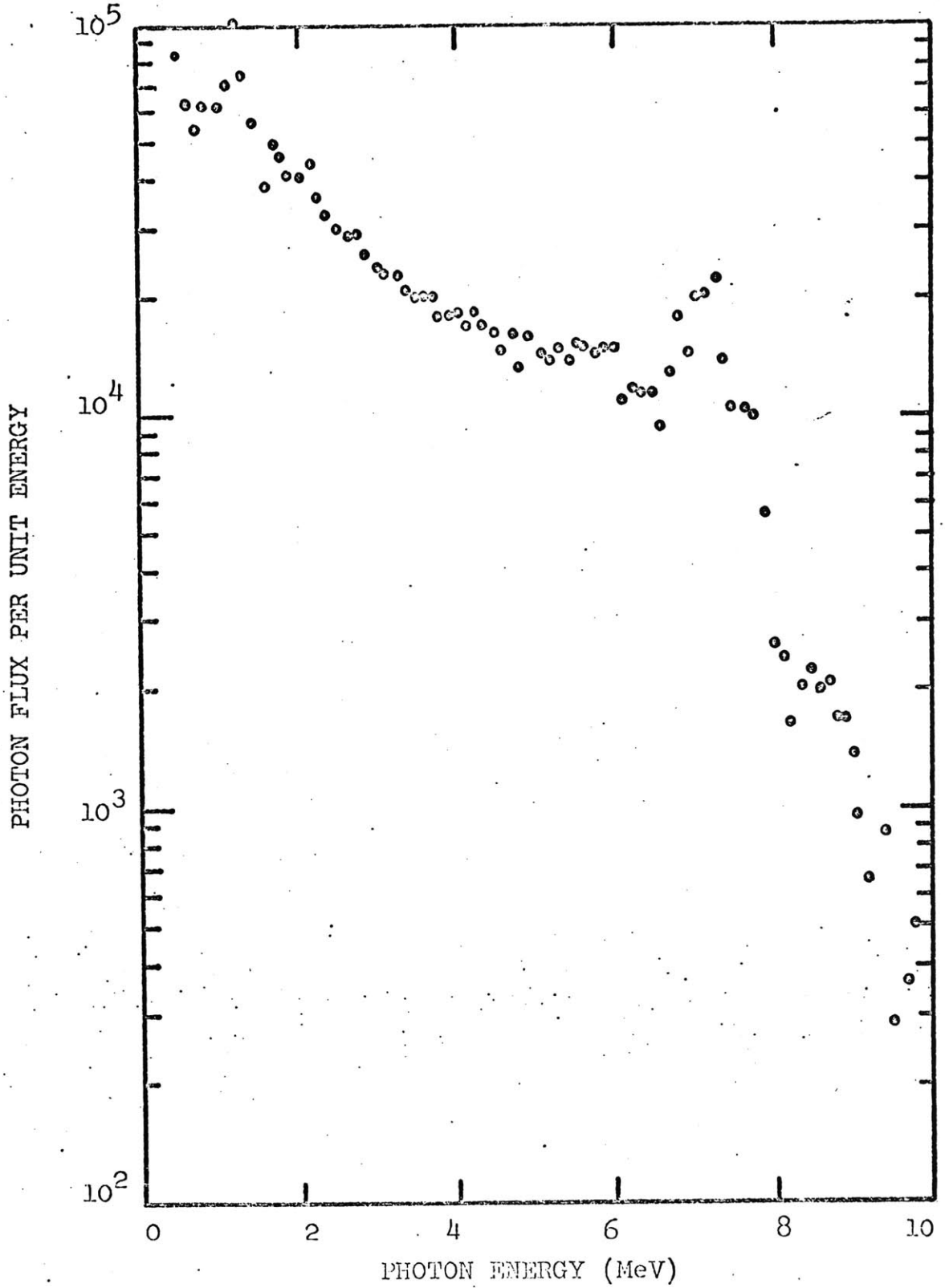

Fig. 5.15 The Gamma-Ray Spectrum Leaking from Blanket No. 2, Run No. 105

The capture reaction rates of blanket constituents in Blanket No. 2 were investigated. Because the U^{238} prompt capture gamma-ray lines could not be detected, the decay gamma rays of Np^{239} were analyzed through calculating the total efficiency, using measured and calculated correction factors and measured intrinsic efficiency data for the detector. Mixed results were obtained: for example, the capture rate of sodium (relative to that of U^{238}) was found to be in good agreement with the calculated value and foil activation measurements, whereas the capture rate of chromium was much smaller than the theoretical and foil activation values.

In addition to the capture rates, the inelastic scattering rates of sodium, chromium, iron and oxygen were obtained as well as the total fission rate in the blanket. The inelastic scattering rates turned out to be quite different from the theoretical results because of the difference between the inelastic scattering cross section and the gamma-ray production cross section. The total fission rate (relative to the U^{238} capture rate) was in good agreement with the theoretical value and foil activation measurements.

All reaction rates were compared on the basis of normalization to the same capture rate in U^{238}. Because of the difficulties involved in the determination of this rate using low energy decay gammas, it is essential to eventually resolve U^{238} prompt capture gamma rays if this approach is really to become useful. It is also necessary to compile a considerable catalog of basic gamma-ray yield data with respect to the captured neutron energy if one is to analyze data with any confidence.

The moisture content of sodium chromate was determined by the thermal neutron prompt activation method, using the 4TH1 irradiation facility of the MITR. This method confirmed less than 0.1 w/o hydrogen contamination of the loaded sodium chromate, consistent with the value determined by crucible drying tests.

It was found that Ge(Li) detectors can be used both as high energy neutron spectrometers and as continuous gamma-ray energy spectrometers. The broadened internal conversion spectral line at 691.4 keV, which is produced by the incident fast neutrons reacting inelastically with the detector nuclei, made possible the inference of

the high energy neutron spectrum. Because inelastic scattering is a threshold reaction, this approach can measure only energy spectra higher than the threshold energy. However, one may conclude that the spectrum is fairly precise and accurate in the high energy region. The Compton recoil continuum, which is usually considered a troublesome background component of the gamma-ray line spectrum, is unfolded to deduce the continuous gamma-ray spectrum leaking from the blanket. These two last applications suggest the possibility of using Ge(Li) detectors as simultaneous neutron-gamma spectrometers in LMFBR shielding studies.

5.7.2 Recommendations

Based upon the results of this investigation, a number of both specific and general recommendations are suggested:

1. It is suggested that in future work at M.I.T. the possibility of using a long-nose dewar to hold the Ge(Li) crystal closer to the blanket be investigated. This will increase the counting rate of the detecting system and reduce the statistical error.

2. It is recommended that a study of prompt capture yield changes of U^{238}, sodium, chromium and other LMFBR constituents be made as a function of neutron energy.

3. It is recommended that further study of the relationship between the gamma-ray production and the inelastic scattering cross section be considered.

4. Further development of the prompt activation analysis approach using inelastic and capture gamma rays to deduce the neutron spectrum is recommended.

5. Analysis and unfolding of the broadened inelastic scattering spectrum of Ge^{74} at 595 keV and comparison with the spectrum unfolded using the 691.4-keV spectral line would appear useful.

6. Development of external target methods to reduce background (especially Fe prompt capture gamma rays, which cause great problems in all spectra) is suggested.

7. Further study of the energy shift method using low-Z materials for measurement of neutron spectra is probably not warranted, based upon its demonstrable low efficiency.

8. Finite size effects of the Ge(Li) crystal (1, 8) should be investigated in more detail with regard to the Compton recoil continuum analysis.

9. It is felt that, before reaction rate determination can be practically applied, it will be necessary to successfully extract U^{238} prompt neutron capture lines in a fast spectrum.

5.8 References

(1) R. Gold, "Compton Recoil Continuum Measurements for In-Core Gamma-Ray Spectroscopy," Reactor Physics Division Annual Report (July 1, 1967 - June 30, 1968), ANL-7410, pp. 373-377.

(2) R. Heath, et al., "Instrumental Requirements for High-Resolution Gamma-Ray Spectroscopy Using Ge(Li) Detectors," IEEE Trans. Nucl. Sc., NS-13, 445 (June 1966).

(3) V. Orphan and N. Rasmussen, "Study of Thermal Neutron Capture Gamma-Rays Using a Ge(Li) Spectrometer," MITNE-80 (January 1967).

(4) N. Rasmussen, T. Harper, Jr. and T. Inouye, "GAMANL, A Computer Program Applying Fourier Transforms to the Analysis of Gamma Spectra," MIT-3944-2, MITNE-97 (August 1968).

(5) T. Leung, M. Driscoll, I. Kaplan and D. Lanning, "Neutronics of a LMFBR Blanket Mockup," COO-3060-1, MITNE-127, to be issued.

(6) I. Forbes, M. Driscoll, T. Thompson, I. Kaplan and D. Lanning, "Design, Construction and Evaluation of a Facility for the Simulation of Fast Reactor Blankets," MIT-4105-2, MITNE-110 (Feb. 1970).

(7) T. Yule and E. Bennett, "Measured Neutron Spectra in a Number of Uranium and Plutonium-Fueled Reactor Assemblies," Nucl. Sci. and Eng., 46, 236-243 (1971).

(8) R. Gold, "Compton Recoil Gamma-Ray Spectroscopy," Nucl. Inst. and Meth., 84, 176 (1970).

6. NEUTRON SPECTRUM DETERMINATION BY PROMPT GAMMA SPECTROMETRY

C. W. Forsberg

6.1 Introduction

The objective of the research reported in this chapter was the evaluation of a new type of neutron spectrometer based upon measurement and analysis of the prompt gamma-ray spectrum emitted following neutron absorption in an appropriate target. Operation of this spectrometer is based on the variation of prompt capture gamma-ray yields with incident neutron energy.

A simultaneous-equation solving program was used to find the neutron spectrum, given the measured prompt-neutron capture-gamma-ray spectrum of a target material, the target material's neutron absorption cross section as a function of energy, and the variation of the intensities of selected gamma rays emitted by the target as a function of the incident neutron energy. Numerical tests were carried out to demonstrate the validity of the unfolding technique.

Apparatus was built to extract the prompt gamma spectra of the chosen target material, tantalum-181, from a fast reactor blanket mock-up. The designed-for Ta^{181} photopeak signal intensities were eventually achieved; however, high background degraded the statistical precision of these measurements sufficiently to prevent attainment of accurate final results. Information pertinent to the achievement of further improvements in equipment design was developed.

It is concluded that a neutron spectrometer based upon this principle is feasible, given foreseeable improvements in experimental technique.

6.2 Principle of Operation

The spectrometer is designed to make use of the well-known fact that prompt capture gamma yields vary with the energy of the captured

neutrons. It is therefore possible, in principle, at least, to deduce the energy distribution of the incident neutrons from the measured yield of prompt capture gammas emitted by a target. Mathematically, we have:

$$\Gamma_i = \int_0^\infty Y_i(E)\ \Sigma(E)\ \phi(E)\ dE, \tag{6.1}$$

where

Γ_i = production rate of gamma rays having i^{th} discrete energy (per cc of target),

$Y_i(E)$ = yield of group i gammas as a function of neutron energy, E,

$\Sigma(E)$ = (n, γ) cross section of target material,

$\phi(E)$ = ambient neutron flux immersing target.

Equation 6.1 is readily transformed into discrete form by replacing the integral by a sum over a number of energy groups, j. It can then be solved for the neutron group flux vector given Γ_i, Y_{ij} and Σ_j. Thus the problem reduces to selection of a material having suitable physical properties (Y_{ij} and Σ_j), and selection of a detection system to measure gamma intensities, which are proportional to Γ_i.

It will be recognized that experimental data must be corrected for detector efficiency and for gamma self-shielding by the target in order to extract the Γ_i from measured gamma spectra. The former corrections are common to any gamma spectrometry work and are readily made using calibrated standard sources. The self-shielding corrections can be calculated, but experimental determination was envisioned in the present work. Since thermal neutron spectra are readily available, and gamma yields following thermal neutron capture are much better known than for higher neutron energies, the self-shielding factors can be measured by inserting the spectrometer's target into a thermal neutron beam and comparing the measured line intensities to standard, infinitely thin target data.

The two overriding considerations which led to selection of tantalum as the target material were the availability of gamma yield data versus neutron energy (2, 3) and the large cross section for fast neutron capture.

Even so, there is considerable room for improvement evident in the area of gamma yield measurements: better accuracy and more materials need to be investigated, particularly for epithermal and fast neutron irradiation. This lack of data and precision is at present one of the major deficiencies in the concept of using prompt gammas for neutron spectrometry.

Given the general approach embodied in Eq. 6.1 and a choice of target material, the research logically fell into two primary categories: investigation of the feasibility of spectrum unfolding and performance of demonstration experiments on a prototype spectrometer.

6.3 Spectrum Unfolding

A Gaussian elimination program was written in FORTRAN IV language to solve Eq. 6.1 for the neutron energy spectrum, given a gamma-ray spectrum. Numerical studies were conducted on a simple five-group problem: a neutron spectrum typical of an LMFBR blanket was used to generate Γ_i using Eq. 6.1; then this Γ_i vector was employed in the unfolding program. The program was shown to be self-consistent in that it recalculated the neutron spectrum which had been used to derive the input gamma spectrum. Tests were also run in which random "errors" of up to ± 15% were introduced into the gamma intensities.

The results of these numerical experiments can be summarized as follows:

(1) Even with zero random error introduced, it was found that the order of solution of the simultaneous equations of Eq. 6.1 was important. Accumulated round-off errors can lead to unacceptable solutions, which, however, are almost always immediately obvious – e.g., large negative group fluxes. Thus this problem was easily bypassed by solving the same problem a number of times after shuffling the sequential order of the i equations. Correct solutions were then identified as being those which were all-positive and which were also duplicated (within a small error limit) for several different shuffles.

(2) As random input data errors approached ± 10%, the number of correct solutions approached zero.

On the basis of these numerical experiments, it was concluded that the (n, γ) neutron spectrometer is a feasible device in that neutron spectra can be unfolded from gamma data of reasonable accuracy. Attention was then focused upon whether, in the particular application at hand, sufficiently accurate experimental measurements were practicable.

6.4 Experimental Measurements

The prototype spectrometer tested was of very simple design. It consisted of a 2-inch-O.D. Al tube, approximately 6 feet long, containing annular lead collimators, and at the in-pile end, a target assembly. The target consisted of a 168-gm, 1.5-inch-diameter, tantalum metal disc, preceded by 0.75 inch of lead to reduce gamma background. At the other end of the tube a Ge(Li) detector was positioned, preceded by a 0.25-inch-thick, borated plastic sheet to reduce neutron background.

The detector, electronics and procedures were essentially the same as developed and applied by other researchers at M.I.T. over the past several years (4) and need no further description here. Likewise, the standard program, GAMANL, was used to analyze the multichannel gamma spectra (5).

The spectrometer was inserted into the 2.0-inch-diameter hole penetrating the reflector of Blanket No. 2 through port 12CH1 in the BTF Facility shield doors. Runs of up to 38 hours' duration were made at full reactor power.

Although 6 to 12 tantalum lines having photopeak intensities $\geq$ 1000 counts were identifiable, the net uncertainty in the data was far too great to permit meaningful analysis due to the extremely low signal-to-background ratio ($\sim$0.05). Experiments were conducted to show that this background was due to Compton-scattered gammas in the beam being analyzed and not to general room background. Likewise, tests of modifications in the collimator design showed that no appreciable improvements were possible by changing the spectrometer design.

Because sufficient signal strength was realized which would, in the absence of background, make the spectrometer workable, two other alternatives were investigated: the use of an external target and the use of a through-hole.

Extraction of a neutron beam and allowing it to fall upon an external target is an obvious approach to background reduction, since one can arrange the gamma detector so that no strong background source is in its line of sight. This variation was tested, but it was found that the photopeak signal strength achievable was now too low for a practical device.

The second fix, namely, extension of the beam hole completely through the blanket and converter, would also improve matters, again by removing strong sources from direct view of the detector. This approach was rejected as entailing time- and money-consuming expenditures beyond that justifiable.

6.5 Discussion

The results of this work show that the (n, γ) neutron spectrometer is feasible in principle, but that for the particular applications of present interest, the concept proved impractical. In particular, successful application of classical foil techniques using decay gamma counting, discussed elsewhere in this report, obviated the need for pursuit of this approach with any degree of priority. Nevertheless, the (n, γ) spectrometer has many attractive features which may make it suitable for reconsideration by others. For example, given the availability of gamma yield data, it offers the capability for development of a passive spectrometer which interrogates only the self-spectrum emitted by the materials composing an assembly. In any case, it would appear that only applications where neutron source intensity permits use of an external target, or where assembly configuration permits use of a through-port for internal target irradiation, should be considered because of the background problem.

6.6 References

(1) C. W. Forsberg, "Determination of Neutron Spectra by Prompt Gamma-Ray Spectrometry," S.M. Thesis, M.I.T. Dept. of Nucl. Engineering (June 1971).

(2) K. J. Yost, J. E. White, and C. Y. Fu, "Neutron Energy-Dependent Capture Gamma-Ray Yields for U-238 and Ta-181," Trans. Am. Nuc. Soc., Vol. 13, No. 2 (Nov. 1970).

(3) O. A. Wasson et al., "Resonance Neutron Capture in $^{181}Ta(n, \gamma)^{182}Ta$," Nuclear Physics, A132, 161 (1969).

(4) Y. Hukai, N. C. Rasmussen and M. J. Driscoll, "Some Applications of Ge(Li) Gamma-Ray Spectroscopy to Fuel Element Assay," MIT-3944-5, MITNE-113 (April, 1970).

(5) T. Harper, T. Inouye and N. C. Rasmussen, "GAMANL, A Computer Program Applying Fourier Transforms to the Analysis of Gamma Spectra Data," MIT-3944-2, MITNE-97 (August 1968).

7. HETEROGENEOUS EFFECTS IN LMFBR BLANKET FUEL ELEMENTS

P. DeLaquil, III

7.1 Introduction

The primary manifestations of heterogeneity in an LMFBR blanket are the spatial dependence of the U^{238} fission and capture reaction rates within the fuel rods. In an effort to obtain quantitative data on these effects in an environment closely representative of an actual LMFBR blanket, a special subassembly has been built utilizing UO_2 fuel, stainless steel cladding, and metallic sodium coolant. This subassembly can be used in place of one of the standard Na_2CrO_4-filled, uranium metal-fueled, carbon steel clad subassemblies in Blanket Mock-Up No. 2, and the effects of fuel heterogeneity measured using uranium foil activation techniques.

7.2 Description of the Special Subassembly

The special subassembly contains a total of 85 fuel rods arranged on a 0.610-inch triangular spacing; two fuel rods are removable and are designed to permit in-rod foil activation experiments. Each fuel rod contains 1.0999% enriched UO_2 pellets which are 0.430 inch in diameter. The fuel pellets are clad with stainless steel tubing having a 0.500-inch O.D. and a 28-mil-thick wall. Each fuel rod contains 48 inches of fuel pellets. The rods are sealed at each end with stainless steel plugs and are held in place by the upper and lower grid plates. The inter-rod volume is filled with solid sodium metal. The outside subassembly dimensions and active fuel height are exactly the same as those of the standard Na_2CrO_4-filled subassemblies. Figure 7.1 shows the unit cell arrangement in the "sodium" subassembly, which may be compared with that of the standard "chromate" subassembly shown in Figure 7.2. Figures 7.3 and 7.4 show horizontal and vertical sections through the special sodium subassembly.

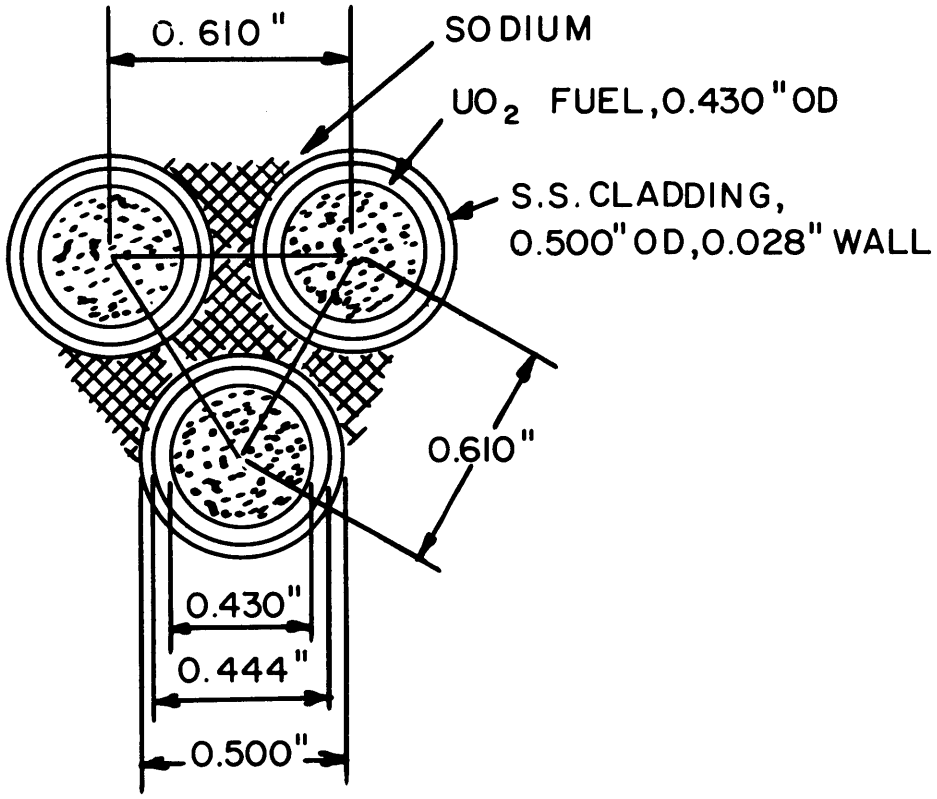

FIG. 7.1 FUEL ROD SPACING IN SPECIAL SODIUM SUBASSEMBLY

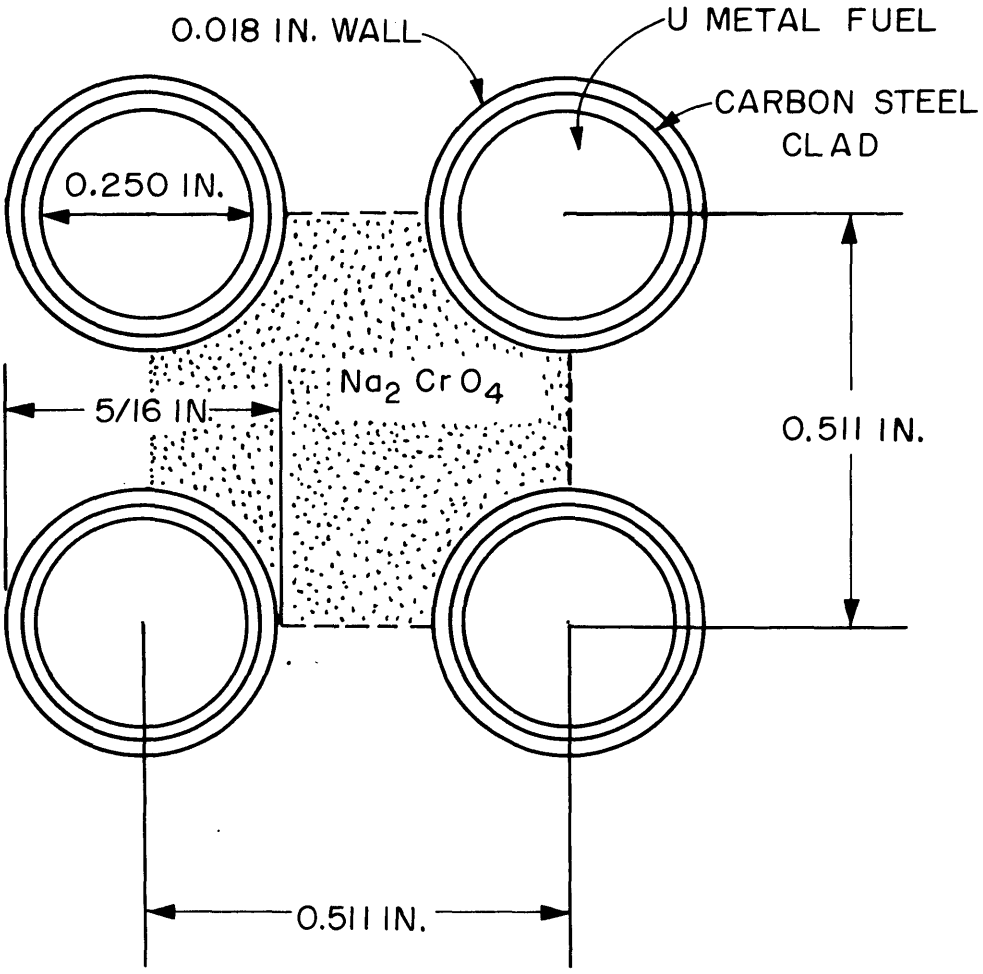

FIG. 7.2 FUEL ROD SPACING IN STANDARD CHROMATE SUBASSEMBLIES OF BLANKET NO. 2

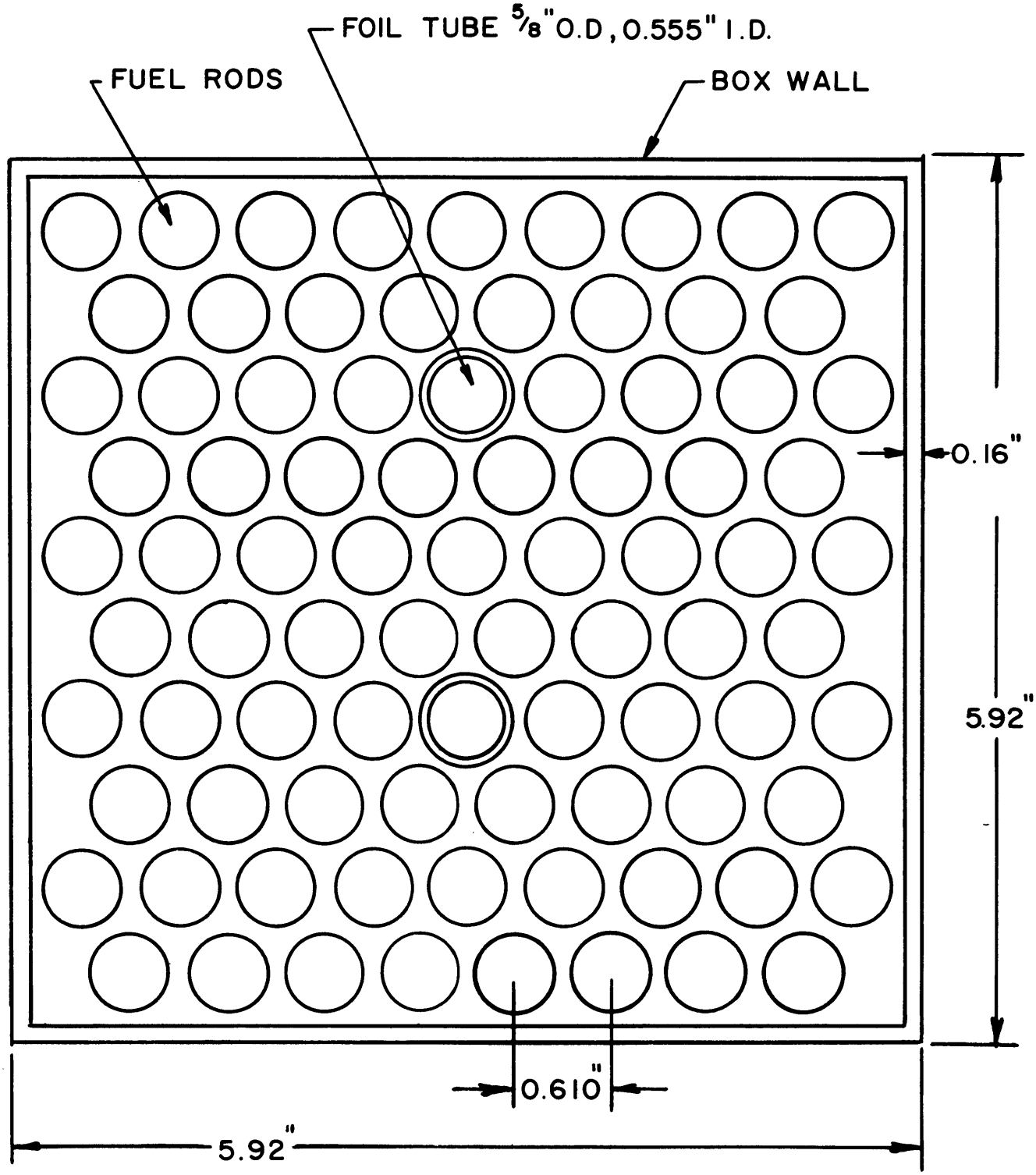

FIG. 7.3 FUEL ARRANGEMENT IN SPECIAL SUBASSEMBLY

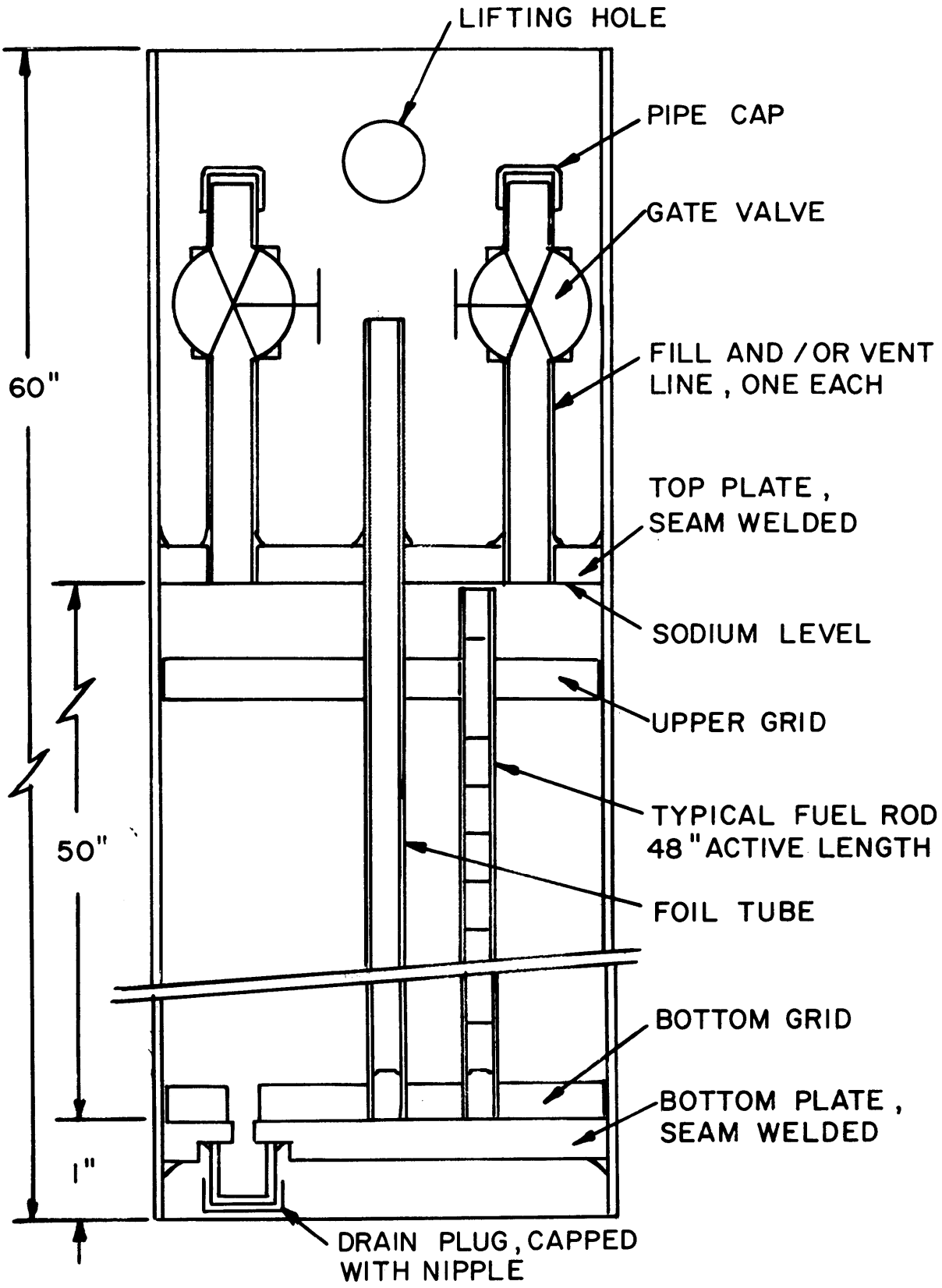

FIG. 7.4 SPECIAL SUBASSEMBLY SECTION VIEW

A standard chromate subassembly of Blanket No. 2, which the above special sodium subassembly is designed to replace, contains 121 fuel rods arranged in an 11 X 11 square lattice on a pitch of 0.511 inch. The fuel rods are 0.250-inch-diameter uranium metal, clad in low-carbon steel tubing having a 5/16-inch O.D. The inter-rod volume is filled with anhydrous sodium chromate powder (Na_2CrO_4). Rods having two different uranium enrichments (1.016% and 1.143%) are loaded in a checkerboard array to give a mean enrichment of 1.08%. Table 7.1 shows a comparison of subassembly weights, and Table 7.2 shows a comparison of homogenized subassembly composition on a nuclide-by-nuclide basis. The composition match is fairly good, although the sodium assembly has more sodium and less uranium than the standard subassemblies.

TABLE 7.1

Comparison of Subassembly Component Weights

Standard Chromate Subassembly		Special Sodium Subassembly	
Uranium metal	89.30 kg	UO_2	88.64 kg
Na_2CrO_4	31.11 kg	Na	10.75 kg
Cladding	13.00 kg	Cladding*	24.06 kg
Subassembly box	26.55 kg	Subassembly box	26.55 kg
Grid plates	0.36 kg	Grid plates	0.58 kg
Grid plate supports	0.91 kg	Valves	1.48 kg
TOTAL	161.23 kg	TOTAL	152.06 kg

*Type 304 stainless steel

TABLE 7.2

Comparison of Homogenized
Subassembly Atom Densities*

Nuclide	Na_2CrO_4 Subassembly		$NaUO_2$ Subassembly	
U-235	0.000088		0.000078	
U-238	0.008108		0.007043	
O	0.016293		0.014242	
Na	0.008128		0.010740	
Cr	0.004064	0.017859	0.001746	0.017309
Fe	0.013750		0.014639	
Ni	0.000000		0.000696	
Mn	0.000045		0.000228	
Si	0.000000		0.000180	
C	0.000096		0.000095	
H	0.000073		0.000000	

*Based on analysis of composition through a cross section at the subassembly mid-plane.

In Table 7.3 the unit cell atom densities are compared: here we have a much closer match than for the subassembly atom densities. Since the subassembly was designed to compare neutronics on the local level, designing to match unit cell composition was considered more important than matching composition on a whole-subassembly basis.

Note should also be taken of the fact that the unit cells in which all foil activations take place differ from the normal unit cells. Figure 7.5 compares the traversing-tube unit cells in the chromate and the sodium subassemblies. Both unit cells contain an extra thickness of clad material in the form of the tube into which the traversing rods are inserted.

TABLE 7.3

Comparison of Homogenized Unit Cell Atom Densities

Nuclide	Special Sodium Subassembly		Na_2CrO_4 Subassembly	
U-235	0.000100		.000098	
U-238	0.009011		.008989	
O	0.018222		.019096	
Na	0.009927		.009529	
Cr	0.002055		.004764	
Fe	0.007462	0.011542	.005042	.009833
Ni	0.000809		.000000	
Mn	0.000216		.000027	
Si	0.000211		.000000	
C	0.000039		.000038	
H	0.000000		.000086	

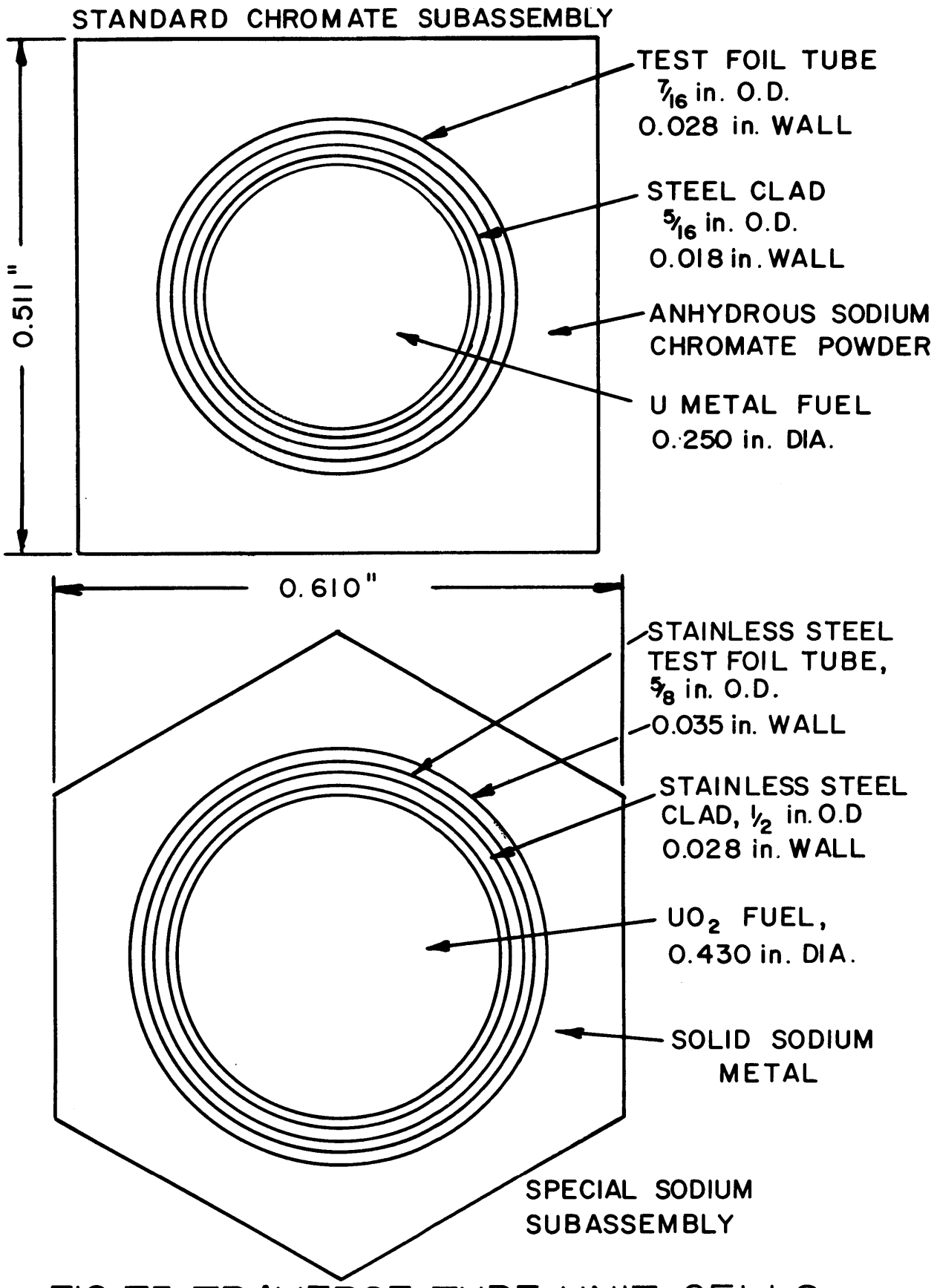

FIG. 7.5 TRAVERSE-TUBE UNIT CELLS

7.3 Summary of Present and Future Work

In-rod U^{238} fission and capture reaction rates are being measured using 18-ppm, U^{235} depleted uranium foils. Work is being done using two-piece annular foils to obtain data on the relative distribution of fission and capture reaction rates in the fuel. Measurements are to be made both with the sodium present in the subassembly and in the sodium-voided condition. These results will be compared to similar measurements made in the uranium metal fuel of the standard subassemblies by Westlake (1) and will help assess just how well the fuel configuration of Blanket Mock-Up No. 2 can be considered to simulate the heterogeneous effects in a real LMFBR blanket.

Work is also being done using six-piece annular foils to determine the actual spatial variation of the fission and capture reaction rates inside the fuel rod. These results will be compared with the theoretical predictions of fast fission enhancement and resonance self-shielding to determine the accuracy of the methods used to account for these effects in LMFBR blanket calculations.

7.4 References

(1) Westlake, W. J., Jr., "Heterogeneity Effects in LMFBR Blanket Fuel Elements," LMFBR Blanket Physics Project Progress Report No. 1, MIT Nuclear Engineering Department (June 1970).

8. CALCULATION OF U^{238} CROSS SECTIONS

V. C. Rogers and I. A. Forbes

8.1 Introduction

An accurate description of the flux and the reaction rates in LMFBR's depends upon the proper treatment of resonance self-shielding in U^{238}. It has been shown (1) that when these effects are neglected, significant discrepancies occur between calculated and experimental activation traverses.

The effects of energy and spatial resonance self-shielding in U^{238} in the Blanket Test Facility are currently being investigated. The MIDI code (2) has been developed and is used to generate broad group cross sections for U^{238} in the resolved and unresolved resonance regions. Flux distributions and reaction rate traverses over the entire assembly are then obtained with the ANISN code using a modified ABBN cross-section set for all other cross sections.

8.2 The Computer Code MIDI

The MIDI code calculates average cross sections in the resonance energy region. It is based upon the IDIOT code (3), a program that generates broad group fission and capture cross sections and their temperature derivatives for use in Doppler calculations. In the resolved region, MIDI calculates the broad group capture, scattering and fission cross sections from basic nuclear and resonance parameters. Broad group cross sections in the unresolved resonance region are calculated from the statistical averages of the resonance parameters. The Doppler-broadened, single-level Breit-Wigner formula is used in all calculations. For the resolved resonances, the narrow resonance and intermediate resonance approximation (4, 5) are available with the λ and κ parameters either included as input or calculated internally. In the unresolved region, the individual resonance parameters are replaced by values obtained by averaging over the appropriate chi-squared or Wigner distributions (6, 7). The unresolved resonance cross sections

are calculated by sequence; a sequence is a set of resonances possessing the same total angular momentum and parity. Several investigators (8-12) have shown that resonance overlap effects between different resonance sequences have a negligible effect upon the broad group cross sections. The effects of resonance overlap within one sequence may be significant, though, and corrections for this effect are performed in MIDI using a series expansion method derived from the multilevel formalism of Hwang (13).

Heterogeneity effects for cylindrical geometry are treated by an extended equivalence relation proposed by Kelber (14). MIDI also has provisions for treating plate cells, typified by the ZPR critical assemblies; this correction is identical to that used in the MC^2 code (15). Preliminary work with the RABID code (16) and with IDIOT indicate that this method for treating heterogeneities is valid above 50 eV. Below this energy, the choice of broad group boundaries becomes a significant factor in averaging over the resonances.

MIDI also has provisions for a fine group collapse to the broad group structure.

Because of the semi-analytic nature of MIDI, most problems can be run in a very short time using very little computer memory. The code is not intended to be as accurate in all instances as MC^2 (15), RABID (16) or RABBLE (17), which require significantly more core memory and have running times over a factor of ten longer. It is intended to be a simple, inexpensive method for calculating resonance self-shielding effects in fast neutron assemblies.

The explicit mathematical formalism employed in MIDI is contained in Reference 2, which also gives input specifications, a program listing, a sample problem and a U^{238} library.

8.3 MIDI-Prepared U^{238} Cross Sections

The MIDI code was used to prepare U^{238} broad group cross sections for the converter plate and Blanket No. 2 in the energy range from 21.5 keV down to 4.65 eV; this corresponds to groups 11 through 21 of the ABBN set. The appropriate converter plate and Blanket No. 2 unit cells (see page 29, Reference 18) were used as input to the calculations.

Table 8.1 compares the U^{238} capture cross sections computed by MIDI with the ABBN infinite-dilution values. Tables 8.2 and 8.3 give the MIDI-derived U^{238} cross sections (in ABBN group format) for Blanket No. 2 and the converter plate, respectively. It is interesting to note that the self-shielded cross sections for the 1/2-inch-diameter UO_2 fuel rods of the converter plate are nearly the same as those for the 1/4-inch-diameter U metal fuel rods of Blanket No. 2.

TABLE 8.1

A Comparison of MIDI-Generated and ABBN Infinite-Dilution U^{238} Capture Cross Sections

Group	Lower Energy	Capture Cross Section (barns)	
		MIDI*	ABBN
10	21.5 keV	--	--
11	10.0 "	0.428	0.750
12	4.65 "	0.626	0.780
13	2.15 "	0.536	1.20
14	1.00 "	0.566	2.10
15	465 eV	0.725	3.60
16	215 "	0.633	4.50
17	100 "	1.058	17.0
18	46.5 "	2.894	15.0
19	21.5 "	2.384	58.0
20	10.0 "	6.621	82.0
21	4.65 "	7.043	171.0

*For Blanket No. 2 unit cell.

TABLE 8.2

U^{238} Cross Sections Generated by MIDI for B.T.F. Blanket No. 2

Group	σ_a	σ_t	$\sigma_{g\to g}$	$\sigma^*_{g\to g+1}$
11	0.428	10.828	10.287	0.113
12	0.626	11.266	10.524	0.116
13	0.536	12.016	11.355	0.125
14	0.566	10.706	10.030	0.110
15	0.725	11.085	10.247	0.113
16	0.633	10.122	9.387	0.103
17	1.058	12.638	11.454	0.126
18	2.894	15.064	12.038	0.132
19	2.384	13.604	11.098	0.122
20	6.621	17.081	10.346	0.114

TABLE 8.3

U^{238} Cross Sections Generated by MIDI for the B.T.F. Converter Plate

Group	σ_a	σ_t	$\sigma_{g\to g}$	$\sigma^*_{g\to g+1}$
11	0.459	11.159	10.583	0.117
12	0.697	11.787	10.969	0.121
13	0.506	11.796	11.167	0.123
14	0.553	10.653	9.990	0.110
15	0.706	11.026	10.207	0.113
16	0.617	10.094	9.374	0.103
17	1.036	12.566	11.404	0.126
18	2.860	15.000	12.007	0.133
19	2.370	13.580	11.088	0.122
20	6.596	17.056	10.346	0.114
21	6.983	16.383	9.297	0.103

$^*\ \sigma_{g\to g+1} = \frac{\xi}{\Delta U}\,\sigma_s$

8.4 Neutron Spectrum and Foil Activation Calculations

The MIDI-derived U^{238} cross sections given in Tables 8.2 and 8.3 have been incorporated in a modified ABBN cross section library. This cross section set has been used with the ANISN code to calculate the multigroup flux and material activation distributions in Blanket No. 2.

In Figure 8.1, the neutron spectrum at a depth of 24.4 cm into Blanket No. 2, calculated with the self-shielded U^{238} cross sections, is compared with that calculated using the original (infinite-dilution) ABBN cross sections. As expected, the low energy end of the neutron spectrum of the MIDI-ANISN calculation decreases much more slowly with decreasing energy than that of the ABBN-ANISN calculation.

With the inclusion of U^{238} resonance self-shielding effects in the computations, significant improvements in the agreement between calculated and experimental foil activation traverses are obtained, as shown in Figure 8.2. The dashed curves were calculated using the infinite-dilution ABBN U^{238} cross sections, while the solid curves were calculated using the self-shielded MIDI U^{238} cross sections. (The normalization of these curves is arbitrary.)

Figure 8.2 shows the capture activation traverses of Au and U^{238}. The agreement between experiment and the MIDI-ANISN calculations indicates that U^{238} self-shielding is a major factor in accurately calculating the flux and the reaction rate traverses.

8.5 Conclusion

Significant improvement in the calculation of the flux and axial foil activation traverses in Blanket No. 2 are obtained when the energy and spatial effects of resonance self-shielding in U^{238} are taken into account with the MIDI code. Residual differences between calculated and experimental values can probably be further reduced by (a) incorporating improved elastic downscatter cross sections, and (b) accounting for the decrease in U^{238} self-shielding close to the blanket-reflector boundary.

Future work will be directed toward relation and comparison of the calculated self-shielded cross sections to the measured intra-rod activation traverses discussed in Chapter 7.

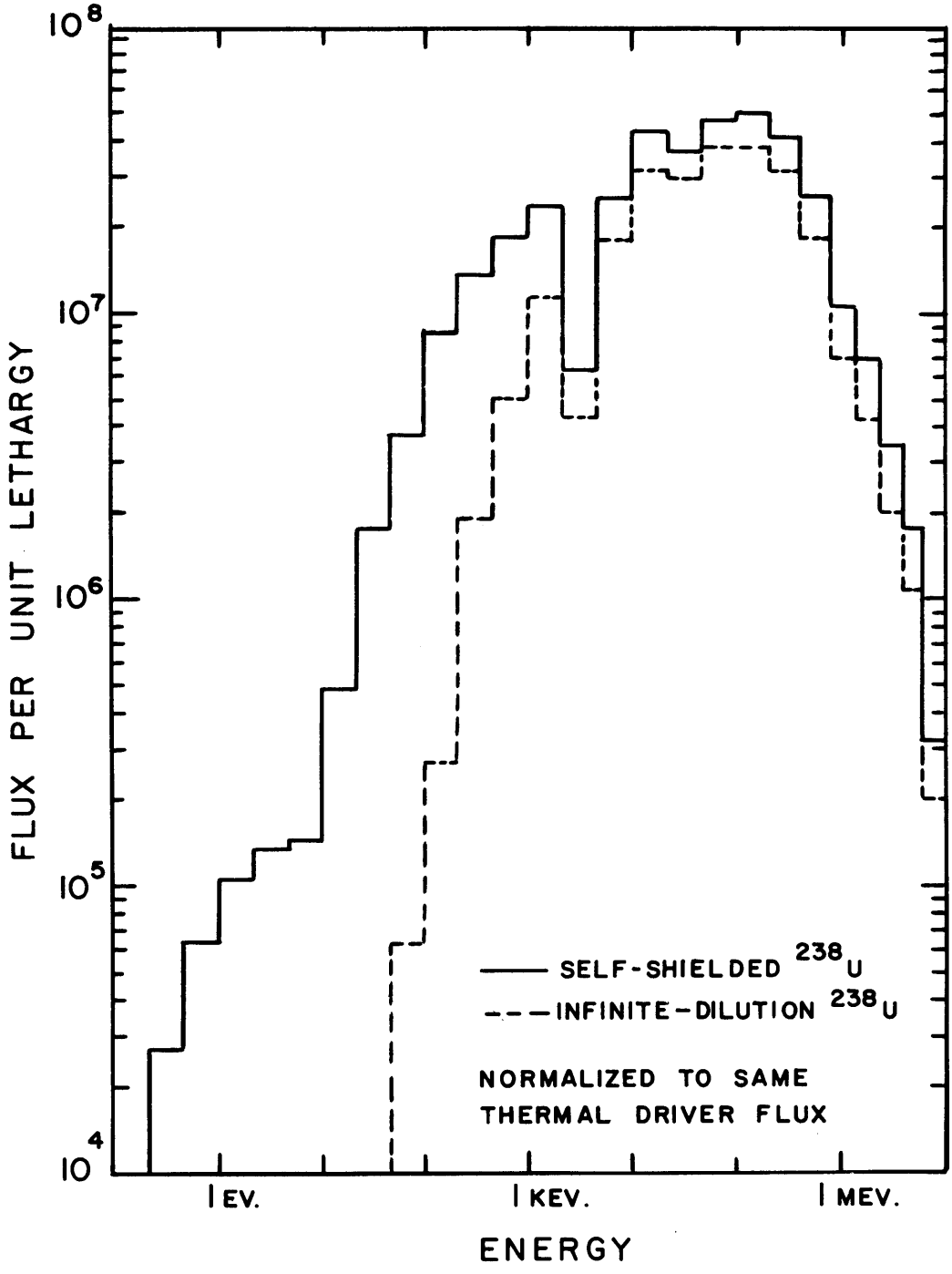

FIG. 8.1 NEUTRON SPECTRUM AT A DEPTH OF 24.4 cm. INTO BLANKET NO. 2

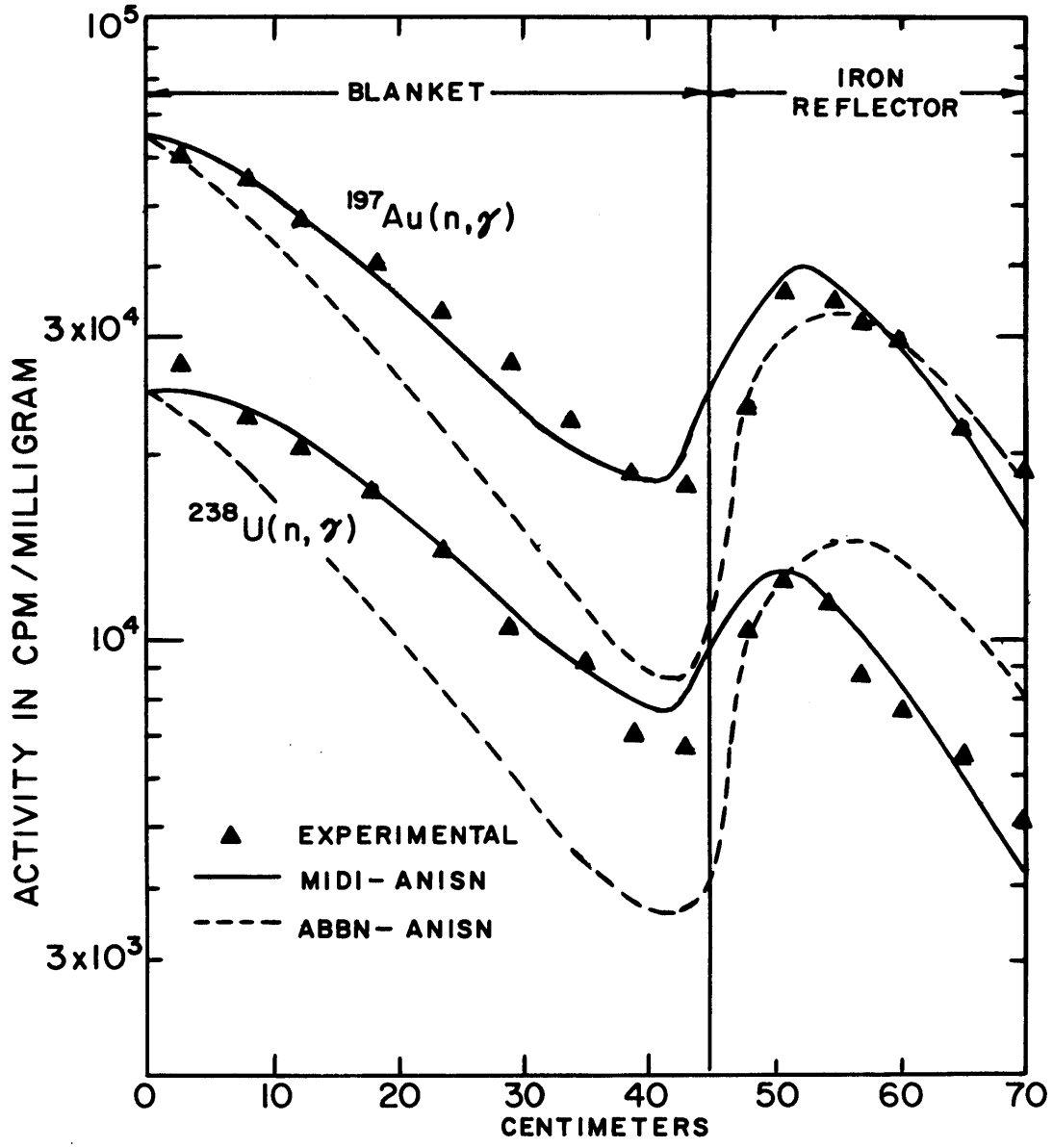

FIG. 8.2 A COMPARISON OF CALCULATED AND EXPERIMENTAL CAPTURE ACTIVATION TRAVERSES IN BLANKET NO. 2

8.6 References

(1) T. C. Leung, M. J. Driscoll, I. Kaplan and D. D. Lanning, "Measurements of Material Activation and Neutron Spectra in an LMFBR Blanket Mock-Up," Trans. Am. Nucl. Soc., 14, 383 (1971).

(2) V. C. Rogers, "MIDI – A Fortran Program for the Calculation of Average Cross Sections in the Resonance Energy Region," Internal Report, Nuclear Engineering Department, M.I.T. (July 1971).

(3) T. A. Pitterle and D. M. Green, "IDIOT – A Fortran-IV Code for Calculation of Resonance-Averaged Effective Cross Sections and Their Temperature Derivatives," APDA-119 (1968).

(4) R. Goldstein and E. R. Cohen, Nucl. Sci. Eng., 13, 132 (1962).

(5) R. Goldstein, Nucl. Sci. Eng., 22, 387 (1965).

(6) J. E. Lynn, The Theory of Neutron Resonance Reactions, Clarendon Press, Oxford (1968).

(7) J. J. Schmidt, "Neutron Cross Sections for Fast Reactor Materials, Part I: Evaluation," KFK-120, EANDC-E-35-0 (1966).

(8) R. B. Nicholson and E. A. Fischer, "The Doppler Effect in Fast Reactors," in Advances in Nuclear Technology, Vol. 4, Academic Press (1968).

(9) E. A. Fischer, Nukleonik, 8, 146 (1966).

(10) B. A. Hutchins, "The Effects of Resonance Overlap on the Doppler Coefficient in a Fast Ceramic Reactor," GEAP-4630 (1964).

(11) R. Froelich and K. Ott, Nucl. Sci. Eng., 22, 487 (1965).

(12) T. F. Heenan and C. R. Adkins, Nucl. Sci. Eng., 45, 279 (1971).

(13) R. N. Hwang, Nucl. Sci. Eng., 21, 253 (1965).

(14) C. N. Kelber, Nucl. Sci. Eng., 42, 257 (1970).

(15) B. J. Toppel, A. L. Rago and D. M. O'Shea, "MC^2, A Code to Calculate Multigroup Cross Sections," ANL-7318 (1967).

(16) A. P. Olson, "RABID: An Integral Transport Theory Code for Neutron Slowing Down in Slab Cells," ANL-7645 (1970).

(17) P. H. Kier and A. A. Robba, "RABBLE, A Program for Computation of Resonance Absorption in Multiregion Reactor Cells," ANL-7326 (1967).

(18) "LMFBR Blanket Physics Project Progress Report No. 1," MIT-4105-3, MITNE-116 (June 1970).

9. OPTIMIZATION OF MATERIAL DISTRIBUTIONS IN FAST BREEDER REACTORS

C. P. Tzanos

This section is a summary of the work presented in the topical report:

> C. P. Tzanos, E. P. Gyftopoulos and M. J. Driscoll, "Optimization of Material Distributions in Fast Breeder Reactors," MIT-4105-6, MITNE-128 (August 1971).

9.1 Introduction

The objective of this study was the development and application of a method to optimize the material distributions in a fast reactor of fixed power output, constrained power density and constrained material volume fractions so as to maximize or minimize a given objective function. (The term, objective function, in this study denotes a criterion of optimality.) An iterative method has been developed, based on linearization of the relations describing the system and on Linear Programming. The method can be used to maximize or minimize integral reactor quantities which are linear functions of the neutron flux and the material volume fractions.

In what follows, primary emphasis has been placed on the problem of optimization of the fuel distribution in the reactor core and a moderator distribution in the reactor blanket so as to obtain a maximum initial breeding gain. In addition, the optimization method has been applied to the problems of optimization of critical mass and sodium void reactivity.

Numerical results show that: (a) the core of maximum initial breeding gain is also the core of minimum critical mass and minimum sodium void reactivity; and (b) the initial breeding gain is a very weak function of the moderator concentration in the blanket.

Without any loss of generality, the development of the method will be discussed in connection with the breeding optimization problem.

9.2 Mathematical Statement of the Problem

A typical fast reactor consists of a core of plutonium-enriched fuel surrounded by a blanket of depleted uranium, which, in turn, is surrounded by a reflector-shield region. It is a common practice to describe the neutron behavior in a fast reactor by the multigroup diffusion equations. For an infinite cylindrical geometry, the diffusion equation for the i^{th} group at a point r is written as (1):

$$\nabla D_i(r)\,\nabla\phi_i(r) - \Sigma_{a,i}(r)\,\phi_i(r) - \sum_{h=i+1}^{N} \Sigma_{(i-h)}(r)\,\phi_i(r) +$$

$$\sum_{h=1}^{i-1} \Sigma_{(h-i)}(r)\,\phi_h(r) + \chi_i \sum_{h=1}^{N} \nu_h \Sigma_{f,h}(r)\,\phi_h(r) = 0\,, \qquad (9.1)$$

where

ϕ_i = neutron flux in group i,

D_i = diffusion coefficient for group i,

$\Sigma_{a,i}$ = macroscopic absorption cross section for group i,

$\Sigma_{(i-h)}$ = macroscopic down-scattering cross section for transfer from group i to group h by elastic and inelastic scattering,

χ_i = fraction of fission neutrons born into group i,

ν_h = number of neutrons released per fission occurring in group h,

$\Sigma_{f,h}$ = macroscopic fission cross section for group h,

N = number of neutron groups.

The power density P(r) at a point r is given by the relation

$$P(r) = \sum_{i=1}^{N} \left\{ u_f(r)\Sigma_{f,i}^{fs} + [N_o - u_f(r) - u_m(r)]\Sigma_{f,i}^{fr} \right\} \phi_i(r), \qquad (9.2)$$

where

$u_f(r)$ = volume fraction of the fissile material,

$u_m(r)$ = volume fraction of the moderating material,

$\Sigma_{f,i}^{fs}$ = macroscopic fission cross section of pure fissile material for group i,

$\Sigma_{f,i}^{fr}$ = macroscopic fission cross section of pure fertile material for group i,

N_o = fissile volume fraction + fertile volume fraction + moderator volume fraction.

The total thermal power W delivered by the reactor is

$$W = 2\pi \int_0^{t_f} \sum_{i=1}^{N} \{ u_f(r) \Sigma_{f,i}^{fs} + [N_o - u_f(r) - u_m(r)] \Sigma_{f,i}^{fr} \} \phi_i(r)\, r\, dr \qquad (9.3)$$

where

t_f = outer reactor radius.

The "economist's breeding gain," here defined as net plutonium production per unit power, can be written as

$$BG = \frac{2\pi \int_0^{t_f} \sum_{i=1}^{N} \{ [N_o - u_f(r) - u_m(r)] \Sigma_{\gamma,i}^{fr} - \Sigma_{a,i}^{fs} u_f(r) \} \phi_i(r)\, r\, dr}{W} \qquad (9.4)$$

where

$\Sigma_{\gamma,i}^{fr}$ = macroscopic capture cross section of pure fertile material for group i,

$\Sigma_{a,i}^{fs}$ = macroscopic absorption cross section of pure fissile material for group i.

In terms of the mathematical relations just cited, the breeding optimization problem is stated as follows: Find the optimum fissile and moderator distributions, $u_f(r)$ and $u_m(r)$, respectively, which maximize the breeding gain BG (Eq. 9.4) while the following equations and inequalities are satisfied:

1. Multigroup diffusion equations (Eq. 9.1).

2. The power density

$$P(r) \leq p = \text{const.} \tag{9.5}$$

3. The total thermal power

$$W = \text{const.} \tag{9.6}$$

4. The sum of fissile and moderator volume fractions

$$u_m + u_f \leq N_o = \text{const.} \tag{9.7}$$

9.3 The Linearized Form of the Breeding Optimization Problem

It is seen from Eqs. 9.1, 9.2, 9.3 and 9.4 that the optimization problem of interest is nonlinear. It is very difficult to solve such a problem explicitly or numerically through use of nonlinear optimization methods. For this reason, computer-aided solutions have been sought through use of appropriate mathematical programming techniques. One of these techniques is Linear Programming which has the advantages of simplicity and availability of standard computer subroutines.

Linear Programming is a method for maximizing (minimizing) a linear objective function for a system with linear algebraic constraints (2). For a nonlinear problem, linearization can be used to reduce the problem into a form suitable for use of Linear Programming.

Linearization of Eqs. 9.1, 9.2, 9.3 and 9.4 by means of a Taylor series expansion results in the following linearized form of these relations.

1. Linearized breeding gain:

$$BG = \frac{2\pi}{W}\left\{-\int_0^{t_f} u_f(r) \sum_{i=1}^{N}\left(\Sigma_{\gamma,i}^{fr}+\Sigma_{a,i}^{fs}\right)\phi_i^o(r)\, r\,dr - \int_0^{t_f} u_m(r) \sum_{i=1}^{N} \Sigma_{\gamma,i}^{fr}\,\phi_i^o(r)\, r\,dr + \right.$$

$$\int_0^{t_f} \sum_{i=1}^{N}\left[\left(N_o - u_f^o(r) - u_m^o(r)\right)\Sigma_{\gamma,i}^{fr} - u_f^o(r)\,\Sigma_{a,i}^{fs}\right]\phi_i^*(r)\, r\,dr +$$

$$\left.\int_0^{t_f} N_o \sum_{i=1}^{N} \Sigma_{\gamma,i}^{fr}\,\phi_i^o(r)\, r\,dr\right\}, \tag{9.8}$$

where the superscript zero is used to denote quantities evaluated at the operating point about which the relations describing the system are linearized, and

$$\phi_i^*(r) = \phi_i(r) - \phi_i^o(r) . \tag{9.9}$$

2. Linearized multigroup diffusion equations:

$$\frac{1}{r}\frac{d}{dr}\left[rD_1^o(r)\frac{d}{dr}\phi_i^*(r)\right] - \Sigma_{a,i}^o(r)\,\phi_i^*(r) - \sum_{h=i+1}^{N}\Sigma_{(i-h)}^o(r)\,\phi_i^*(r) +$$

$$\sum_{h=1}^{i-1}\Sigma_{(h-i)}^o(r)\,\phi_h^*(r) + \chi_i\sum_{h=1}^{N}\nu_h\Sigma_{f,h}^o(r)\,\phi_h^* +$$

$$\left[u_f(r)-u_f^o(r)\right]\left\{-\left[\Sigma_{a,i}^{fs}-\Sigma_{a,i}^{fr}\right]\phi_i^o(r) - \sum_{h=i+1}^{N}\left[\Sigma_{(i-h)}^{fs}-\Sigma_{(i-h)}^{fr}\right]\phi_i^o(r) +\right.$$

$$\sum_{h=1}^{i-1}\left[\Sigma_{(h-i)}^{fs}-\Sigma_{(h-i)}^{fr}\right]\phi_h^o(r) + \chi_i\sum_{h=1}^{N}\left[\nu_h^{fs}\Sigma_{f,h}^{fs}-\nu_h^{fr}\Sigma_{f,h}^{fr}\right]\phi_h^o(r) -$$

$$\left.\frac{\Sigma_{tr,i}^{fs}-\Sigma_{tr,i}^{fr}}{3[\Sigma_{tr,i}^o(r)]^2}\frac{1}{r}\frac{d}{dr}\left[r\frac{d\phi_i^o(r)}{dr}\right]\right\} + \left[u_m(r)-u_m^o(r)\right]$$

$$\left\{-\left[\Sigma_{a,i}^{m}-\Sigma_{a,i}^{fr}\right]\phi_i^o(r) - \sum_{h=i+1}^{N}\left[\Sigma_{(i-h)}^{m}-\Sigma_{(i-h)}^{fr}\right]\phi_i^o(r) +\right.$$

$$\sum_{h=1}^{i-1}\left[\Sigma_{(h-i)}^{m}-\Sigma_{(h-i)}^{fr}\right]\phi_h^o(r) + \chi_i\sum_{h=1}^{N}\left[-\nu_h^{fr}\Sigma_{f,h}^{fr}\right]\phi_h^o(r) -$$

$$\left.\frac{\Sigma_{tr,i}^{m}-\Sigma_{tr,i}^{fr}}{3[\Sigma_{tr,i}^o(r)]^2}\frac{1}{r}\frac{d}{dr}\left[r\frac{d\phi_i^o(r)}{dr}\right]\right\} = 0 , \tag{9.10}$$

where

$\Sigma_{tr,i}$ = macroscopic transport cross section for group i.

The superscript m is used to denote properties of the moderating material.

3. Linearized total thermal power:

$$W = \int_0^{t_f} u_f(r) \sum_{i=1}^{N} \left[\Sigma_{f,i}^{fs} - \Sigma_{f,i}^{fr}\right] \phi_i^o(r)\, r dr -$$

$$\int_0^{t_f} u_m(r) \sum_{i=1}^{N} \Sigma_{f,i}^{fr} \phi_i^o(r)\, r dr + \int_0^{t_f} \sum_{i=1}^{N} \Sigma_{f,i}^{o}(r)\, \phi_i^*(r)\, r dr +$$

$$\int_0^{t_f} \sum_{i=1}^{N} N_o \Sigma_{f,i}^{fr} \phi_i^o(r)\, dr \,. \qquad (9.11)$$

4. Linearized power density:

$$P(r) = u_f(r) \sum_{i=1}^{N} \left[\Sigma_{f,i}^{fs} - \Sigma_{f,i}^{fr}\right] \phi_i^o(r) - u_m(r) \sum_{i=1}^{N} \Sigma_{f,i}^{fr} \phi_i^o(r) +$$

$$\sum_{i=1}^{N} \Sigma_{f,i}^{o} \phi_i^*(r) + \sum_{i=1}^{N} N_o \Sigma_{f,i}^{fr} \phi_i^o(r) \,. \qquad (9.12)$$

When the multigroup diffusion equations are solved to obtain the neutron flux in a reactor, the criticality condition is imposed by the requirement that the eigenvalue of the multigroup diffusion equations be equal to 1. In this study, as explained later, the linearized multigroup diffusion equations are used to express ϕ_i^* as a function of u_f and u_m. For the reactor to remain critical, u_f and u_m cannot change in an arbitrary way. Perturbation theory can be used to express the criticality condition in the form (3):

$$\int_0^{t_f} - [u_f(r) - u_f^o(r)] \sum_{i=1}^{N} \frac{\Sigma_{tr,i}^{fs} - \Sigma_{tr,i}^{fr}}{3[\Sigma_{tr,i}^{o}(r)]^2} \nabla\phi_i^o(r) \nabla\psi_i^o(r) \, rdr +$$

$$\int_0^{t_f} [u_f(r) - u_f^o(r)] \sum_{i=1}^{N} \left[\Sigma_{a,i}^{fs} - \Sigma_{a,i}^{fr}\right] \phi_i^o(r) \psi_i^o(r) \, rdr +$$

$$\int_0^{t_f} [u_f(r) - u_f^o(r)] \sum_{h=1}^{N} \sum_{h=i+1}^{N} \left[\Sigma_{(i-h)}^{fs} - \Sigma_{(i-h)}^{fr}\right] \phi_i^o(r) \left[\psi_i^o(r) - \psi_h^o(r)\right] rdr -$$

$$\frac{1}{k} \int_0^{t_f} [u_f(r) - u_f^o(r)] \sum_{i=1}^{N} \sum_{h=1}^{N} \left[\Sigma_{f,h}^{fs} - \Sigma_{f,h}^{fr}\right] \chi_i \phi_h^o(r) \psi_i^o(r) \, rdr +$$

$$\int_0^{t_f} - [u_m(r) - u_m^o(r)] \sum_{i=1}^{N} \frac{\Sigma_{tr,i}^{m} - \Sigma_{tr,i}^{fr}}{3[\Sigma_{tr,i}^{o}(r)]^2} \nabla\phi_i^o(r) \nabla\psi_i^o(r) \, rdr +$$

$$\int_0^{t_f} [u_m(r) - u_m^o(r)] \sum_{i=1}^{N} \left[\Sigma_{a,i}^{m} - \Sigma_{a,i}^{fr}\right] \phi_i^o(r) \psi_i^o(r) \, rdr +$$

$$\int_0^{t_f} [u_m(r) - u_m^o(r)] \sum_{i=1}^{N} \sum_{h=i+1}^{N} \left[\Sigma_{(i-h)}^{m} - \Sigma_{(i-h)}^{fr}\right] \phi_i^o(r) \left[\psi_i^o(r) - \psi_h^o(r)\right] rdr -$$

$$\frac{1}{k} \int_0^{t_f} [u_m(r) - u_m^o(r)] \sum_{i=1}^{N} \sum_{h=1}^{N} \left[-\nu^{fr} \Sigma_{f,h}^{fr}\right] \chi_i \phi_h^o(r) \psi_i^o(r) \, rdr = 0 , \qquad (9.13)$$

where

ψ_i = adjoint flux for group i,

k = k-effective.

In terms of the linearized relations just cited, the breeding optimization problem is stated as follows: Determine the optimum fissile and moderator distributions $u_f(r)$ and $u_m(r)$, respectively, which maximize the breeding gain BG (Eq. 9.8) while the following relations are satisfied:

1. Linearized multigroup diffusion equations (Eqs. 9.10).

2. The total thermal power

$$W = \text{const.} \qquad (9.14)$$

3. The power density

$$P(r) \leq p = \text{const.} \tag{9.15}$$

4. Criticality condition as expressed by Eq. 9.13.

5. $0 \leq u_f,\ 0 \leq u_m,\ u_m + u_f \leq N_o = \text{const.}$ (9.16)

Even after the linearization, the optimization problem does not yet have the proper form for application of Linear Programming. Such a form, however, can be obtained as follows: (a) the reactor is divided into a number R of regions, each with spatially uniform material concentrations; and (b) the linearized multigroup diffusion equations are solved to express each ϕ_i^* $(i = 1, N)$ as a function of $u_{f,j}$, $u_{m,j}$ $(j=1, R)$. Thus, the functional to be maximized and the constraints of the problem become linear algebraic functions of $u_{f,j}$ and $u_{m,j}$ and therefore suitable for application of Linear Programming.

9.4 Solution of the Linearized Multigroup Diffusion Equations

The linearized multigroup diffusion equations are of the form

$$\underline{L}\,\underline{\phi}^* = \underline{f}(\underline{u}_f^*, u_m^*), \tag{9.17}$$

where $\underline{L}$ is the multigroup diffusion matrix operator and

$$\underline{u}_f^* = u_f - u_f^o, \quad u_m^* = u_m - u_m^o. \tag{9.18}$$

We want to express $\underline{\phi}^*$ as a function of u_f^* and u_m^*. Application of the finite difference technique gives a set of algebraic equations of the form

$$\underline{M}\,\underline{\phi}^* = \underline{f}(\underline{u}_f^*, \underline{u}_m^*). \tag{9.19}$$

Equations 9.19 can be solved by inversion of the matrix $\underline{M}$. On the other hand, even for 5 neutron groups and 100 mesh points, $\underline{M}$ is a large (500×500) matrix and its inversion requires excessive computer time and gives rise to prohibitive round-off errors.

This difficulty can be avoided by use of the method of Piecewise Polynomials, discussed by Kang (4). The method of Piecewise Polynomials can be applied to solve the linearized multigroup diffusion

equations as follows. The reactor is divided into a number n of mesh points and the flux difference ϕ_i^* (Eq. 9.9) is approximated by

$$\phi^* \simeq \phi_i^* = \sum_{k=1}^{n} a_{k,i} w_k + \sum_{k=1}^{n} \beta_{k,i} v_{k,i}, \tag{9.20}$$

where w_k and $v_{k,i}$ are cubic piecewise polynomials (4). The coefficients $a_{k,i}$ and $\beta_{k,i}$ are determined by requiring

$$\int_V (L_i \phi_i^*) w_k \, dV = \int_V f_i(u_f^*, u_m^*) w_k \, dV, \tag{9.21}$$

$$\int_V (L_i \phi_i^*) v_{k,i} \, dV = \int_V f_i(u_f^*, u_m^*) v_{k,i} \, dV, \tag{9.22}$$

where

V = reactor volume.

The integrations on the right-hand side of Eqs. 9.21 and 9.22 cannot be carried out since the space dependence of u_f^* and u_m^* is unknown. On the other hand, if the reactor is divided into a number R of regions with spatially uniform material concentrations in each region, then the right-hand side of Eqs. 9.21 and 9.22 can be integrated and a system of algebraic equations results. These equations are of the form

$$\underline{A}\,\underline{a} = \underline{g}(\underline{u}_f^*, \underline{u}_m^*, a_{11}), \tag{9.23}$$

where a_{11} is the coefficient of the polynomial w_1 in Eq. 9.20 for i = 1, and the components of the vectors $\underline{u}_f^*$, $\underline{u}_m^*$ are given by

$$u_{f,j}^* = u_{f,j} - u_{f,j}^o, \quad u_{m,j}^* = u_{m,j} - u_{m,j}^o, \quad j = 1, R. \tag{9.24}$$

The solution of the system of Eqs. 9.23 is

$$\underline{a} = \underline{A}^{-1} \underline{g}. \tag{9.25}$$

For n mesh intervals and N neutron groups, the order of the matrix $\underline{A}$ is equal to 2nN-1. The method of piecewise polynomials, compared to the finite difference technique, gives a very good approximation to ϕ_i^*

with only a few mesh intervals n. Since the order of matrix $\underline{A}$ is a function of the number of mesh intervals n, the method of piecewise polynomials gives a smaller matrix $\underline{A}$ than the finite difference technique for the same accuracy in ϕ_i^*. Thus, for N = 5 and n = 10, the order of $\underline{A}$ is $2 \times 10 \times 5 - 1 = 99$. For the same accuracy in ϕ_i^*, the finite difference technique gives a 500×500 matrix. The inversion of a 99×99 matrix is much more advantageous than the inversion of a 500×500 matrix from the standpoint of computation time and round-off errors.

9.5 The Iterative Scheme

The solution of the linearized multigroup diffusion equations results in all constraints and the objective function of the problem being linear algebraic relations of $u_{f,j}$ and $u_{m,j}$ $(j = 1, R)$. This means that the original nonlinear optimization problem has been reduced to a Linear Programming optimization problem.

The linearized form of the breeding optimization problem is a good approximation of the original nonlinear problem only if $u_{f,j}$ and $u_{m,j}$ are sufficiently close to $u^o_{f,j}$ and $u^o_{m,j}$, about which linearization took place. Therefore, Linear Programming can be applied to obtain the optimum values of $u_{f,j}$ and $u_{m,j}$ which maximize the objective function, while $u_{f,j}$ and $u_{m,j}$ must satisfy the additional constraints

$$u^o_{f,j} - \varepsilon_f \leq u_{f,j} \leq u^o_{f,j} + \varepsilon_f,\ u^o_{m,j} - \varepsilon_m \leq u_{m,j} \leq u^o_{m,j} + \varepsilon_m,\quad j = 1, R. \tag{9.26}$$

The parameters ε_f, ε_m are constants such that $u_{f,j}$ and $u_{m,j}$ remain close enough to $u^o_{f,j}$ and $u^o_{m,j}$, respectively.

This procedure results in a suboptimum solution, since $u_{f,j}$ and $u_{m,j}$ are restricted by Eqs. 9.26 to only small variations around $u^o_{f,j}$ and $u^o_{m,j}$. To advance the solution, the following iterative scheme is devised. If $u^{(1)}_{f,j}$ and $u^{(1)}_{m,j}$ is the solution given by Linear Programming, the problem is linearized about $u^{(1)}_{f,j}$, $u^{(1)}_{m,j}$ and Linear Programming is again applied, while the relations,

$$u^{(1)}_{f,j} - \varepsilon_f \leq u_{f,j} \leq u^{(1)}_{f,j} + \varepsilon_f,\ u^{(1)}_{m,j} - \varepsilon_m \leq u_{m,j} \leq u^{(1)}_{m,j} + \varepsilon_m,\quad j = 1, R, \tag{9.27}$$

must be satisfied, to obtain another solution $u^{(2)}_{f,j}$, $u^{(2)}_{m,j}$.

This procedure of linearization about the previous solution of Linear Programming and re-application of Linear Programming is repeated until no further improvement of the objective function is achieved. The last Linear Programming solution gives the optimum fissile and moderator distributions which result in the maximum value of the objective function. It must be pointed out that there is no assurance that the determined optimum is a local or a global one. Therefore, one should repeat the iterative procedure, starting with different initial fissile and moderator distributions, and compare the determined optima.

9.6 Remarks

The discussion up to this point has been based on infinite cylindrical geometry. In principle, the optimization method developed can be extended to any reactor geometry. For geometries involving more than one dimension, however, the method becomes very complicated in terms of its numerical implementation.

From among the possible one-dimensional geometries, infinite cylindrical geometry has been selected because: (a) cylindrical geometry is, almost without exception, characteristic of practical reactors; and (b) the optimization of the fuel and/or a moderator distribution is likewise of practical importance primarily in the radial direction. Nevertheless, the method can be applied equally well to any one-dimensional geometry.

In addition, it should be noted that many two-dimensional calculations in cylindrical geometry are approximated by one-dimensional calculations by adding to the macroscopic absorption cross section a DB^2 term to account for axial leakage (5). This approximation can be incorporated in the optimization method by simply adding an appropriate DB^2 term to the macroscopic absorption cross section.

9.7 Applications

The optimization method has been applied to the core of a 1500-MW (th) fast breeder to obtain the fuel distribution that: (a) maximizes the initial breeding gain; (b) minimizes the critical mass; and (c) minimizes the sodium void reactivity.

For these studies, an infinite cylindrical geometry reactor is considered. The core is divided into four regions of equal volume. As explained later, the optimization procedure involves two reactors of different dimensions. They are designated reactor No. 1 and reactor No. 2. The dimensions of reactor No. 1 are given in Table 9.1. The dimensions of reactor No. 2 are given later. The composition of reactors No. 1 and No. 2 is given in Table 9.2. This composition is representative of LMFBR design studies presented over the last several years (6, 7).

The sum of the PuO_2 and UO_2 volume fractions is constrained to remain constant during optimization and equal to 0.35.

For computational convenience, the total thermal power has been normalized to 100 and the power density limit (550 w/cm^3) to a corresponding value 2.30267.

For the neutronic calculations, five neutron groups were employed.

The ANISN multigroup transport theory code was used to obtain a five-group cross-section set by collapsing a sixteen-group, modified Hansen-Roach cross-section set.

The three problems of breeding optimization, critical mass optimization and sodium void reactivity optimization are described by the same equations except for the objective function.

In Table 9.3, the results obtained in the successive iterations of the iterative optimization method applied to the breeding optimization problem are presented. The computation begins with a four-region homogeneous core as given by the first row of Table 9.3. The optimum configuration is given by the last row of the same table. The breeding gain listed in the last column of the table is calculated by the relation

TABLE 9.1

Dimensions of Reactor No. 1

Region		Inner Radius	Outer Radius
Core	1	0.00 cm	62.64 cm
	2	62.64 cm	90.48 cm
	3	90.48 cm	111.36 cm
	4	111.36 cm	128.76 cm
Radial blanket	5	128.76 cm	174.00 cm*

*Extrapolated outer boundary.

TABLE 9.2

Reactor Composition

Material	Core	Blanket	Atomic or Molecular Density (for pure materials) $cm^{-3} \times 10^{-24}$
Na	50 v/o	50 v/o	0.025410
Fe	15 v/o	15 v/o	0.084870
PuO_2	35 v/o	--	0.025189
UO_2		35 v/o	0.024444

TABLE 9.3

Fissile Composition and Breeding Gain as a Function of Linear Programming Iteration Number for Reactor No. 1

Iteration No.	REGION 1	2	3	4	Breeding Gain*
		PuO_2 (v/o)			
1	3.41200	3.41200	3.41200	3.41200	0.576527
2	3.40670	3.53833	3.21200	3.21200	0.578265
3	3.38110	3.69036	3.01200	3.01200	0.579931
4	3.35800	3.82934	2.81200	2.81200	0.581669
5	3.33607	3.95874	2.61200	2.61200	0.583506
6	3.31556	4.07905	2.41200	2.41200	0.585427
7	3.29832	4.17795	2.24362	2.21200	0.587314
8	3.29680	4.16995	2.32654	2.01200	0.588124
9	3.29543	4.16177	2.40826	1.81200	0.588952
10	3.29407	4.15375	2.48842	1.61200	0.589804
11	3.29277	4.14585	2.56699	1.41200	0.590672
12	3.29146	4.13812	2.64417	1.21200	0.591559
13	3.29017	4.13053	2.71992	1.01200	0.592458
14	3.28885	4.12313	2.79443	0.81200	0.593391
15	3.28765	4.11576	2.86731	0.61200	0.594337
16	3.28642	4.10857	2.93906	0.41200	0.595300
17	3.28521	4.10151	3.00954	0.21200	0.596284
18	3.28402	4.09457	3.07881	0.01200	0.597285
19	3.27854	4.09062	3.03854	0.11200	0.600014
20	3.27801	4.08658	3.07689	0.00000	0.600585
21	3.27801	4.08662	3.07676	0.00000	0.600585

*Net production of Pu^{239} atoms per fission.

$$BG = \frac{2\pi \int_0^{t_f} \sum_{i=1}^{N} \left[(N_o - u_f)\, \Sigma_{\gamma,i}^{fr} - \Sigma_{a,i}^{fs} u_f \right] \phi_i \, r\,dr}{2\pi \int_0^{t_f} \sum_{i=1}^{N} \Sigma_{f,i} \phi_i \, r\,dr} . \qquad (9.28)$$

The peaks of the power density in each core region (which occur at the inner radius of each region) for the initial and optimum configurations are shown in Table 9.4.

TABLE 9.4

Peak Power Densities for Reactor No. 1

Region	1	2	3	4
Initial configuration	2.23971	1.68232	1.15895	0.72096
Optimum configuration	2.30265	2.30264	1.14762	0.07654

Since, as already mentioned, there is no assurance that the determined optimum is a local or a global one, the optimization procedure was repeated with a different starting configuration. The same optimum configuration was obtained.

The results of Table 9.3 show that, for the five-region reactor with dimensions as given by Table 9.1 (reactor No. 1), the optimum configuration is one for which there is no PuO_2 in the fourth region, and the peaks of the power density in regions 1 and 2 are equal to the upper power density limit. The breeding gain of the optimum configuration is 4.08% larger than the breeding gain of the initial homogeneous configuration.

The optimization started with a reactor of four core regions and a 45.24-cm blanket. The optimum configuration consists of three core regions and a 62.64-cm blanket (PuO_2 was removed from the fourth core region of the initial configuration). If it were possible to apply

the optimization method to a reactor with a core divided into an arbitrarily large number of regions, the optimum configuration would apparently approach the optimum configuration obtained by an analytical solution of the problem asymptotically as the number of core regions increased. This suggests that a configuration having a further improvement in breeding gain can be obtained by redivision of the core into four regions and reapplication of the optimization procedure. Thus, the core of the optimum reactor No. 1 is redivided into four regions of equal volume. Since a typical fast reactor blanket is about 45 cm thick (6, 7), the extra blanket is also removed. The dimensions of the new reactor, which will be called reactor No. 2 in the remainder of this study, are shown in Table 9.5.

TABLE 9.5
Dimensions of Reactor No. 2

Region		Inner Radius	Outer Radius
Core	1	0.00 cm	55.68 cm
	2	55.68 cm	80.04 cm
	3	80.04 cm	97.44 cm
	4	97.44 cm	111.36 cm
Radial blanket	5	111.36 cm	156.60 cm*

*Extrapolated outer boundary.

The composition and the peak power densities of the optimum configuration of reactor No. 2 are shown in Table 9.6. The breeding gain of the optimum configuration is equal to 0.582528. As shown in Table 9.6, the peak power densities in the first three core regions of the optimum configuration are all equal to the upper power density limit.

The breeding gain of the optimum configuration of reactor No. 2 is slightly smaller than the breeding gain of the optimum configuration of reactor No. 1. This is due to the fact that reactor No. 2 is smaller than

reactor No. 1 and consequently loses more neutrons by leakage. Reduction of the leakage can be achieved by surrounding the blanket by a reflector. The breeding gains of the initial homogeneous version of reactor No. 2, the optimum configuration of reactor No. 1, and the optimum configuration of reactor No. 2, before and after the addition of a 45.24-cm BeO reflector at the outer periphery of the blanket, are shown in Table 9.7. The optimum reactor No. 2 now has a higher total breeding gain than the homogeneous reactor No. 1 and the optimum reactor No. 1, although it has a core about 25% smaller than the homogeneous reactor No. 1.

TABLE 9.6

Optimum Configuration of Reactor No. 2

Region	1	2	3	4
PuO_2 v/o	3.23751	3.72338	5.01528	0.50175
Peak Power Density	2.30267	2.30267	2.30267	0.29742

TABLE 9.7

Effect of Blanket Reflector on Breeding Gain

Reactor	Breeding Gain of Unreflected Reactor			Breeding Gain After Addition of BeO Reflector*		
	Internal	External	Total	Internal	External	Total
Homogeneous No. 1	0.405686	0.170841	0.576527	0.405832	0.202875	0.608707
Optimum No. 1	0.345045	0.255540	0.600585	0.345059	0.270237	0.615296
Optimum No. 2	0.377648	0.204880	0.582528	0.378024	0.239341	0.616365

*45.24-cm BeO reflector.

The same optimization procedure was applied to the problems of critical mass optimization and sodium void reactivity optimization. The results show that the fuel distribution which leads to a maximum breeding gain leads also to a minimum critical mass and a minimum sodium void reactivity. Specifically, the optimum reactor No. 2 has a critical mass 30.54% less and a sodium void reactivity 2.9$ less than the initial homogeneous reactor. In addition, the optimum reactor has a uniform power density (within the practical limits achievable through use of a small number of reactor zones).

The optimization method has also been applied to the problem of optimization of the distribution of a moderator in a fast reactor blanket so as to obtain a maximum initial breeding gain. Numerical results indicate, however, that the initial breeding gain is a very weak function of the moderator concentration in the blanket and, therefore, numerical errors are sufficiently large compared to changes in the optimization variables to obviate blanket optimization by this approach.

To support these results, the change of the breeding gain as a function of the moderator concentration, homogeneously distributed, was investigated.

The dimensions of an infinite cylindrical geometry reactor considered for the computations are shown in Table 9.8. The reactor compositions for BeO and Na moderated blankets are shown in Tables 9.9 and 9.10, respectively. For the neutronic calculations, five neutron groups were used having the same structure and with the same cross sections as for the previous problems.

TABLE 9.8

Dimensions of Reactor Used in Blanket Studies

	Region	Inner Radius	Outer Radius
Core	1	0.00 cm	62.64 cm
	2	62.64 cm	90.48 cm
	3	90.48 cm	111.36 cm
Radial blanket	4	111.36 cm	160.08 cm
Reflector	5	160.08 cm	206.48 cm*

*Extrapolated outer boundary.

TABLE 9.9

Reactor Composition for BeO-Moderated Blanket

Material	Core Regions 1	2	3	Blanket Reflector		Atomic or Molecular Density for Pure Materials
	(v/o)			(v/o)		$cm^{-3} \times 10^{-24}$
PuO_2	3.2775	4.0859	3.0763	--	--	0.025189
UO_2	31.7225	30.9141	31.9237	55	--	0.024444
BeO	--	--	--		--	0.071270
Na	50	50	50	30	--	0.025410
Fe	15	15	15	15	100	0.084870

TABLE 9.10

Reactor Composition for Na-Moderated Blanket

Material	Core Regions 1	2	3	Blanket Reflector		Atomic or Molecular Density for Pure Materials
	(v/o)			(v/o)		$cm^{-3} \times 10^{-24}$
PuO_2	3.2775	4.0859	3.0763	--	--	0.025189
UO_2	31.7225	30.9141	31.9237	85	--	0.024444
Na	50	50	50		--	0.025410
Fe	15	15	15	15	100	0.084870

The results presented in Table 9.11 show that for even marginally significant changes in the breeding gain, large changes in the moderator volume fraction in the blanket are required.

In addition, the results show that: (a) when Na replaces U^{238} in the blanket, the neutron moderation by Na is not enough to offset the loss in breeding due to reduction of the U^{238} concentration, and consequently the breeding gain decreases as the Na concentration increases; (b) when BeO replaces U^{238} in the blanket, for a BeO volume fraction somewhere between 5% and 10%, the improvement in breeding due to moderation by BeO just offsets the loss in breeding due to reduction of the U^{238} concentration; for any other BeO concentration, the neutron moderation is not enough to offset breeding losses due to reduction of the U^{238} concentration.

The results just cited support the conclusion of the optimization studies to the effect that the initial breeding gain depends weakly on the moderator volume fraction in the blanket. This weak dependence could be of considerable importance to reactor economics. It suggests that the addition of an appropriate moderator or diluent in the blanket (and consequently the reduction of U^{238} concentration) might reduce the reprocessing and fabrication costs without significant penalties in breeding gain.

The reprocessing and fabrication costs of the blanket could also be reduced by reduction of the blanket thickness. If the blanket is surrounded by a particularly effective reflector, the blanket thickness might be reduced without significant loss in breeding.

The breeding gains for three different reflectors, BeO, graphite and Fe, and for three different blanket thicknesses — a one-row blanket (16.24 cm), a two-row blanket (32.48 cm) and a three-row blanket (48.72 cm) — are shown in Table 9.12. It is seen from this table that: (a) surrounding the blanket with a reflector improves the breeding gain, compared to an unreflected blanket; the improvement is more significant as the blanket thickness decreases; (b) BeO is better than graphite, and graphite is better than Fe; (c) the breeding gain becomes a stronger function of the reflector properties as the blanket thickness decreases;

TABLE 9.11

The Breeding Gain as a Function of Moderator Concentration in the Blanket

Case	Moderator (v/o)	U^{238} (v/o)	Breeding Gain		
			Internal	External	Total
		Na MODERATOR			
1	10	75	0.340401	0.286165	0.626566
2	20	65	0.341137	0.282633	0.623770
3	30*	55	0.342077	0.277693	0.619770
4	40	45	0.343326	0.270523	0.613849
5	50	35	0.345091	0.259680	0.604771
		BeO MODERATOR			
6	0	55	0.342077	0.277693	0.619770
7	5	50	0.344532	0.275832	0.620364
8	10	45	0.347181	0.272908	0.620089
9	20	35	0.353354	0.263742	0.617096
10	30	25	0.361465	0.248656	0.610121
11	5**	50	0.344557	0.275206	0.619763
12	5***	50	0.343183	0.271740	0.614923

*The volume fractions of Na and UO_2 of this row are representative of typical fast reactor blanket designs.

** $\sigma^{BeO}_{(n, 2n)} = 0.0$

*** $\sigma^{BeO}_{downscattering} = 0.0$

TABLE 9.12

The Breeding Gain as a Function of the Reflector Material and Blanket Thickness

Blanket Thickness (cm)	Breeding Gain		
	Internal	External	Total
BeO Reflector			
16.24	0.344334	0.256966	0.601300
32.48	0.342144	0.276049	0.618193
48.72	0.342076	0.279802	0.621878
Graphite Reflector			
16.24	0.343837	0.240930	0.584767
32.48	0.342133	0.271428	0.613561
48.72	0.342076	0.279611	0.621687
Iron Reflector			
16.24	0.343804	0.213572	0.557376
32.48	0.342196	0.263786	0.605982
48.72	0.342077	0.277693	0.619770
No Reflector			
32.48	0.341873	0.227775	0.569648
48.72	0.342071	0.267543	0.609614

(d) the internal breeding gain is practically insensitive to the nature of the reflector (as long as there is at least one row of blanket assemblies between core and reflector); and (e) for a 46.4-cm BeO reflector, the breeding gain of a three-row blanket is larger than that of a one-row blanket by only 3.31%. The results of Table 9.12 suggest that from the standpoint of economics a one- or two-row blanket surrounded by a BeO reflector could be better than a three-row blanket. Reduction of the blanket thickness might reduce the reprocessing and fabrication costs without significant penalties in breeding gain.

On the basis of breeding alone, there are two benefits to be obtained from the addition of reflectors: (a) neutron leakage is reduced from the blanket; and (b) neutron moderation softens the spectrum and favors captures by the fertile material in the sub-keV energy range. In this regard, BeO is better than graphite and Fe. In addition, BeO has the property of producing neutrons through a (n, 2n) reaction for incident neutron energies higher than 1.8 MeV. To evaluate the relative significance of the reflective and moderating properties and of the (n, 2n) reaction with respect to the breeding gain, the breeding gain has been computed for a two-row blanket and: (a) a fictitious, "infinite-mass" BeO reflector with downscattering cross sections set equal to zero; (b) a fictitious BeO reflector with the cross section for the (n, 2n) reaction set equal to zero. The results are shown in Table 9.13. It is seen from this table that: (a) the reduction of neutron leakage is much more significant than moderation; and (b) the effect of the (n, 2n) reaction is negligible. These results suggest that a simple figure of merit of a fast reactor blanket reflector could be determined as a function of only the transport and absorption cross sections of the reflector. A mean albedo (calculated using properly weighted cross sections) could be such a figure of merit. If this is so, then all materials could be ranked according to this figure of merit and the best fast reactor blanket reflector material readily selected.

It must be pointed out that all computations up to this point have been done without taking into account any resonance self-shielding corrections. The breeding gains of a two-row blanket, surrounded by a BeO reflector with shielded and unshielded cross sections for U^{238},

are shown in Table 9.14. It is seen from this table that the shielded cross sections give a slightly smaller breeding gain. It is worth noting that the effect of self-shielding would be more significant if appreciable amounts of a strong absorber such as plutonium were present in the blanket, as will occur near the end of the blanket fuel subassembly irradiation life.

TABLE 9.13

The Breeding Gain as a Function of BeO Reflector Properties

Reflector	Breeding Gain		
	Internal	External	Total
No reflector	0.341873	0.227775	0.569648
BeO with $\sigma_{downscattering} = 0.0$	0.342354	0.273840	0.616194
BeO with $\sigma_{n, 2n} = 0.0$	0.342146	0.275884	0.618030
BeO	0.342144	0.276049	0.618193

TABLE 9.14

The Effect of Resonance Self-Shielding on Breeding Gain

U^{238} Cross Sections	Breeding Gain		
	Internal	External	Total
Unshielded	0.342144	0.276049	0.618193
Shielded	0.346069	0.265469	0.611538

9.8 Conclusions

An iterative optimization method based on linearization and on Linear Programming is developed. The method can be used for the determination of the material distributions in a fast reactor of fixed power output, constrained power density and constrained material

volume fractions that maximize or minimize integral reactor parameters which are linear functions of the neutron flux and the material volume fractions.

The method has been applied: (1) To the problems of optimization of fuel distribution in the reactor core so as to obtain (a) maximum initial breeding gain, (b) a minimum critical mass, and (c) a minimum sodium void reactivity. Numerical results show that the same fuel distribution yields maximum breeding gain, minimum critical mass, minimum sodium void reactivity and uniform power density. (2) To the problem of optimization of a moderator distribution in the blanket so as to maximize the initial breeding gain. The results indicate that the breeding gain is a weak function of the moderator distribution. These results are confirmed by studying the effects on the breeding gain of the insertion of a moderator, homogeneously distributed, in the blanket.

Finally, the effects on the breeding gain of surrounding the blanket by a reflector are investigated. The results show that: (a) savings in blanket thickness may be achieved with choice of a proper reflector without substantial loss in breeding and (b) the transport and absorption properties of a medium, rather than its moderating properties, determine the figure of merit of a fast reactor blanket reflector.

9.9 References

(1) Lamarsh, J. R., "Introduction to Nuclear Reactor Theory," Addison-Wesley, Reading, Massachusetts (1966).

(2) Hadley, G., "Linear Programming," Addison-Wesley, Reading, Massachusetts (1962).

(3) Rohan, P. E., "Comparisons of Transport and Diffusion Theory Calculations of Performance Characteristics for Large Fast Reactors," University of Illinois, Urbana, Illinois (1970).

(4) Kang, C. M. and K. F. Hansen, "Finite Element Methods for Space-Time Reactor Analysis," MIT-3903-5, MITNE-135. Expected publication date, November 1971.

(5) Loewenstein, W. B. and G. W. Main, "Fast Reactor Shape Factors and Shape-Dependent Variables," ANL-6403 (Nov. 1961).

(6) "Proceedings of the Conference on Safety, Fuels and Core Design in Large, Fast Power Reactors," ANL-7120 (Oct. 1965).

(7) "Proceedings of the International Conference on Sodium Technology and Large Fast Reactor Design," ANL-7520 (Nov. 1968).

10. ECONOMIC EVALUATION OF LMFBR BLANKET PERFORMANCE

S. T. Brewer

It is clear that the determining factor in the selection of blanket design features will not be neutronics alone, but only as properly interpreted in the light of economic considerations. Development of a consistent economic-neutronic assessment procedure has been the subject of the work to be reported in detail in the forthcoming topical report:

> S. T. Brewer, E. A. Mason and M. J. Driscoll, "Economics of Fuel Depletion in Fast Breeder Reactor Blankets," COO-3060-4, MITNE-123.

A detailed summary of the results of this work and of supplementary work in this area will be contained in next year's annual report.

11. SUMMARY, CONCLUSIONS AND FUTURE WORK

M. J. Driscoll

11.1 Introduction

This is the second annual report of the LMFBR Blanket Physics Project at M.I.T. During the past year, work has been primarily concerned with the following four areas:

(a) Measurements on Blanket Mock-Up No. 2, a benchmark version of typical 1000-MWe plant LMFBR blanket/reflector designs (see Chapters 2 and 3).

(b) Evaluation of a variety of alternative methods for acquisition of reactor physics data from the experiments on Blanket Mock-Up No. 2 (Chapters 4, 5, 6).

(c) Investigation of the effects of U^{238} self-shielding, which are the major source of differences between an idealized homogeneous system and the as-built heterogeneous system (Chapters 7 and 8).

(d) Analyses of blanket physics and economics leading to selection of a design for Blanket Mock-Up No. 3 (Chapters 9 and 10).

11.2 Discussion

The most important conclusions which may be drawn from the results of the work on Blanket Mock-Up No. 2 are as follows:

(1) In general, there was good agreement between experimental results and the results of multigroup calculations, which gives some assurance that current blanket design calculations are not badly amiss.

(2) Fast neutron propagation in the reflector (here iron) is the area in which the largest discrepancies between theory and experiment were encountered. This could have important consequences in shield design.

(3) U^{238} self-shielding effects are important in the blanket. State-of-the-art heterogeneity correction methods appear to do an adequate job in correcting for these effects, however.

(4) Absorption and scattering resonance mismatch effects near the boundary between the widely dissimilar blanket and reflector deserve more analysis.

The work on assessment of experimental methods has led to the following conclusions:

(1) Conventional foil activation techniques remain the single most useful tool, and they will receive increased emphasis in future work.

(2) Simple few-foil methods for inference of neutron spectra can be developed by application of slowing-down theory to facilitate the unfolding process. Further development and application of this technique is planned.

(3) Prompt gamma methods possess some intriguing features, but almost all of their capabilities can be matched or exceeded by other techniques and therefore less emphasis in this area is projected.

(4) Evaluation of instrumental neutron spectrometers is still under way. At least one will be adopted as a standard alternative to the foil method. It is clear, however, that since none of the spectrometers is useful below several keV, their exclusive use is impractical in the present applications.

(5) In-pile measurements have, in general, proved more practical than beam-extraction experiments, and hence less emphasis on the latter approach is in order.

Economic and optimization studies are continuing, but some trends are clear from the work completed so far:

(1) The use of better reflectors than the steel ones now envisioned appears to offer one avenue for improvement of radial blanket

economics. Less blanket subassemblies can be used, and without excessive loss of breeding gain if high-albedo materials, such as BeO, are substituted for steel.

(2) More thermal/hydraulic design data must be factored into radial blanket analysis. Apparently, the physics design is fairly forgiving insofar as maintenance of a high breeding ratio is concerned, and therefore engineering design considerations may well determine the preferable blanket configuration.

(3) Emphasis must evolve from beginning-of-life optimization to time-dependent optimization in which the power shift with exposure is considered.

(4) Few- or even one-group methods can be profitably used for economics studies.

11.3 Future Work

During the coming contract year, July 1, 1971, through June 30, 1972, work will be concerned mainly with the following:

(1) Completion of the documentation of work performed on Blanket Mock-Up No. 2.

(2) Foil activation measurements on Blanket Mock-Up No. 3: essentially a repetition of the measurements made on Blanket Mock-Up No. 2.

(3) Other experimental and analytical work, primarily on U^{238} heterogeneity effects and unfolding of foil data to obtain neutron spectra.

(4) Numerical investigations of blanket design and economic performance.

The major focal point for next year's work will be Blanket Mock-Up No. 3, which will have a graphite reflector and which will therefore provide data to help answer the question as to whether high-albedo

reflectors can permit use of thinner, and therefore more economic, radial blankets. Mock-Up No. 3 will be identical to No. 2, except that a 12-inch-thick graphite reflector (i.e., equivalent to two subassembly rows) is inserted in place of the third blanket subassembly row of No. 2.

The choice of graphite for the improved reflector study was based upon a number of considerations:

(1) Calculations showed that graphite and BeO were roughly equivalent candidates insofar as the potential magnitude of the improvement in the blanket U^{238} capture rate; and both were substantially superior to other materials investigated, such as nickel (which has been shown to be a good core reflector in studies done for EBR-II and FFTF), as can be seen in Figure 11.1, and in Figure 10.2 of last year's annual report.

(2) Graphite cannot be ruled out as a material suitable for actual use in a practical application. An early version of the British PFR design incorporated a graphite reflector (1), as does the Westinghouse modular core design concept (2). Although BeO may prove more compatible with sodium coolant, there already exists some, and perhaps adequate, experimental data pertinent to its use as a blanket reflector, acquired at ANL as part of studies on coupled fast-thermal reactors (3). Successful use of BeO in SEFOR, and its consideration as a blanket reflector in an early version of a GE 1000-MWe plant design (4), indicate that it must be considered further, should the final conclusions of this project substantiate the presumed advantages of high performance blanket reflectors.

(3) Although an even better moderator, zirconium hydride, has been shown to be adequately compatible with sodium at 1000° F by German investigators (5), calculations have shown that the albedo of a reflector is substantially more important for the present purposes than its moderating power. Thus, while this and other candidate materials will be examined further in numerical studies, graphite appeared to have a higher justifiable priority for experimental investigation at this time.

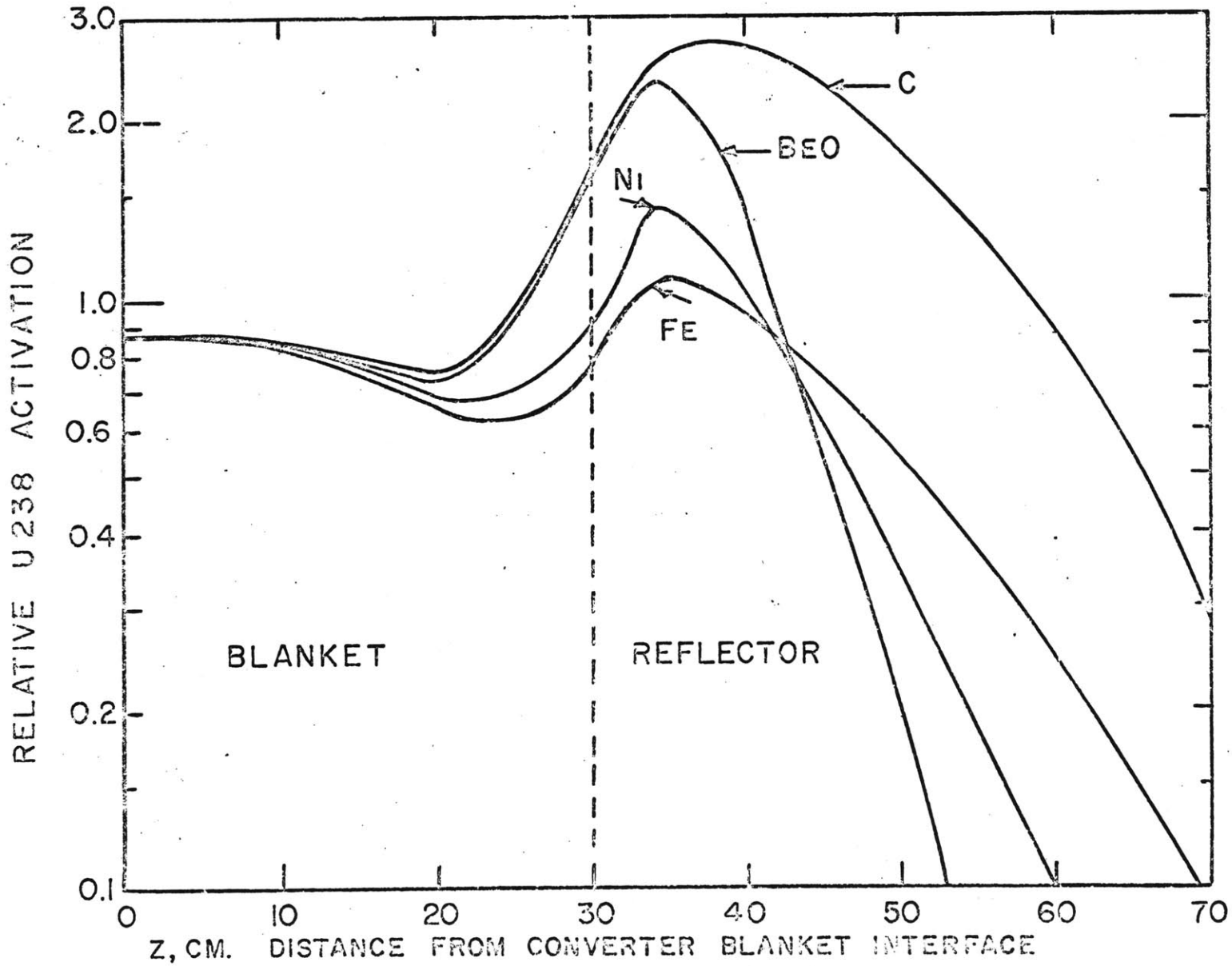

FIG 11.1 UNSHIELDED U238 ACTIVATION IN BLANKET NO. 3 FOR VARIOUS REFLECTOR MATERIAL

(4) Finally, and not inconsequentially, sufficient reactor-grade graphite was already available at MIT at no cost to the project, while several tons of BeO would have to be purchased at on the order of $50 per pound, and its use would involve handling problems because of its extreme toxicity.

Paralleling the experimental work done to confirm the reactor physics advantages of improved reflection, we will have to carry out more detailed burnup, fuel management and economic trade-off analyses to determine whether, when all important variables are taken into account, attractive cost savings do indeed accrue from improved radial blanket designs. Some of this has already been done in developing the motivation for pursuing this avenue for improved blanket design; but more detailed studies remain to be done to define the magnitude of savings resulting from items such as better blanket subassembly power-flattening, reduction in mixed-mean outlet-temperature degradation, simplification of fuel handling procedures, and the like. Also, while radial blanket neutronics have been emphasized in the work to date, the applicability of this work to axial blanket design must also be evaluated.

11.4 References

(1) D.C.G. Smith, J.E. Mann and R.C. Wheeler, "Some Physics Studies in Support of PFR Design," in "Fast Breeder Reactors," Proceedings of 1966 BNES London Conference, P.V. Evans, ed., Pergamon Press, New York (1967).

(2) R.B. Steck, ed., "Liquid Metal Fast Breeder Reactor Design Study, Final Report," WCAP-3251-1 (January 1964).

(3) R. Avery et al., "Coupled Fast-Thermal Power Breeder Critical Experiment," Vol. 12, Second ICPUAE Geneva (1958).

(4) K.P. Cohen and G.L. O'Neill, "Safety and Economic Characteristics of a 1000 MWe Fast Sodium-Cooled Reactor Design," Advan. Nucl. Sci. Technol., 4 (1968).

(5) R. Harde and K.W. Stöhr, "A Sodium-Cooled Power Reactor Experiment Employing Zirconium-Hydride Moderator," Vol. 6, Third ICPUAE, Geneva (1965).

Appendix A

BIBLIOGRAPHY OF BLANKET PHYSICS PROJECT PUBLICATIONS

In this appendix are tabulated all publications associated with work performed in the MIT Blanket Physics Project. Sc.D. theses are listed first, followed by S.M. theses and then by other publications.

A.1 DOCTORAL THESES

(Also see section 3 for corresponding topical reports.)

A.1.1 Completed

Forbes, I.A.

Design, Construction and Evaluation of a Facility for the Simulation of Fast Reactor Blankets

Ph.D. Thesis, MIT Nucl. Eng. Dept., Feb. 1970

(Thesis Supervisor: M.J. Driscoll)

Sheaffer, M.K.

A One-Group Method for Fast Reactor Calculations

Ph.D. Thesis, MIT Nucl. Eng. Dept., August 1970

(Thesis Supervisors: M.J. Driscoll and I. Kaplan)

A.1.2 Forthcoming (titles are tentative)

Brewer, S.T.

Economics of Fuel Depletion in Fast Breeder Reactor Blankets

Leung, T.C.

Neutronics of an LMFBR Blanket Mock-Up

Tzanos, C.P.

Optimization of Material Distributions in Fast Breeder Reactors

Ortiz, N.R.

Instrumental Methods for Neutron Spectroscopy in the MIT Blanket Test Facility

A.1.2 Forthcoming (continued)

Kang, C.S.

Use of Gamma Spectroscopy for Neutronic Analysis of LMFBR Blankets

A.2 S.M. THESES

Forsberg, C.W.

Determination of Neutron Spectra by Prompt Gamma-Ray Spectrometry

M.S. Thesis, MIT Nucl. Eng. Dept., June 1971

(Thesis Supervisors: M.J. Driscoll and N.C. Rasmussen)

Ho, S.L.

Measurement of Fast and Epithermal Neutron Spectra Using Foil Activation Techniques

S.M. Thesis, MIT Nucl. Eng. Dept., Jan. 1970

(Thesis Supervisor: M.J. Driscoll)

Pant, A.

Feasibility Study of a Converter Assembly for Fusion Blanket Experiments

S.M. Thesis, MIT Nucl. Eng. Dept., Jan. 1971

(Thesis Supervisors: M.J. Driscoll and L.M. Lidsky)

Passman, N.A.

An Improved Foil Activation Method for Determination of Fast Neutron Spectra

S.M. Thesis, MIT Nucl. Eng. Dept., Jan. 1971

(Thesis Supervisor: M.J. Driscoll)

Shupe, D.A.

The Feasibility of Inferring the Incident Neutron Spectrum from Prompt Capture Gamma-Ray Spectra

S.M. Thesis, MIT Physics Dept.

(Thesis Supervisor: M.J. Driscoll)

Westlake, W.J.

Heterogeneous Effects in LMFBR Blanket Fuel Elements

S.M. Thesis, MIT Nucl. Eng. Dept., June 1970

(Thesis Supervisor: M.J. Driscoll)

A.3 OTHER PUBLICATIONS

A.3.1 Prior to June 30, 1971

I.A. Forbes, M.J. Driscoll, T.J. Thompson, I. Kaplan and D.D. Lanning

Design, Construction and Evaluation of a Facility for the Simulation of Fast Reactor Blankets

MIT-4105-2, MITNE-110, Feb. 1970

M.K. Sheaffer, M.J. Driscoll and I. Kaplan

A One-Group Method for Fast Reactor Calculations

MIT-4105-1, MITNE-108, Sept. 1970

I.A. Forbes, M.J. Driscoll, D. D. Lanning, I. Kaplan and N.C. Rasmussen

LMFBR Blanket Physics Project Progress Report No. 1

MIT-4105-3, MITNE-116, June 30, 1970

I.A. Forbes, M.J. Driscoll, T.J. Thompson, I. Kaplan and D.D. Lanning

Design, Construction and Evaluation of an LMFBR Blanket Test Facility

Trans. Am. Nucl. Soc., Vol. 13, No. 1, June 1970

M.K. Sheaffer, M.J. Driscoll and I. Kaplan

A Simple One-Group Method for Fast Reactor Calculations

Trans. Am. Nucl. Soc., Vol. 14, No. 1, June 1971

S.T. Brewer, M.J. Driscoll and E.A. Mason

FBR Blanket Depletion Studies – Effect of Number of Energy Groups

Trans. Am. Nucl. Soc., Vol. 13, No. 2, Nov. 1970

T.C. Leung, M.J. Driscoll, I. Kaplan and D.D. Lanning

Measurements of Material Activation and Neutron Spectra In an LMFBR Blanket Mock-Up

Trans. Am. Nucl. Soc., Vol. 14, No. 1, June 1971

S.T. Brewer, E.A. Mason and M.J. Driscoll

On the Economic Potential of FBR Blankets

Trans. Am. Nucl. Soc., Vol. 14, No. 1, June 1971

A.3.2 Forthcoming (titles are tentative)

S.T. Brewer, E.A. Mason and M.J. Driscoll

Economics of Fuel Depletion in Fast Breeder Reactor Blankets

COO-3060-4, MITNE-123

T.C. Leung, M.J. Driscoll, I. Kaplan and D.D. Lanning

Neutronics of an LMFBR Blanket Mock-Up

COO-3060-1, MITNE-127

C.P. Tzanos, E.P. Gyftopoulos and M.J. Driscoll

Optimization of Material Distributions in Fast Breeder Reactors

MIT-4105-6, MITNE-128

N.R. Ortiz, I.C. Rickard, M.J. Driscoll and N.C. Rasmussen

Instrumental Methods for Neutron Spectroscopy in the MIT Blanket Test Facility

COO-3060-3, MITNE-129

C.S. Kang, N.C. Rasmussen and M.J. Driscoll

Use of Gamma Spectroscopy for Neutronic Analysis of LMFBR Blankets

COO-3060-2, MITNE-130

I.A. Forbes, M.J. Driscoll, N.C. Rasmussen, D.D. Lanning and I. Kaplan

LMFBR Blanket Physics Project Progress Report No. 2

COO-3060-5, MITNE-131

T.C. Leung and M.J. Driscoll

A Simple Foil Method for LMFBR Spectrum Determination

Trans. Am. Nucl. Soc., Vol. 14, No. 2, Oct. 1971